Winter 12-22-2021

Direct Single Molecule Imaging of Enhanced Diffusion for Enzymes and Enzyme-conjugated Dna origami

Mengqi Xu
Syracuse University

Abstract

Enzymes have been shown to diffuse faster in the presence of their substrates. Recently, we revealed new insights into this process of enhanced diffusion using single-particle tracking (SPT) with total internal reflection fluorescence (TIRF) microscopy. We found that the mobility of individual enzymes was enhanced three-fold in the presence of the substrate, and the motion remained Brownian. We showed that the relative increase in diffusion is independent of the total enzyme concentrations; and the oligomerization state of enzymes did not change during the catalytic turnover. These experiments ruled out the possibility that the enhanced enzyme diffusion was caused by the collective effects or the size changing of enzymes during reaction. We also compared different experimental designs with different data analysis approaches for studying single enzyme diffusion. We tried different surface coating methods (polymer brush coated surface and lipid bilayer coated surface) and different viscosity agents (methylcellulose and glycerol) to slow diffusion and facilitate tracking. We found that high amounts of glycerol inhibited enzyme activity, resulting in the failure to observe the enhanced diffusion. To get rid of glycerol, we tethered enzymes directly on the supported lipid bilayers (SLBs) and found a similar enhanced diffusion behavior for the tethered enzymes. Using active enzymes as motors, we also tried to construct highly programmable self-propelled enzyme-powered DNA origami active particles and study the mechanism of propulsion from the bottom-up.

Direct Single Molecule Imaging of Enhanced Diffusion for Enzymes and Enzyme-conjugated DNA Origami

By

Mengqi Xu

B.S., South University of Science and Technology of China, 2016

M.S., University of Massachusetts Amherst, 2019

DISSERTATION

SUBMITTED IN PARTIAL FULFILLMENT OF THE REQUIREMENTS FOR

THE DEGREE OF

DOCTOR OF PHILOSOPHY IN PHYSICS

Syracuse University

December 2021

Acknowledgements

First and foremost I would like to express my sincere gratitude to my supervisor, Prof. Jennifer L. Ross. She has been an incredible advisor for me during the past five year both on my research and my life. Her immense passion and rigor for science inspired me throughout and shaped my future interests as well. I feel very lucky to be her student and I deeply appreciate for all of her invaluable advice and unwavering support throughout the my PhD studies.

I would also like to extend my sincere thanks to Prof. Ayusman Sen, Prof. W. Benjamin Rogers and Prof. Wylie Ahmed for their insightful comments and suggestions, professional assistance and support for me at every stage of my research project. Their immense knowledge and plentiful experience have inspired and encouraged me all the time of my academic research and daily life. I feel very privileged to able to collaborate with their group and work with them during my PhD studies.

Next, I would like to thank my committee members, Prof. Carlos Castaneda, Prof. Alison E Patteson, Prof. Liviu Movileanu, Prof. Christian D Santangelo and Prof. Jennifer Schwarz for their inspirational suggestions and professional comments about my thesis and dissertation.

I would also like to offer my special thanks to my collaborators and mentors, Dr. Lyanne Valdez, Dr. Xi Zhao, Daichi Hayakawa, Dr. Thomas Videbaek and Ryan Muoio all of for their technical help and support on my research project. They taught me to perform the basic enzyme and DNA experiments and were always supporting me to collect data for my research project. I have learnt a great deal from their expertise. And especially, I would like to thanks Daichi for his brilliant mentorship for me on DNA origami. I really appreciate for all of his teaching, supporting, help and exceptional patience for me throughout the project. I am indebted

to him for always being willing to answer any kinds of my questions and kindly sharing so much knowledge about DNA origami since the collaboration. The work he has done and the conversations with him were really influential in shaping my experiment methods and critiquing my results as shown in Chapter 5.

Also, I would like to express my thanks to all of my labmates, especially to Sumon Sahu, Dr. Leila Farhadi, and K. Alice Lindsay, for all of their kind help and support and cherished time spent together in the lab. My appreciation also goes out to my friends and my roommates both at UMass and Syracuse. It's been really hard to transfer to a new school at the beginning of my forth year, and also extremely difficult to try building up a new lab at a new place from zero. But thanks to all of you for always being my side, encouraging me, supporting me, believing in me and giving me strength to carry on.

Finally, I would like to express my deep gratefulness to my mom and dad, my warm harbor. Thank you for all of your tremendous understanding, unconditional encouragement, unwavering support and love. I would never be able to go through all of these difficulties myself alone. Everything I have and everything I am, I owe it all to you. Thank you, my two lifelines.

Contents

List of Figures

To my beloved mom and dad...

Chapter 1

Introduction

Active matter, comprised of large numbers of energy-using components, can exhibit remarkable properties as found in living materials, that traditional, passive materials cannot have. Enzymes are such an energy-consuming unit that use energy to perform a variety of tasks required for the basic functions of cells, and thus can be seen as nanoscale active matter. For catalytic enzymes, they bind with their substrates specifically at the active site and convert them into product molecules with high efficiency. For motor protein enzymes, they can harness the chemical free energy released during the substrate turnover and convert it into kinetic energy to achieve mechanical motion [1–3].

1.1 Enhanced enzyme diffusion

Recently, exciting work about enzymes shows that the capability of chemical/kinetic energy conversion is not restricted to motor protein enzymes. Some catalytic enzymes, such as urease [6], catalase [7], DNA polymerase [8], and hexokinase [9] can also perform mechanical energy conversion. Specifically, when performing chemical reactions, these nanoscale active constituents can propel themselves in a way

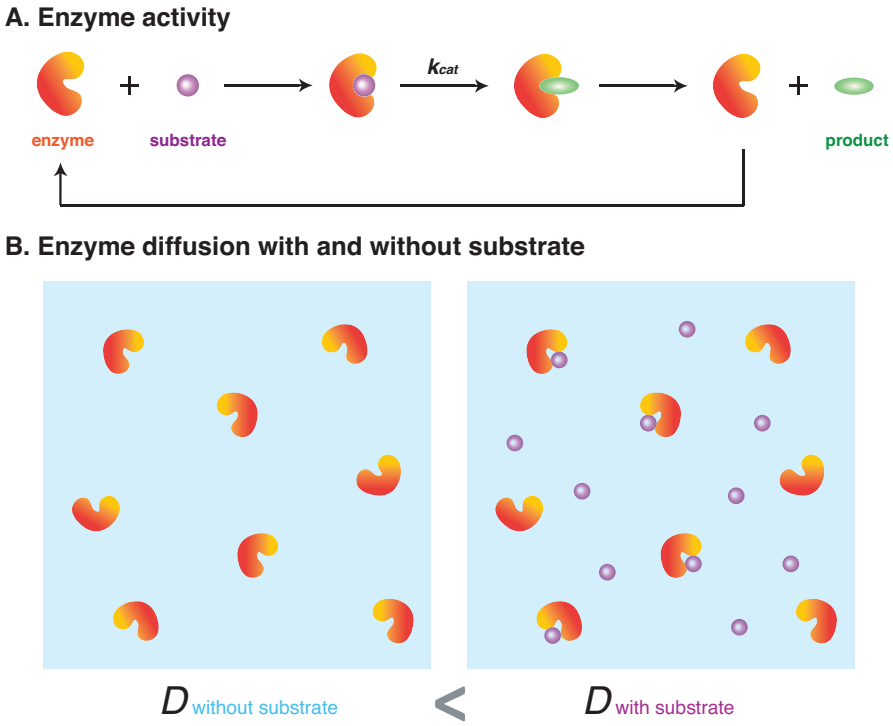

FIGURE 1.1: Schematic of A) Enzyme activity: Enzymes, as nanoscale protein molecules, can catalyze chemical reactions. It can specifically bind with the substrate molecules, convent it into product molecules and release it, in the meanwhile, having energy exchange with the environment. As a catalyst, enzyme might change the shape during the chemical reaction, but will return to the original conformation after the catalytic turnover, and waiting for another substrate to come and bind.

B) Enhanced enzyme diffusion with the presence of substrate.

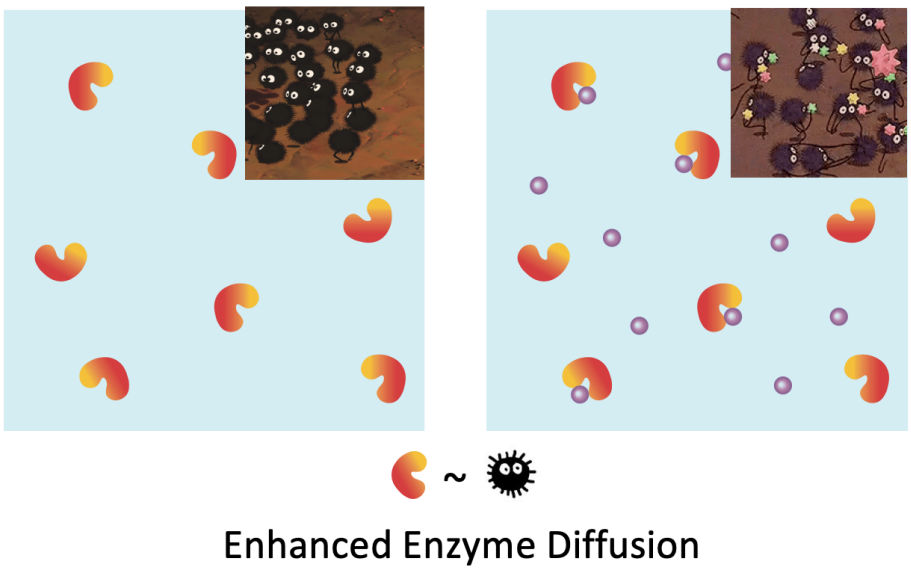

FIGURE 1.2: Active enzymes behave as little fairy dust in Hayao Miyazaki's movie, *Spirited Away*.

and display an enhanced diffusion (Fig. 1.1) [6, 7, 9–15]. That is to say, these active enzymes are just like those little fairy dust in Hayao Miyazaki's movie, *Spirited Away*, when getting food (substrate), the little fairy dust (enzyme) would become happier, more energetic and start to running around (diffuse faster), as demonstrated in Fig. 1.2.

Using active enzymes as propulsive units and coupling them onto the surface of plastic spheres [4] or silica tubes [5], people also constructed self-propelled nanorockets as shown in Fig. 1.3. These emergent findings about enzymes have ignited a series of research on the possible mechanisms and uses for enzymes in active materials. While the fundamental physics about how single enzymes could "self-propel" or achieve enhanced diffusion still remains open.

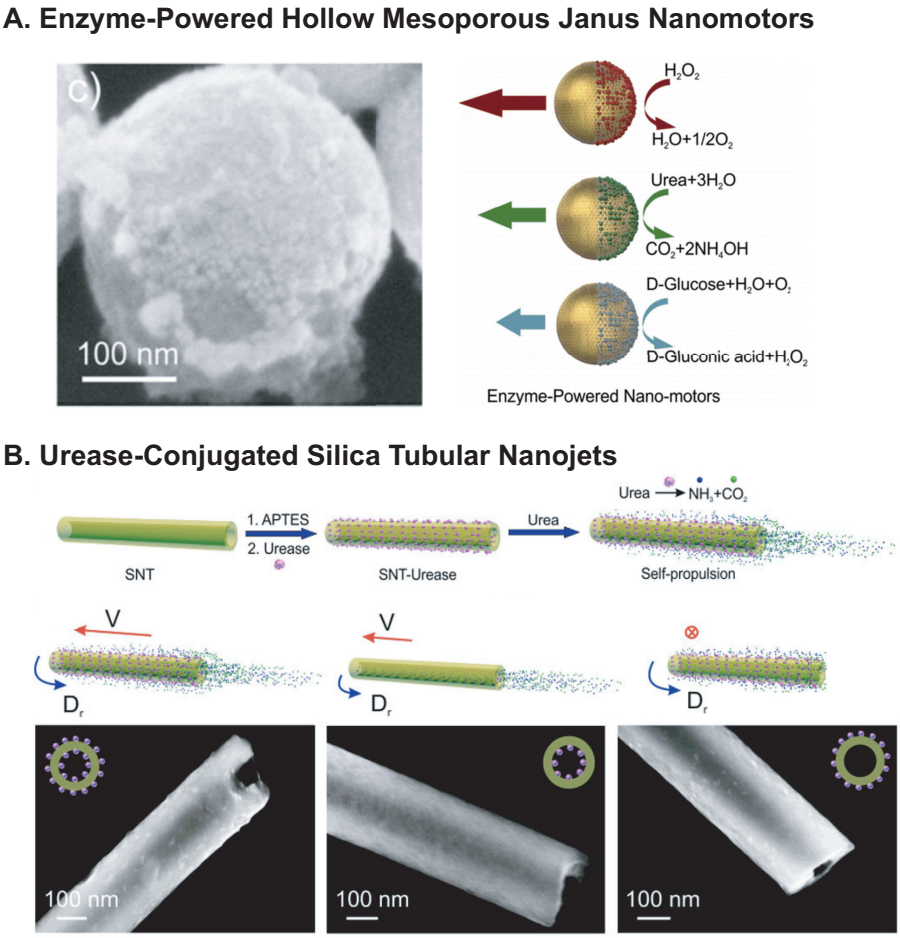

FIGURE 1.3: A) SEM image and schematic of enzyme-coated Janus hollow mesoporous silica nanoparticles. B) Schematic illustration of the fabrication of urease-conjugated silica tubular nanojets with enzyme coated all over, inside, and outside the nanotube, and their corresponding SEM images. Reprinted with permission from ref [4, 5]. Copyright 2015 American Chemical Society and 2016 American Chemical Society.

1.2 Is it real or technique artifacts?

Most of the fundamental studies on the enhanced diffusion of enzymes exploited fluorescence correlation spectroscopy (FCS) for diffusion measurements [6, 7, 9–12, 14]. Fig. 1.4 summarized all of the enzymes that had been found to perform enhanced diffusion using FCS these days. However, recently, Gunther et al. showed that typical FCS experiments might introduce artifacts for enzyme diffusion measurements, calling some of the former findings into question [16].

FCS is an indirect diffusion measurement method. It records the temporal fluctuations of the fluorescence intensity signal caused by the motion of fluorescent particles passing through a small detection volume (Fig. 1.5). Through analyzing the auto-correlation functions of these fluctuation signals, it quantifies the average number of fluorescent particles (N) inside the detection volume and also their average diffusion time (τ_D) through the volume. With the characteristic diffusion time (τ_D) and the width of the detection volume (ω_0), the diffusion coefficient can be easily deduced from Eqn 1.1:

$$D = \frac{\omega_o^2}{4\tau_D} \tag{1.1}$$

However, these fluorescence signals are highly sensitive to the environment. Fluctuation would also occur even without particle motions. Gunther et al. reviewed several circumstances in the enzyme diffusion experiments that could cause the misinterpretation of the fluctuation signal as increased diffusion [16]. They demonstrated that enzyme multimers could dissociate into smaller subunits at low concentration, which cannot be detected by FCS, but would cause an increase in diffusion. They also described that the free dyes remaining in the solution, the transient fluorescent quenching on labeled enzymes, the conformational change of

Table 1. Reports of Enhanced Enzyme Diffusion Determined with FCS Measurements in Chronological Order[a]

enzyme (species or source)	substrate or [competitive inhibitor]	D/D_0	ref
F_1-ATPase (*Escherichia coli*)	adenosine triphosphate	1.23	9
F_1-ATPase (*Escherichia coli*)	[imidoadenosine-5′-triphosphate]	1.14	9
urease (*Canavalia ensiformis*)	urea	1.28	1
catalase (*Bos taurus*)	hydrogen peroxide	1.45	10
urease (*Canavalia ensiformis*)	urea	1.3‡	11
catalase (*Bos taurus*)	hydrogen peroxide	1.3‡	11
alkaline phosphatase (bovine)	p-nitrophenyl phosphate	1.8‡	11
triose phosphatase isomerase (*Saccharomyces cerevisiae*)	D-glyceraldehyde 3-phosphate	1.0‡	11
fructose bisphosphate aldolase (rabbit)	fructose-1,6-bisphosphate	1.3‡	12
fructose bisphosphate aldolase (rabbit)	[pyrophosphate]	1.2‡	12
urease (*Canavalia ensiformis*)	urea	1.5*‡	13
acetylcholinesterase (*Electrophorus electricus*)	acetylcholine	1.2*‡	13
hexokinase (*Saccharomyces cerevisiae*)	D-glucose	1.38	14

[a] D/D_0 denotes the maximum ratio of translational diffusion constant with (D) and without (D_0) interacting substrate/inhibitor reported. Data marked by * was measured with STED-FCS, and data marked with ‡ was extracted from the corresponding figures.

FIGURE 1.4: Summary of enzymes that performed enhanced diffusion using FCS measurements. Adapted from ref [16]. Copyright 2018 American Chemical Society.

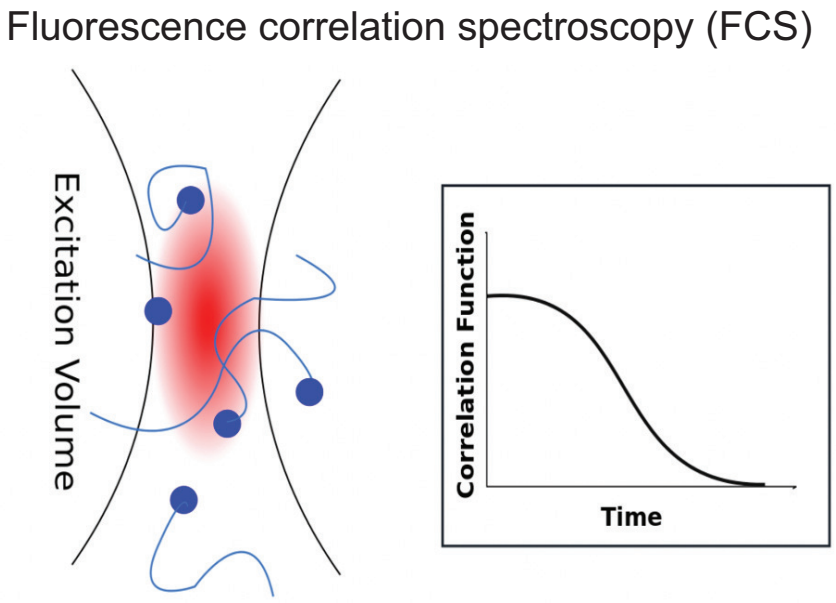

$$G(\tau)_{\mathrm{D}} = \frac{1}{N}\left(\frac{1}{1+\tau/\tau_{\mathrm{D}}}\right)\left(\frac{1}{1+(\omega_0/z_0)^2\tau/\tau_{\mathrm{D}}}\right)^{1/2}$$

FIGURE 1.5: Schematics of fluorescence correlation spectroscopy (FCS). Top left: Molecules diffusing through the excitation volume (detection volume). Top right: Typical shape of the autocorrelation function of the fluctuated signal. Bottom: Autocorrelation function: N, the the average number of detected fluorophores; τ_D, the characteristic diffusion time; ω_0, the radial radii of the detection volume and z_0, the axial radii of the detection volume. Top part adapted from ref [17].

enzymes during catalytic turnover and the binding and unbinding between enzyme and substrate would also cause changes in FCS signals which were similar to enhanced diffusion. Experts agree that interpretation of autocorrelation curves is complicated and requires modeling to fit properly. Yet, prior reports all have fit data with the assumption of normal, free diffusion of enzymes. It is imperative that these results are verified and recapitulated with distinct experimental methods.

In an attempt to test if the enhanced diffusion is real or just a result of experimental artifacts, researchers have employed a variety of alternative techniques to provide complementary measurements for enzyme diffusion [18–21]. Some new techniques refuted the prior reported enhanced diffusion of several enzymes. For example, aldolase measured by dynamic light scattering (DLS) [18] or nuclear magnetic resonance (NMR) [19], and alkaline phosphatase detected by anti-Brownian electrokinetic (ABEL) trap [21], both showed no enhanced diffusion, making this emergent research field even more controversial.

1.3 Highly programmable DNA origami

Besides enzyme proteins, DNA molecules are another group of biological materials that exhibits remarkable attributes in living cells. Their unique capabilities of programmable molecular recognition enable them the prominent building blocks for self-assembly of well-defined nanostructures. DNA origami technology, adopting the highly programmable nature of DNA molecule developed in the past decades, affords for seemingly infinite customized designs ranging from tens of nanometres to sub-micrometres (Fig. 1.6B-G) [23, 29–32]. The basic concept of DNA origami is as follows: a long, circular strand of DNA called scaffold is folded by $\sim$ 200 single-stranded DNA oligomers (staples) into a prescribed three-dimensional shape via

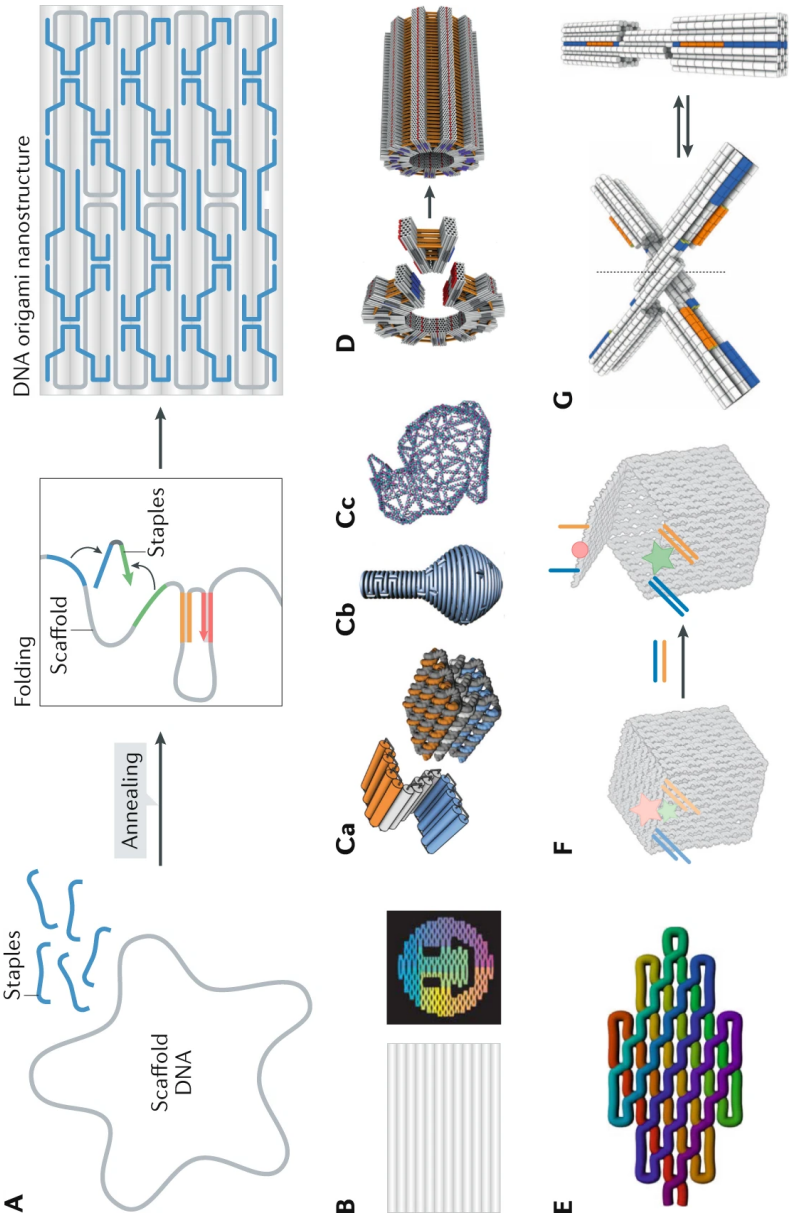

FIGURE 1.6: A) Principle of classic DNA origami. B-G) Representative DNA origami structures: B) Examples of 2D planar DNA origami shapes [22]. C) 3D nanostructures depicting a honeycomb lattice [23] (part Ca), a structure with complex curvature [24] (part Cb) and a wireframe structure with arbitrary shape [25] (part Cc). D) Superstructures hierarchically assembled from multiple DNA origami structures [26]. E) Single-stranded DNA/RNA origami [27] F,G) Examples of dynamic DNA origami nanostructures: a DNA origami box whose lid is initially locked by two DNA duplexes and can be opened via strand displacement by oligonucleotide keys (part F)[28] and a dynamic nanodevice switchable between two conformations (part G) [29]. Adapted from ref [30]. Springer Nature Limited.

base pairing (Fig. 1.6A) [22]. Each of the staple is programmed with a unique sequence, that brings together specific regions of the scaffold to form the desired geometry. Staples can also be designed with a 'sticky end', that extends out from the DNA origami structure to bind with other molecular components (e.g., fluorophores or enzymes). This way, nearly every position on the folded structure can be functionalized independently with nanoscale precision.

Exploiting the highly programmable nature of DNA origami and combining with the emergent active enzymes, we can create a new suite of programmable self-propelled active particles using enzymes as the propulsive units. We can couple a precise number of enzymes on specific positions (near-atomic-level) of the DNA origami structure to study the mechanism of propulsion from the bottom-up. We can also design nanoscale DNA origami probes to investigate the non- equilibrium thermodynamics of active enzyme bath.

1.4 Outline

In this thesis, we first demonstrated our recent findings about enhanced enzyme diffusion using a complementary method in Chapter 2. We used single-molecule imaging to directly image and track the motion of each individual enzyme, which contributed some new insights into this puzzle [13]. However, no method was perfect, single-molecule imaging also has its own caveats. So, we dissected the possible caveats in our prior work in Chapter 3 by tethering urease on a fluid lipid surface and Chapter 4 by constructing a simplified experimental chamber setup. We also compared two different data analysis approaches for single particle tracking (SPT) experiments in Chapter 4. In Chapter 5, we tried to combine the enzymes with

highly programmable DNA origami to create a new suite of programmable, self-propelled, active particles and study mechanism of propulsion from the bottom-up. Finally, in Chapter 6, we proposed some prospective ideas that combines enzyme, lipid and DNA origami together for future investigations.

Chapter 2

Direct single molecule imaging of enhanced enzyme diffusion

2.1 Introduction

Enzymes are reactive nano-scale biomolecules that use energy to perform a variety of tasks required for the basic functions of cells. Enzymes catalyze numerous reactions that are essential to maintain cellular temperature, basic metabolism, and active mixing of the crowded and visco-elastic environment inside cells [33, 34]. When enzymes are bound to the surface of nano-scale or micro-scale colloidal particles, these particles become active and self-propelled in the presence of reactant molecules (substrate) [4, 35, 36]. Thus, enzymes have been shown to act as a source of propulsion to move large-scale objects in aqueous media.

Recent experimental studies have demonstrated that enzymes could diffuse faster in the presence of their corresponding enzymatic substrates, which is termed *enhanced diffusion* [6–8, 12, 16, 37–39]. Prior studies of enhanced diffusion measured a relative increase in the diffusion coefficient from 20% to 80%, depending on the enzyme type used and the substrate concentration [6–8, 12, 16, 37–39]. A major drawback of prior measurements is that they all used a single method: fluorescence

correlation spectroscopy (FCS). In FCS, the diffusion coefficient is determined by measuring and analyzing the autocorrelation function of the fluctuations in fluorescence intensity due to particle motion. Although FCS is referred to as a single-molecule technique, the measurement often relies on signal from several particles [40]. Further, it is difficult for FCS to detect if diffusion is anomalously fast (super-diffusive) or slow (sub-diffusive) because it typically does not report on the mean squared displacement of the particles [41]. Recently, Gunther et al. showed that typical FCS experiments might introduce artifacts in diffusion measurements for enzymes, calling some of the former findings into question [16].

Here, we use direct single molecule imaging to visualize the trajectories of diffusing enzymes in solution over time, calculate the mean squared displacements (MSD), test if the enhanced diffusion is anomalous, and determine the diffusion coefficients. Our method has the added value that it is truly single molecule and mobility increases are obvious by eye.

2.2 Method

2.2.1 Enzyme preparation

Urease from Jack Bean was purchased from TCI Chemicals. Aldolase from rabbit muscle was purchased from Sigma Aldrich. Green fluorescent protein (GFP) was purified following a standard protocol for His-tagged protein purification. Enzymes were fluorescently labeled with Alexa Fluor 647 C_2 maleimide (Thermo Fisher) using a commercially available protein labeling kit (Thermo Fisher) following the optimized protocols provided by vendor. Inhibited urease was made by incubating urease with pyrocatechol (Sigma) at a 1:1000 mole ratio for 48 h to ensure fully inhibition. The urease activity assay was performed following a published protocol

in Ref.[42]. Briefly, we used phenol red as an color indicator, which turned from yellow to red as pH increased, to estimate the urease activity. 1ml assay mixture contained 10 nM urease, 28 μM phenol red, 1mM urea, and 1$\times$ PBS buffer. We measured the absorbance at 560 nm every 6 seconds to quantify the color-changing rate using UV-vis spectroscopy.

2.2.2 Methylcellulose/Pluronic F127 chamber setup

Experimental flow chamber were made by microscope slides (FisherBrand, Thermo Scientific), silanized cover slips (22$\times$30mm, No. 1.5 Thickness, FisherBrand, Thermo Scientific), and double stick tape. Briefly, two pieces of double stick tape were sandwiched between a slide and a cover slip, acting as a spacer and forming a 5-mm-wide flow channel in middle. The chamber volume was limited to $\sim$ 10 μl by the width of the flow channel and the thickness of the tape (80 $\sim$ 100 μm in height). Cover slips were silanized with dimethyldichlorosilane before using to make the surface homogeneously hydrophobic. For silanization, coverslips were first cleaned with ultra-violet and ozone (UVO) for 20 min, followed by soaking in acetone for 1 hr, 1 mM KOH for 15 min, and allowed to air dry. Cleaned, dry coverslips were then immersed in 2% dimethyldichlorosilane (GE Healthcare, Wauwatosa, WI) for 5 min to be silanized. Fully silanized cover slips were ready to be used after washing with distilled water and allowed for air dry. We coated the interior of the flow chamber with a block-copolymer to prevent enzymes from sticking to the surface. Basically, 10 ul 5% (w:v) Pluronic F-127 (Sigma) in 1$\times$PBS buffer (diluted from 10$\times$ phosphate buffered saline, Sigma) was flowed into the chamber and incubated for 5 min before loading the imaging mixture. The imaging mixture contains $\sim$ 100 pM desired enzymes/GFP, urea of proposed concentration/1$\times$ PBS buffer, an oxygen scavenging system (10 mM dithiothreitol (DTT), 15 mg/ml glucose, 0.15 mg/ml

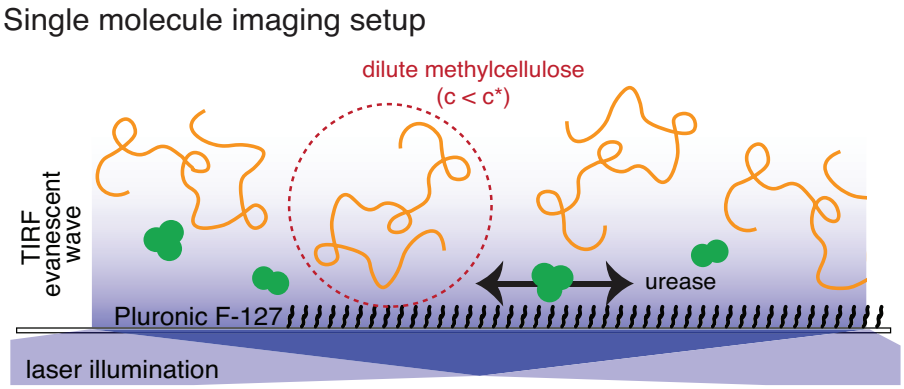

FIGURE 2.1: Experimental setup for single particle imaging of urease using TIRF (blue) of fluorescent urease (green) in a chamber with Pluronic F127 (black) coating the surface and dilute methylcellulose polymers to slow down the mobility (orange). Radius of gyration of methylcellulose (dashed red circle, $\sim$ 30 nm) represented [43].

catalase, and 0.05 mg/ml glucose oxidase) to extend the lifetime of the fluorescent dyes and minimize photobleaching, and 0.6% (w:v) methylcellulose (88 kD, Sigma), as a viscous agent to slow down the diffusion and facilitate tracking (Fig. 2.1). All chambers were imaged using a custom-built TIRF microscope immediately after loading and kept measuring for a maximum of 30 minutes before discarding.

2.2.3 TIRF imaging

Single-particle imaging was performed using total internal reflection fluorescence (TIRF) microscopy with a custom-built laser system (50 mW 488 nm laser and 100 mW 638 nm laser from CrystaLaser) constructed around a Nikon Ti-E microscope. Imaging was performed with a 60$\times$, 1.49 NA TIRF objective (Nikon), and then magnified an additional 2.5$\times$ before being projected onto an EM-CCD camera (IXON electron-multiplier CCD, Andor). The camera had 512 $\times$ 512 square pixels of 16.2 μm on each side, giving a final magnified pixel size of 107 nm/pixel. Movies were

recorded at a rate of 8-13 frames/s ($\Delta t = 80 - 130$ ms/frame, ROI = 512×512 pixels) with a 50-100 ms exposure using the Nikon Elements software. Laser power and EMCCD gain settings were kept constant for all movies.

2.2.4 Data analysis

Movies from the Nikon Elements software were opened in ImageJ/FIJI using the BioFormats Importer plugin. Registration was performed using the StackReg plugin based on fluorescent proteins that were affixed on the cover glass to eliminate drift. Registered movies were then analyzed by ParticleTracker 2D/3D plugin to track visible particles in the movie for all frames [44]. In the ParticleTracker plugin, the particle size was set to be 3-5 pixels, the cutoff was 0.001, the percentile was 1%-5%, and link range was 4, the displacement was 4-6, and the dynamics type was chosen to be Brownian for optimal tracking of all possible trajectories. Position and time information of the particle in each trajectory were then generated after tracking.

Particle trajectory information was analyzed by a self-programmed MatLab code based on @msdanalyzer [45], which calculated the mean square displacement and fit only the first 25% of each track to get the α exponent and diffusion coefficient for each trajectory. Individual α exponents and diffusion coefficients were then used to create the probability distribution function(PDF) histograms for each urea concentration. The distributions of α exponent were normal and were directly fit with a Gaussian to get the mean for each case and were shown in Fig. 2.2. Error bars represented the standard error of the mean.

The probability distributions of diffusion coefficient originally showed as log-normal form for each case. So, we log transformed each diffusion coefficient and got the PDF of log(D) for different urea concentrations. And after log-transformation,

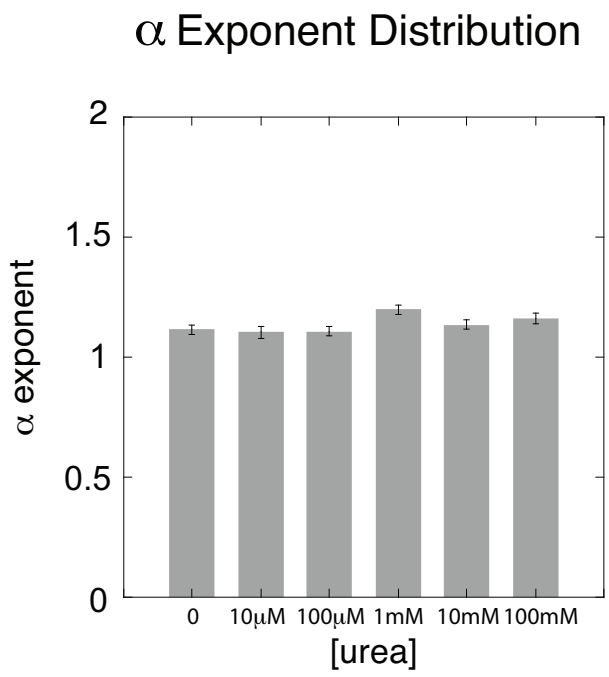

FIGURE 2.2: The means of α exponent under different urea concentrations. Error bar shows the standard error of the mean.

the PDF of log(D) showed as a normal distribution as expected. These PDFs were then fit to a Gaussian as depicted in Eqn 2.1.

Gaussian fit equation:

$$PDF = A \times \exp\Big[-\frac{(log(D) - < log(D) >)^2}{2\sigma^2}\Big], \tag{2.1}$$

The mean of each Gaussian fit was then transformed back, acting as the median for the original log-normal distribution, and was used as the effective diffusion coefficient for each urea condition. Error bars are obtained from the standard error of the each Gaussian fit. The top of the error bar was determined from adding the mean by the standard error to determine the right-most edge of the Gaussian width and then taking that as the power of 10 to transform it back to D. The bottom of the error bar was determined by the same way except subtracting the standard error.

All fit parameters are given in the Appendix A.

ParticleTracker plugin can also report the α exponent and general diffusion coefficient for each trajectory, using the similar method as our MatLab code. It calculated the mean squared displacements, plotted in log-log scale and fit the first 25% data points to a linear line. We also compared the diffusion coefficient reported by the plugin with the result obtained by our MatLab code. Both methods gave results within error of each other.

We also analyzed the initial shape of each MSD plot based on the first 7 data points of each MSD polt using the MatLab program for both buffer (0 mM urea) and 1 mM urea conditions. We aimed to look for systematic deviations from linear trends that might indicate ballistic motion of urease molecules in the presence of urea, as previously described in the literature [46], which showed a parabolic component in MSD plot at the very beginning time part of a propelled particle. We found that the early time part of the MSD plots were sometimes linear and sometimes parabolic with either positive or negative curvature for both groups. We expected to have more or larger upward parabolic trajectories which could indicate ballistic propulsion for the group with urea. However, we found no difference between the two conditions in our data. Thus, we cannot confirm this ballistic motion claim with the current spatial and temporal resolution in our measurements.

2.3 Reliability of single-molecule imaging chamber setup

We first performed a control experiment to test the reliability of the method. We measured the diffusion coefficients of different sized proteins and see if D scales inversely with size as predicted by the Stokes-Einstein equation: $D = k_B T/6\pi\eta R$.

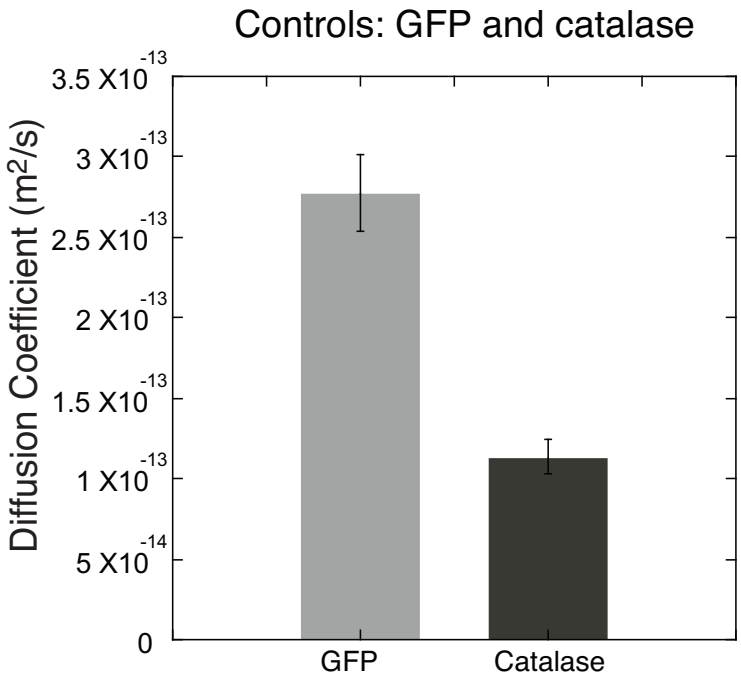

FIGURE 2.3: Diffusion coefficients of GFP (light gray bars, $N = 125$) and Alexa Fluor 488 labeled catalase (dark gray bars, $N = 25$). Error bars were determined from the standard errors of Gaussian fits as described in the Method.

We used fluorescently-labeled catalase ($R = 5.2$ nm) and green fluorescent protein (GFP, $R = 2.3$ nm). We found that the diffusion coefficient for catalase was $D_{catalase} = 1.13 \pm 0.11 \times 10^{-13}$ m^2/s, and $D_{GFP} = 2.77 \pm 0.23 \times 10^{-13}$ m^2/s for GFP. The ratio of their radii is ~ 2.3. According to the Stokes-Einstein equation, we would expect a similar ratio to be observed for their diffusion coefficients. Taking the ratio of the diffusion coefficients, we get $D_{GFP}/D_{catalase} = 2.4 \pm 0.4$, which is similar in scale as expected (Fig. 2.3).

2.4 Enhanced diffusion of urease

We next seek to quantify the diffusion of active urease under different urea concentrations using our single-molecule imaging experimental setup. To test for anomalous diffusion, MSD data were first plotted on log-log scale and fit to the power-law equation: $\langle(\Delta r)^2\rangle = \Gamma t^{\alpha}$, where t is the lagtime, Γ is the generalized diffusion coefficient, and α is the anomalous diffusion exponent (Fig. 2.4C). We found that α was on average equal to one for all data, implying that the diffusion we measure was not anomalous (Fig. 2.2, Fig. 2.4C). Since the MSD was linear with time, we can then deduce the diffusion coefficient, D, of urease from the slope of the MSD plot according to the Einstein's equation in 2D: $\langle(\Delta r)^2\rangle = 4Dt$, (Fig. 2.4C).

In agreement with prior work, we find that urease displays enhanced diffusion in the presence of its substrate, urea (Fig. 2.4C). The change in mobility is visible directly from trajectories and the MSD plots (Fig. 2.4A-C). For our assays, we measure over 100 single particle trajectories for each experimental condition to obtain statistically significant data. Diffusion data display a log-normal distribution that could be plotted and fit with a Gaussian after log-transformation (Fig. 2.5A). The mean of the Gaussian fit represents the median of the original log-normal distribution, which is then transformed back and used as the effective diffusion coefficient measured for each case.

Interestingly, we find that the relative increase of the diffusion coefficient in our single molecule experiments is significantly higher than those previously reported using FCS methods [6, 38]. For the highest concentration of urea we tested (100 mM), we find a $\sim$ 3 fold increase in the diffusion constant (Fig. 2.5B), compared to prior results that showed only a $\sim$ 30% increase [6, 38]. We also performed control experiments with green fluorescent protein and inhibited urease that cannot interact

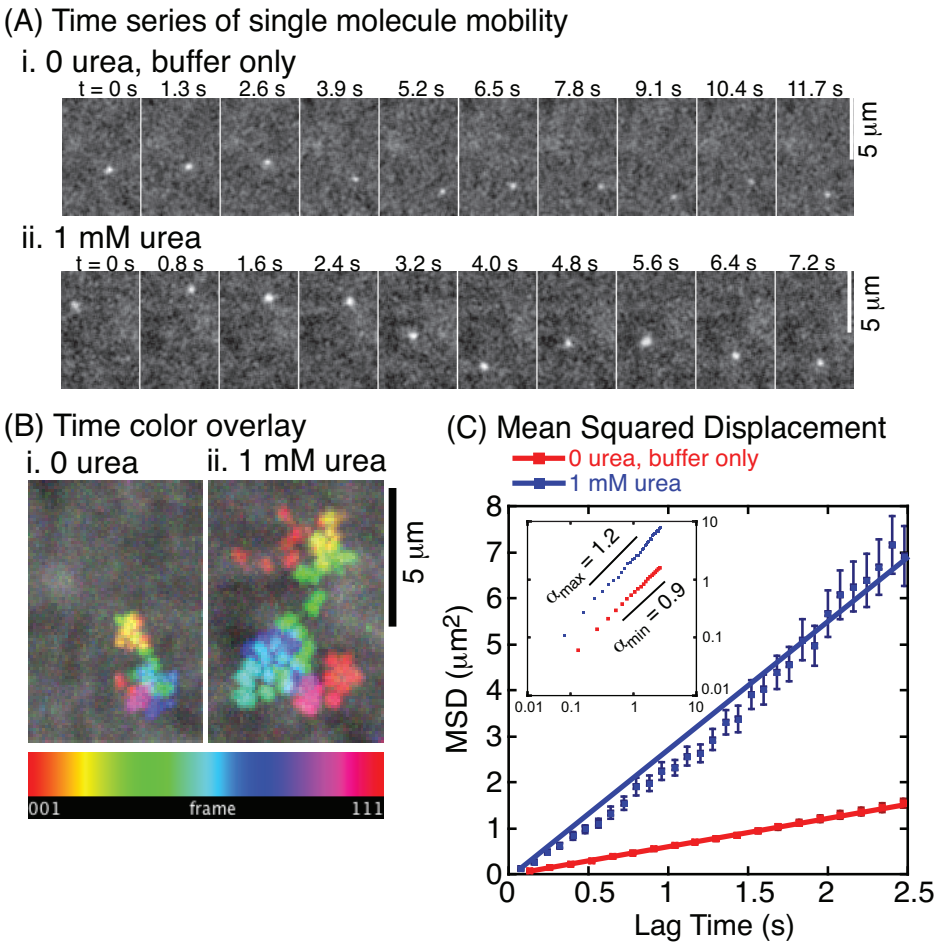

FIGURE 2.4: A) Example trajectories of single urease enzyme over time i) without urea, and ii) with urea at 1 mM. Scale bar 5 μm. Time interval given for each frame. B) Example 2D trajectories displayed as collapsed images with rainbow scale representing time as given in the time color bar over 111 frames with i) 0.13 s between frames for urease without urea, and ii) with 0.08 s between frames for urease with 1 mM urea. Scale bar 5 μm. C) Time-averaged MSD plot of each trajectory, fit with a linear equation to determine the diffusion coefficient, D. Inset: Same MSD data plotted on log-log scale. Black lines represent the range of α exponent values: $\alpha_{max} = 1.2$, $\alpha_{min} = 0.9$. (Red squares: urease without urea; blue squares: urease with 1 mM urea; error bars represent the standard error.)

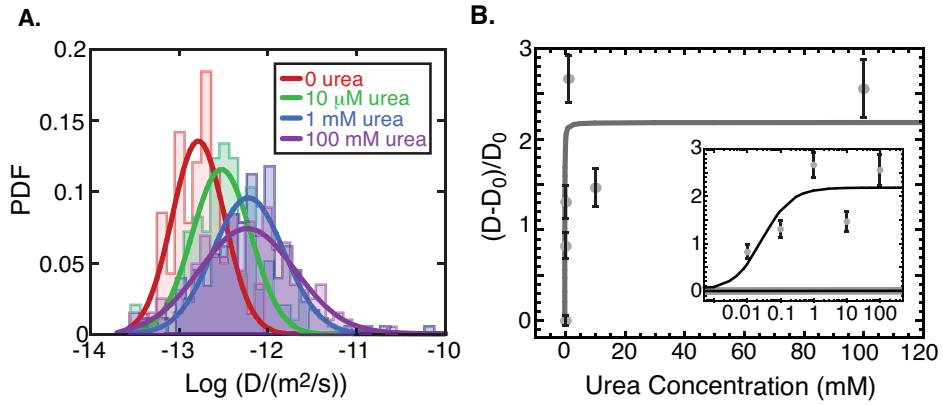

FIGURE 2.5: A) Representative probability distribution histograms of log-transformed diffusion data at different urea concentrations: 0 (red region, $N = 141$), 10 μM (green region, $N = 97$), 1 mM (blue region, $N = 178$), 100 mM (purple region, $N = 203$) and corresponding Gaussian fit lines 0 (red line), 10 μM (green line), 1 mM (blue line), 100 mM (purple line). B) The normalized relative increase in the diffusion coefficient $(D - D_0)/D_0$, plotted as a function of the urea concentration. Inset shows the same data plotted on a logarithmic scale. Solid line shows the hyperbolic fit with a characteristic concentration, K.

with urea. We measured their diffusion rates with and without the presence urea. And both show a slight decrease in D when urea was added (Fig. 2.6, Fig. 2.7). These controls demonstrate that the enhanced diffusion of urease is not due to the presence of urea in solution, but rather to the interaction between urea and urease.

We calculate and plot the relative increase in the diffusion coefficient as a function of urea concentration (Fig. 2.5B). The data displays a hyperbolic dependence of the form: $(D - D_0)/D_0 = A \times \frac{[urea]}{[urea]+K}$, where D is the measured diffusion coefficient, D_0 is the diffusion coefficient in the absence of substrate, A is an amplitude, $[urea]$ is the urea concentration, and K is the characteristic concentration required for 50% activity. The hyperbolic relationship represents a well-known biochemical model for substrate consumption by enzymes, called the Michaelis-Menten function. We find that the best fit has $K = 30 \pm 30$ μM (all fit parameters available in Supplemental Information).

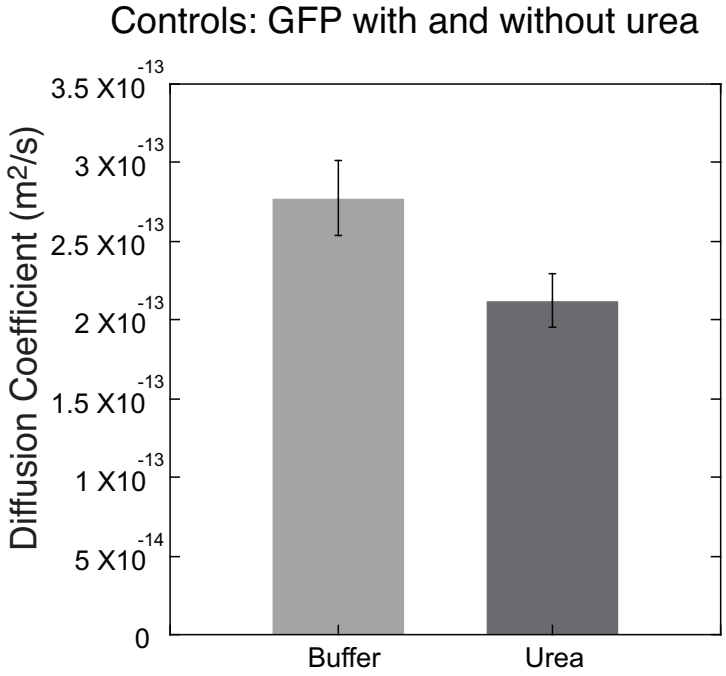

FIGURE 2.6: Diffusion coefficients of GFP without urea (light gray bars, N = 125) and with 1 mM urea (dark gray bars, N = 106). Error bars were determined from the standard errors of Gaussian fits as described in the Method.

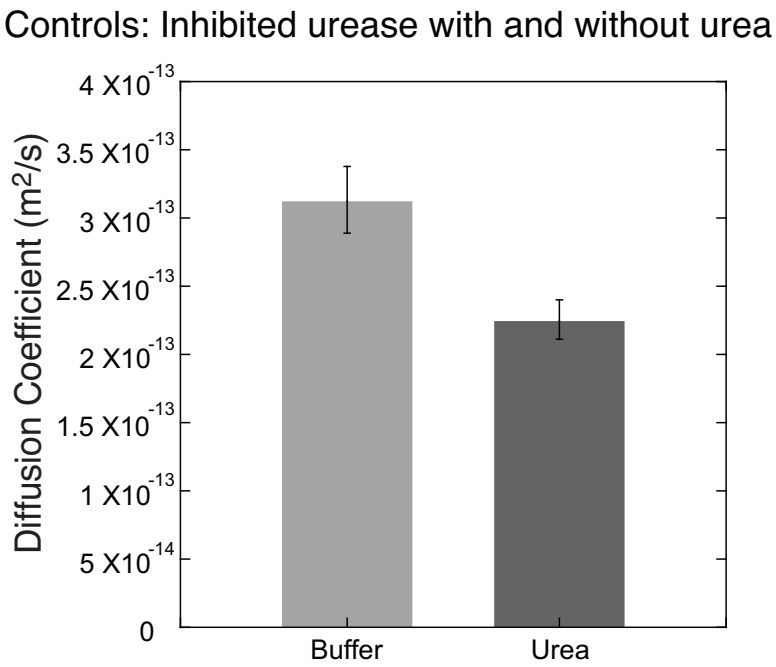

FIGURE 2.7: Diffusion coefficients of inhibited urease without urea (light gray bars, N = 120) and with 1 mM urea (dark gray bars, N = 118). Error bars were determined from the standard errors of Gaussian fits as described in the Method.

The equilibrium dissociation constant, K_D, is the concentration required for half of the maximum urea binding to urease and was previously reported as 250 μM [47]. The Michaelis-Menten constant, K_M, is the urea concentration required for half the maximum reaction rate of urea consumption by urease and was reported as 3 mM [48]. Comparing our results to these two rate constants, we find that our data is more similar to the binding coefficient, K_D, instead of the reaction turn-over rate, K_M. Several theoretical models have suggested that substrate binding could change the size or flexibility of enzymes, driving the difference in the diffusion coefficient [14, 39], but no model has predicted such a large shift in the diffusion coefficient as we measured here.

2.4.1 Estimation of temperature increase in chamber due to enzyme catalytic turnover

Prior works have noticed a correlation between the diffusion coefficient increase and the heat released during enzymatic turnover [38]. Assuming the enzyme size does not change during the turnover, in order for the diffusion coefficient to increase by a factor of 3, as we observed (Fig. 2.5B), the temperature would need to increase by 55K locally. This increase was estimated by using the Stokes-Einstein relation: $D = \frac{k_B T}{6\pi\eta R}$, in which the viscosity, η, is also considered as a function of temperature: $\eta(T) = 2.4 \times 10^{-5} Pa \cdot s \times 10^{247.8K/(T-140K)}$ for water [49]. Below we estimate the heat released from enzymes under two scenarios: 1) the local heat released around a single enzyme; 2) the global heating of the entire chamber by many enzymes.

Local Heating Estimate. We first estimate the temperature increase around a single enzyme using the heat diffusion equation with an instantaneous point source

[38]. Since the concentration of the enzyme was extremely low ($\sim$ 100 pM), each single enzyme is modeled as an instantaneous point source of heat during each enzymatic turnover. Thus, we have:

$$\Delta T(r,t) = \frac{\Delta Q}{\rho c(4\pi\kappa t)^{3/2}} \exp\big[-\frac{r^2}{4\kappa t}\big], \tag{2.2}$$

where $\Delta Q = 25 k_B T$ is the heat released from a single catalytic reaction. The background material is water with specific heat capacity $c = 4.18$ J/(K·g), density $\rho = 1$ g/cm^3, and thermal diffusivity $\kappa \simeq 10^{-7}$ m^2/s. We estimate the temperature increase during one catalytic turnover, with $t = t_c = 1/k_{cat} \simeq 10^{-4}$ s for urease at saturating urea concentration and used a distance comparable to enzyme size with $R = 2$ nm. We find the temperature shift would be minuscule, $\Delta T \sim 10^{-11}$ K, so it seems unlikely that heating the local environment alone could cause such a large increase in the diffusion coefficient.

Chamber Heating Estimate. Another model estimates the entire heating of the whole chamber due to many enzymes in the solution [50].

In this model, the characteristic heat diffusion time is determined as $\tau_{esc} = l^2/\kappa$, where $l = 100$ μm is the characteristic diffusion distance travelled by the heat to exit the system, approximated as the smallest length of the experimental chamber, and κ is the heat conductivity of water. Thus, we can use the heat generated during time τ_{esc} to estimate the general temperature increase in our system:

$$\Delta T_{total} = Q_{tot}/V c_v. \tag{2.3}$$

The total heat released during that time is $Q_{tot} = N\Delta Q k_{rxn} \tau_{esc}$, N is the number of reacting enzymes, $V = 10$ μl is the volume of the system, and $c_v = 4.2 \times 10^6$

J/(K·m^3) is the volumetric heat capacity of water. For our system, the escape time $\tau_{esc} = 0.1$ s. The enzyme concentration in our system is ~ 100 pM. If we suppose all of the enzymes are reacting with the substrate during this time, we have $Q_{tot} \sim 10^{-7}$ J, and the corresponding temperature increase in our system is $\Delta T_{total} \sim 10^{-6}$ K, which is too small to account for the large increase in diffusion coefficients.

Combining with the other heating estimations previously made by [38, 50], the temperature increase ΔT for urease ranges from 10^{-11}K to 0.09K. These T increases are too small to account for the factor of 3 increase in diffusion that we observed.

2.4.2 Collective heat effect and collective hydrodynamic flow effect

In prior estimations of temperature changes, the enzymes each act as an independent source of heat or activity. Two recent models have taken collective effects of many enzymes into account. One is a collective heating model [50] and another is a collective hydrodynamics model [51]. Both of these models predict that the diffusion rate increase will depend linearly on the total concentration of the enzymes in solution.

Collective Heating This theoretical hypothesis assumed that the local temperature increase around a single enzyme could be high enough to denature the enzymes during the reaction, in addition to chamber heating (described above) [50]. It predicted a linear relationship between the relative diffusion increase $\Delta D/D_0$ and a dimensionless quantity:

$$\delta = \frac{Ql^2}{\kappa T}\frac{k_0 S C_e}{K_M + S}, \tag{2.4}$$

called the strength of collective heating, where S is the substrate concentration, and C_e is the total enzyme concentration. Thus, it takes into account the hyperbolic dependence on substrate concentration, S, with characteristic reaction concentration, K_M (Michaelis-Menten constant) as observed in our experiments. This model predicts that the relative increase in diffusion coefficient $\Delta D/D_0$ should be proportional to the total enzyme concentration, C_e.

Collective Hydrodynamics. Another hypothesis was based on the collective hydrodynamics effects [51]. Specifically, if enzymes are interacting with their substrate, they can act as a force dipole that affects the fluid field around it. At low Reynolds number, such change in flow would influence the motion of other molecules (passive or active) at larger distances than expected. The change in the diffusion coefficient due to such a hydrodynamic collective effect can be written as:

$$D_{hydro} = \zeta \frac{S_A C_e}{l_c \eta^2}, \tag{2.5}$$

where ζ is a dimensionless factor computed from the Green's function for the hydrodynamic coupling, l_c is a cutoff length scale, C_e is the concentration of enzymes, η is the liquid viscosity, and S_A is the active component of correlation function due to the activity, and can be estimated by $S_A \sim m^2 \tau_{rxn}$, where m is the force dipole formed by the enzyme and τ_{rxn} is the reaction time, which equals one over the reaction rate ($\tau_{rxn} = k_{rxn}^{-1}$) for saturating substrate conditions. Thus, it also predicts that the relative increase in diffusion coefficient $\Delta D/D_0$ should be proportional to the total enzyme concentration, C_e.

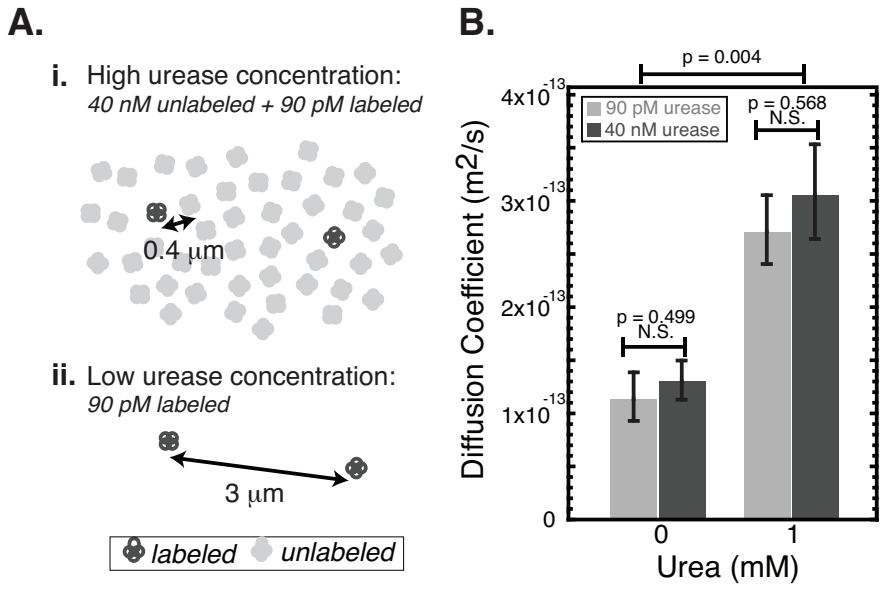

FIGURE 2.8: A) i. Cartoon of 40 nM urease with average spacing between molecules of 400 nm. ii. Cartoon of 90 pM urease with average spacing between molecules of 3 μm. B) Diffusion coefficients of urease at 40 nM urease concentration (dark gray bars) without urea (N = 31) and with 1 mM urea (N = 35), or urease at 90 pM (light gray bars) without urea (N = 30) and with 1 mM urea (N = 36). Error bars are determined from the standard errors of the mean of the Gaussian fits.

To test the predictions of these collective models, we repeat our experiments at two different total enzyme concentrations, 40 nM and 90 pM (Fig. 2.8). For both groups, we keep the concentration of labeled enzyme constant at the single molecule level (90 pM). The average spacing between enzymes depends on their concentration in solution, which we estimate as $\sim$ 400 nm for 40 nM and $\sim$ 3 μm for 90 pM (Fig. 2.8Ai)-ii). We compare the diffusion coefficients for different concentration groups in the absence of urea or with 1 mM urea (saturating concentration, Fig. 2.5B). We find no difference in the diffusion constants between 40 nM and 90 pM concentrations for either the buffer case or urea case (Fig. 2.8B). Although the proportional relationship between diffusion and total enzyme concentration is not

observed in our experiments, it is possible that collective phenomena would come into play at much higher, non-physiological concentrations of enzymes. Regardless, these collective models cannot explain the 3-fold increase in diffusion that we observe in our experiments.

2.4.3 Oligomerization state of urease with and without the presence of urea

Diffusion coefficients can also be significantly altered due to the dissociation of enzyme complexes at the low concentrations used in FCS or single molecule studies, as described above [16].

Suppose an enzyme with radius R undergoes a change in size, δR, during its interaction with the substrate, the liquid viscosity remains the same. From the Stokes-Einstein equation, the relative change in diffusion can be written as

$$\frac{\Delta D}{D_0} = \frac{1}{1+\frac{\delta R}{R}}\frac{T}{T_0} - 1. \tag{2.6}$$

A positive change in ΔD requires a negative change in δR, as expected. We can then estimate the size change of urease in our experiments needed to account for a 3-fold increase in diffusion. For our experiments, $\frac{\Delta D}{D_0} \sim 2$ and $\frac{T}{T_0} \simeq 1$ from the calculations above. We estimate that $\delta R \simeq -\frac{2}{3}R$, a 67% loss of radius. Considering that urease enzymes are hexamers [52], the large increase in our diffusion measurements would most likely be due to the dissociation of hexamers to smaller oligomers after interacting with urea.

Although, this dissociation process cannot be detected by FCS, it can be directly monitored using our single molecule imaging method. To directly test the oligomerization state of the urease multimers, we perform single molecule photobleaching

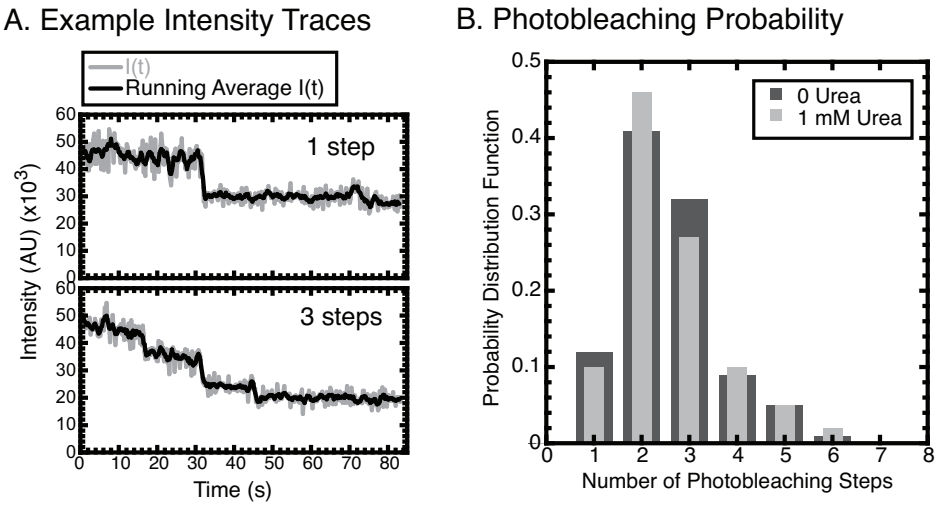

FIGURE 2.9: A) Two example intensity traces of fluorescent urease complexes photobleaching over time, showing a one-step bleach (top) and a three-step bleach (bottom). B) The distributions of photobleaching steps directly report the number of fluorescent urease monomers in each complex in the presence of 0 urea (dark gray bars, $N = 100$) and 1 mM urea (light gray bars, $N = 100$).

experiments that reveal the number of urease monomers within each fluorescent complex [53, 54]. Each urease monomer is covalently labeled with one fluorophore, on average, and there are reported to be 6 monomers per urease complex [52]. We first mix the labeled urease hexamers with urea at 0 or 1 mM concentration allowing them to react and then affix them to the cover glass. Binding to the glass stabilizes their state and makes the local laser illumination and z-height constant for the entire measurement. We use TIRF microscopy to image the enzymes without oxygen scavenging agents, so that the fluorophores photobleach over time (Fig. 2.9A).

We count the number of photobleaching steps for each fluorescent spot, which corresponds to the number of monomers in each complex, and create a histogram of the number of bleaching events for each condition (Fig. 2.9B). Urease complexes never display more than 6 bleach steps, indicating that the hexamer is the largest oligomerization state. We find that two or three monomers per complex are the

most common states for both 0 and 1 mM urea conditions. If the dissociation of the oligomer occurs due to the presence of urea, we would expect to see a large shift in the distribution of the 1 mM urea group to lower numbers of bleaching steps. However, we find no difference between these two distributions according to the Kolmogorov-Smirnov statistical test ($P = 1.0$). From these results, the enhanced diffusion we observe cannot be caused by changes in the oligomerization state of the molecule.

2.4.4 Discussion

There is a distinct possibility that our technique cannot probe, which is that the shape of the enzyme complex could significantly change from triangular, as depicted in crystal structures [52], to linear (Fig. 2.10). Because asymmetric particles are known to diffuse faster in the direction parallel to their long-axis [55, 56], shape changes like these could result in enhanced diffusion by as much as a factor of two for urease. Such large shifts in conformation could be probed in future experiments using Förster resonance energy transfer (FRET) measurements coupled with FCS or single molecule imaging. In conclusion, we use a distinct method to measure the diffusion of enzymes to test if the enhanced diffusion previously reported was genuine or an artifact of the FCS technique employed. Excitingly, we have verified that the enhanced diffusion of urease occurs on a truly single molecule level. We find that the enhanced diffusion is Brownian - not anomalous. We also observe a higher increase in diffusion rates, by a factor of three, in comparison with the $\sim$ 30% increase previously reported. The large increase in diffusion is difficult to account for based on current physical models of heat release or collective interactions. Finally,

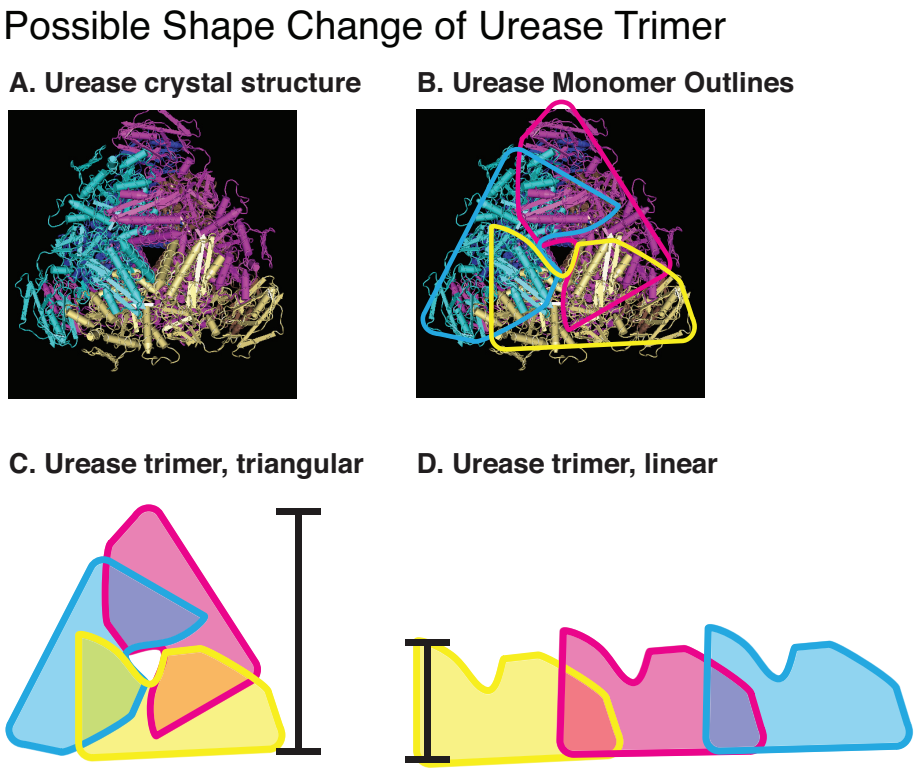

FIGURE 2.10: Example possible shape change of urease enzyme. A. Urease crystal structure from protein data bank (PDB: 3LA4) B. Urease monomer shapes outlined on protein crystal structure. C. Urease monomer shapes in triangular arrangement from crystal structure. D. Example, possible large-scale shape rearrangement that would allow for urease to diffuse faster parallel to the long-axis.

single molecule imaging techniques are able to directly measure the oligomerization state of the enzymes, excluding the possibility that the enhancement in diffusion we observe is caused by the dissociation of enzyme multimers. We expect the direct imaging technique will be a powerful, complementary method to test the predictions of future models of the mechanism behind the enhanced diffusion of enzymes.

2.5 Enhanced diffusion of aldolase

To test the enhanced diffusion for other enzymes, we made the same single-molecule diffusion measurements for aldolase. Aldolase is an endothermic enzyme (ΔH = 30-60 kJ/mol) and has a slow reaction rate (k_{cat} = 1-5 s^{-1}). It converts the substrate fructose-1,6-bisphosphate (FBP) into dihydroxyacetone phosphate (DHAP) and D-glyceraldehyde-3-phosphate (G3P). We measured the diffusion coefficient of aldolase under different concentrations of FBP solution and found an interesting two-phase changing behavior as shown in Fig. 2.11. At lower FBP concentrations, the diffusion of aldolase actually slowed down as more FBP was added. However, when FBP was more than 10 mM in the solution ([FBP] $>$ 10 mM), a faster diffusion was observed as the concentration of FBP further increased. At the highest FBP concentration (100 mM) we measured, the final relative increase in D was $\sim$ 30% (Fig. 2.11B), which was in agreement with the previous FCS findings [14]. This two two-phase changing of D implied that the diffusion of aldolase might be regulated by multiple factors. These factors competed with each other and elaborated together to contribute to the final diffusion behavior observed. Hypothetical factors might include the heat exchange with the environment, the slight conformational change during the catalytic turnover or some other unknown hydrodynamic effects, that deserved further investigation. Recently, some other studies using different diffusion measuring techniques such as dynamic light scattering (DLS) [18], nuclear magnetic resonance (NMR) [19] and STED-FCS [20] showed no enhanced diffusion for aldolase with the presence of FBP, making this field even more controversial.

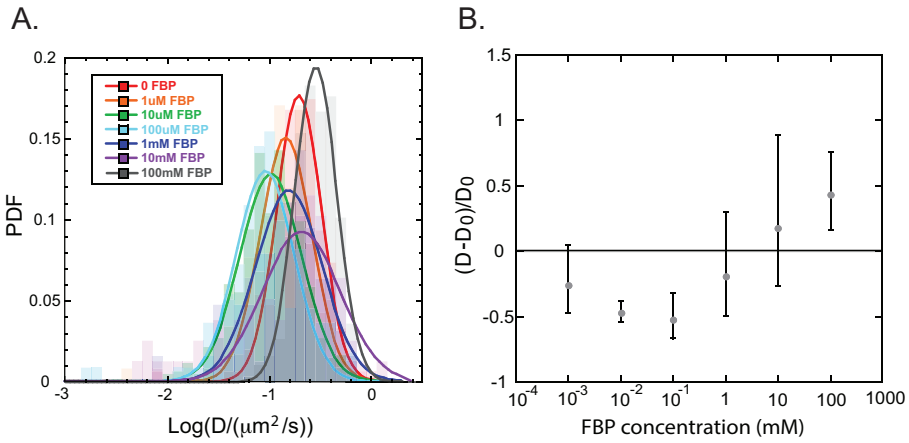

FIGURE 2.11: A) Representative probability distribution histograms of log-transformed D at different FBP concentrations: 0 (red region, N = 149), 1 μM (orange region, N = 117), 10 μM (green region, N = 594), 100 μM (blue region, N = 110), 1 mM (dark blue region, N = 63), 10 mM (purple region, N = 78), 100 mM (gray region, N = 306), and corresponding Gaussian fit lines 0 (red line), 1 μM (orange line), 10 μM (green line), 100 μM (blue line), 1 mM (dark blue line), 10 mM (purple line), 100 mM (gray line). B) The normalized relative increase in the diffusion coefficient $(D - D_0)/D_0$, plotted as a function of the FBP concentration.

2.6 Conclusion

In conclusion, we used a distinct method to measure the diffusion of enzymes to test if the enhanced diffusion previously reported was genuine or an artifact of the FCS technique employed. Excitingly, we verified that the enhanced diffusion of urease occurred on a truly single molecule level. We found that the enhanced diffusion was Brownian - not anomalous. We also observed a higher increase in diffusion rates, by a factor of three, in comparison with the $\sim$ 30% increase previously reported. The large increase in diffusion was difficult to account for based on current physical models of heat release or collective interactions. To test if the huge enhancement was caused by the dissociation of enzyme multimers, we directly measured the oligomerization state of the enzymes using single molecule imaging techniques, and excluded this possibility. Finally, we applied the same single-molecule diffusion measurements on aldolase, a slow and endothermic enzyme. We observed a two-phase changing of aldolase diffusion behavior: a reduced diffusion at low substrate concentration and a $\sim$ 30% enhanced diffusion at high substrate concentration. We expected the direct imaging technique will be a powerful, complementary method and contribute new insights into the future investigations of the mechanism behind enhanced enzyme diffusion.

Chapter 3

Enhanced diffusion of urease tethered to supported lipid bilayer

3.1 Introduction

In the prior chapter, we verified the enhanced diffusion of urease in the presence of its substrate, urea, by using a direct single-molecule imaging method with total internal reflection fluorescence (TIRF) microscopy. We found that the overall mobility of each individual active urease was increased by 2–3 fold at saturated substrate concentration, while diffusion remained Brownian. Although we were able to recapitulate the enhanced diffusion of enzymes using SPT, there were caveats to this method: (1) We recorded the 2D projections of 3D trajectories. Specifically, the TIRF microscope exploits the total internal reflection of incident light to form an evanescent field immediately adjacent to the interface between the specimen and the glass coverslip. Thus, only fluorophores within the 200-nm excitation region above the surface are capable of being excited, which makes single-particle imaging possible. The motion in z-direction (perpendicular to the interface) is totally lost. (2) Polymers in solution and on the surface might have unquantifiable effects on enzyme diffusion. In our prior work, to slow down the enzyme mobility and facilitate

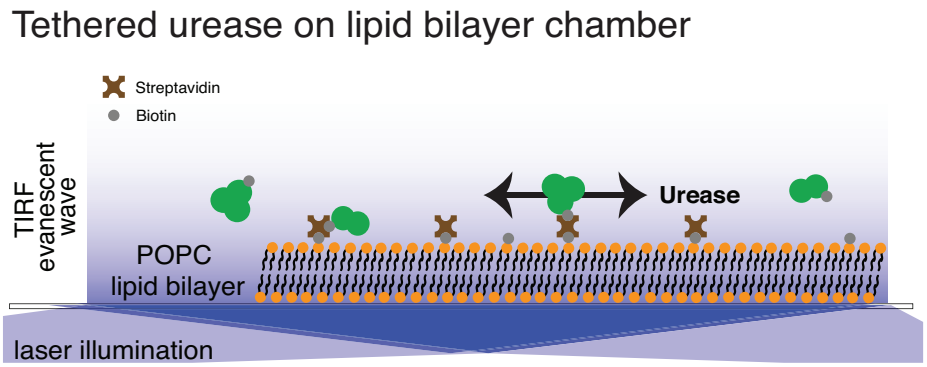

FIGURE 3.1: Schematics of tethered urease experimental chamber design in which biotin modified urease is tethered on a biotinylated SLB via biotin(gray)-streptavidin(brown) interactions.

tracking, we introduced a surface polymer coating (Pluronic F127) and a viscous polymer (methylcellulose) to our experimental chamber. The presence of these additives indeed slowed down the enzyme mobility enough for accurate tracking, but also raised concerns of their potential, unknown effects on enzyme diffusion that were not easily quantifiable.

Here, we dissect the experimental caveats of our prior work, and compare different experimental designs as well as data analysis approaches of direct single-molecule imaging of enzyme diffusion measurements. We first tether urease directly to a supported lipid bilayer (SLB) to constrain the enzyme diffusion to two dimensions (Fig. 3.1). We measure the diffusion of tethered urease with and without urea, and show a 3-fold enhancement in the diffusion of urease, as we observed before in in Chapter 2.

3.2 Method

3.2.1 Fluorescent labeling and biotin modification of urease

Urease from Jack Bean was purchased from TCI Chemicals. Enzymes were fluorescently labeled with Alexa Fluor 647 C_2 maleimide (Thermo Fisher) and biotinylated using a commercially supplied EZ-Link Sulfo-NHS-LC-Biotinylation kit (Thermo Fisher) following the instructions provided.

3.2.2 Biotinylated supported lipid bilayer (SLB)

The supported lipid bilayers are made by fusing small unilamellar vesicles (SUVs) on the chamber surface [57]. Biotinylated SUVs are made of POPC (1-palmitoyl-2-oleoyl-glycero-3-phosphocholine) and ∼0.1 mol% biotin-PE (1,2-dioleoyl-sn-glycero-3-phosphoethanolamine-N-(cap biotinyl)) purchased from Avanti. First, 50 μl of 10 mg/ml POPC and 5 μl of 0.1 mg/ml biotin-PE were added in 50 μl of chloroform and mixed well. Chloroform is then evaporated from the mixture under a gentle stream of N_2 gas for 10 min. The lipid mixture is further dried out in a vacuum desiccator for 30 min. The dried lipid is rehydrated in 100 μl PBS buffer and vortexed for 1 min to form giant unilamellar vesicles (GUVs). The white opaque GUV suspension is then sonicated using a sonicator microtip probe (Sonifier) for 3 min to form a clear SUV solution. This clear SUV solution is stored at 4°C and used for the SLB surface coating.

3.2.3 Tethering urease on SLBs via biotin-streptavidin

Tethering multi-streptavidin-urease complexes on biotinylated SLBs

5.38 μM Alexa647-biotin-urease is mixed with a 2-fold molar excess of streptavidin(SA) and incubated on ice for 1 hr to form SA-Alexa647-biotin-urease complexes. The reaction mixture is then diluted by 10,000 times to make the enzyme concentration optimized for single particle imaging. For biotinylated SLB-coated flow chambers, 7 μl of biotinylated SUV solution is first flowed in and incubated for 20 min to allow for the fusion of SUVs to the surface. Excess unfused SUVs are subsequently removed by washing the chamber with PBS buffer 7 times. Then 14 μl of diluted reaction mixture is flowed into the biotinylated SLB-coated chamber and incubated in a humid container for 10 min. Free unattached streptavidin and enzyme complex are then removed by washing with PBS buffer for 7 times.

Tethering Alexa647-biotin-urease on streptavidin coated biotinylated SLBs

To decorate the biotinylated SLBs with streptavidin, 7 μl of 0.01mg/ml streptavidin was flowed in the biotinylated SLB-coated flow chamber and incubated for 5min to allow for the binding interaction between biotinylated lipid surface and streptavidin. Excess unbound streptavidins were subsequently removed by washing the chamber with 50 μl PBS buffer. Then 14 μl of 100 pM Alexa647-biotin-urease was flowed in the chamber and allowed for interaction with the streptavidin-coated lipid for 5 min. Finally, the free unbound Alexa647-biotin-urease was washed by 50 μl PBS buffer.

For all chambers, an oxygen scavenging system (10 mM dithiothreitol (DTT), 15 mg/ml glucose, 0.15 mg/ml catalase, and 0.05 mg/ml glucose oxidase) was flowed

prior to imaging to extend the lifetime of the fluorescent dyes and minimize photobleaching. All chambers are imaged using a custom-built TIRF microscope immediately after loading and kept measuring for a maximum of 30 minutes before discarding.

3.2.4 TIRF imaging

Single-particle imaging is performed using total internal reflection fluorescence (TIRF) microscopy with a custom-built laser system (100 mW 638 nm laser from Crysta-Laser) constructed around a Nikon Ti-E microscope. Imaging is performed with a 60×, 1.49 NA TIRF objective (Nikon), and then magnified an additional 2.5× before being projected onto an EM-CCD camera (IXON electron-multiplier CCD, Andor). The camera has 512 × 512 square pixels of 16.2 μm on each side, giving a final magnified pixel size of 107 nm/pixel. Movies were recorded at a rate of 17 frames/s ($\Delta t = 60$ ms/frame, ROI = 512×512 pixels) with a 30 ms exposure time using the Nikon Elements software. Laser power and EMCCD gain settings were kept constant for all movies.

3.2.5 Data analysis

The mean squared displacement (MSD) analysis is performed using the same protocol as described in Ref. [13]. A tracking plugin in ImageJ/FIJI, called ParticleTracker 2D/3D [44], is used to extract trajectories from microscopy videos. Homemade MATLAB codes based on Ref. [45] are applied for trajectory analysis. For each trajectory, we compute the time-averaged mean squared displacements (MSD) over different lag times by $\left\langle (\Delta r_i(t))^2 \right\rangle = \left\langle [\vec{r}_i(\tau + t) - \vec{r}_i(\tau)]^2 \right\rangle_\tau$, where $r_i(t)$ is the

position of the ith trajectory at lag time t, and the brackets $\langle \cdots \rangle$ indicate a time average over τ. We plot the MSDs as a function of lag time t, and derive the diffusion coefficient, D, from the slope of the MSD plot after fitting to the Einstein's diffusion equation in 2D:

$$\left\langle (\Delta r_i)^2 \right\rangle = 4Dt \tag{3.1}$$

Since the diffusion coefficients obtained from SPT measurements follow a log-normal distribution empirically [58–61], we first log-transform the diffusion coefficients extracted for each experimental group and bin it into a histogram. Each histogram is then fit with a Gaussian, for which the mean is taken as the apparent diffusion constant after transforming back to the normal D scale.

The parameters used in ParticleTracker 2D/3D plugin are: Particle size = 3-5 pixels; cutoff = 0.001; Percentile = 1%-5%; Link range = 4; Displacement = 4-7; Dynamics type = Brownian, for optimal tracking. Usually, thousands of trajectories can be detected for each experimental group by ParticleTracker 2D/3D, but not all are used for MSD analysis. Two thresholds are applied to select trajectories for analysis: 1) the minimum trajectory length, N, and 2) the goodness of the MSD-fit, R^2. In our analysis, only trajectories of at least 15 frames ($N \geq 15$) with the goodness of MSD-fit greater than 0.9 ($R^2 \geq 0.9$) contribute to the histogram of logarithmic diffusion coefficients for each case.

3.3 Enhanced diffusion of tethered urease

3.3.1 Enhanced diffusion of multi-streptavidin-urease complexes on SLBs

To confine the enzymes to 2D for accurate tracking, we tethered the urease to the SLB surfaces. Since the SLB is fluid, tethered urease could still diffuse freely in 2D. To tether the enzymes on SLB, we used the biotin-streptavidin interaction as the anchoring system. We first tried to conjugate the streptavidin(SA) directly on the biotinylated urease by incubating Alexa647-biotin-urease with streptavidin for hours. And then we tethered these SA-urease complexes on the biotinylated SLBs. However, during the hour-long incubation between SA and biotinylated urease, multi-SA-urease complexes could be formed, since each streptavidin has four biotin binding-sites and each urease(hexamer) could be modified by multiple biotin molecules. We measure the mobility of each tethered multi-SA-urease complexes on lipid surface with and without the presence of urea. Fig. 3.2A shows the distributions of log-transformed diffusion coefficient of the tethered multi-SA-urease complexes in the absence or presence of 200 mM urea. Each log$D$ histogram is fit by a Gaussian. The mean of each Gaussian fit is transformed back to normal diffusion units and used as the diffusion coefficient for each case (Fig. 3.2B). For the buffer case, we find $D_{\text{buffer}} = 0.0824\ \mu\text{m}^2/\text{s}$, and for the urea group we have $D_{\text{urea}} = 0.236\ \mu\text{m}^2/\text{s}$, an almost 3-fold enhancement in diffusion. This result is an important quantitative confirmation of our prior result demonstrating enhanced diffusion in Chapter 2. Compared with the lipid lateral diffusion constant in lipid bilayer ($D_{\text{lipid}} \sim$ 1-5 $\mu\text{m}^2/\text{s}$), the diffusion coefficient we measured for tethered multi-SA-urease complexes was much lower. We speculated that the diffusion constants we measured was actually for giant SA-urease-lipid aggregates, in which

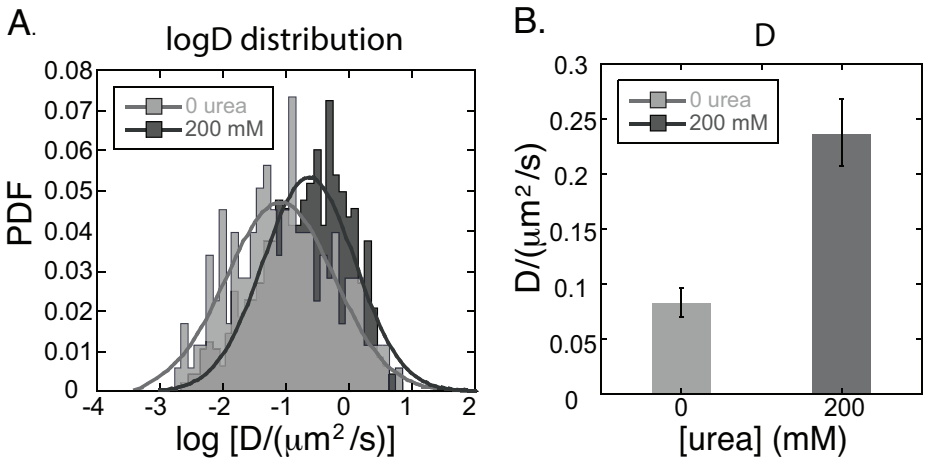

FIGURE 3.2: A) Histograms of logarithmic diffusion constant log$D$ of tethered urease with (dark gray, N = 484) and without (gray, N = 178) the presence of 200 mM urea. Line: the corresponding Gaussian fit to each log$D$ histogram. B) Apparent diffusion coefficients derived from the mean of the Gaussian fits for tethered urease with (dark gray) and without (gray) the presence of 200 mM urea. Error bars are determined from the standard errors of the mean of the Gaussian fits.

each streptavidin could bind with several adjacent biotinylated lipid molecules and form a raft-like diffusion patch in the lipid membrane.

3.3.2 Enhanced diffusion of streptavidin-urease complexes on SLBs

Another approach for tethering enzymes on SLBs was to first decorate the biotinylated lipid surface with streptavidin (SA) and then conjugate the biotinylated enzymes on the SA-decorated lipid bilayer. This method prevented the forming of multi-SA-urease complexes. Fig. 3.3 shows the representative trajectories of a multi-streptavidin-urease complex and a streptavidin-urease complex in buffer. The much dimer spot of the streptavidin-urease complex implied a fewer number of ureases conjugated in each complex, and confirmed the validity of this method as expected.

We then measured the diffusion rate of each tethered SA-urease complex with

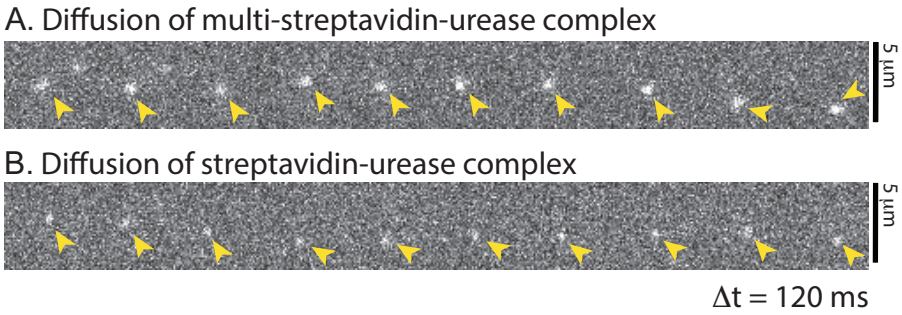

FIGURE 3.3: Representative trajectories of A) a multi-streptavidin-urease complex and B) a streptavidin-urease complex in buffer. The brighter spot in A) demonstrated that there might be multiple ureases conjugated together with one or more streptavidins in the complex, while the much dimer spot in B) implied a fewer number of urease conjugated, ideally should be one. (Time interval between frames: 120 ms; Scale bar: 5 nm.)

and without the presence of urea. Fig. 3.4A shows the distributions of log-transformed diffusion coefficient of tethered SA-urease in the absence or presence of 1 mM urea. Each log$D$ histogram was fit by a Gaussian. The mean of each Gaussian fit was transformed back to normal diffusion units and used as the diffusion coefficient for each case (Fig. 3.4B). For the buffer case, we found $D_{\text{buffer}} = 0.636\ \mu\text{m}^2/\text{s}$, and for the urea group we had $D_{\text{urea}} = 1.086\ \mu\text{m}^2/\text{s}$. An almost 1.7-fold enhancement in diffusion was observed. Compared with the diffusivity of the multi-SA-urease complexes in the former section, a faster diffusion was measured for the SA-urease probably due to its smaller size, while the relative enhancement in D was slightly attenuated. This lower enhancement might be due to the lower urea concentration used in this scenario. Further, there were less enzymes conjugated on each complex and thus might have less propulsive units to propel the enzyme-lipid rafts.

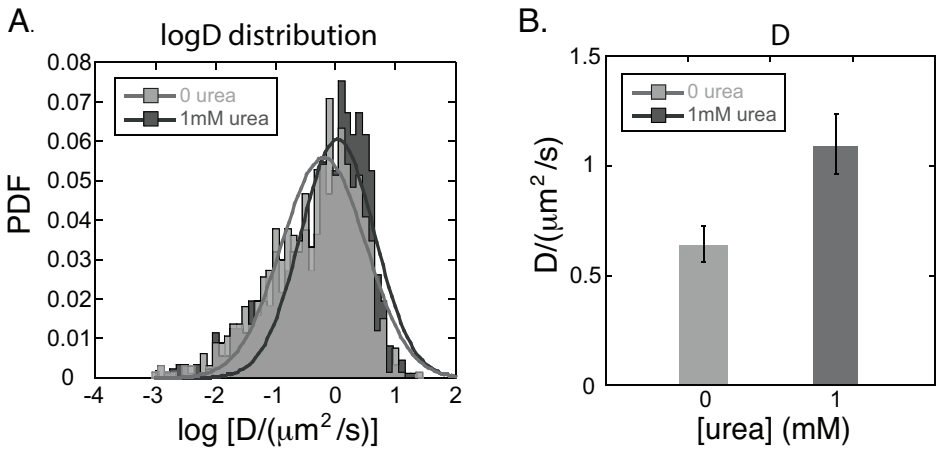

FIGURE 3.4: A) Histograms of logarithmic diffusion constant log$D$ of tethered urease with (dark gray, N = 877) and without (gray, N = 663) the presence of 1 mM urea. Line: the corresponding Gaussian fit to each log$D$ histogram. B) Apparent diffusion coefficients derived from the mean of the Gaussian fits for tethered urease with (dark gray) and without (gray) the presence of 1 mM urea. Error bars are determined from the standard errors of the mean of the Gaussian fits.

3.4 Conclusion

Using this tethered urease experimental design, we confirm the enhanced diffusion of urease at single enzyme scale. We show that the diffusion of each urease could be enhanced by 1.5-fold to 3-fold in the presence of urea, even when confined to two dimensions. This observation is also consistent with the findings that we reported in our prior work when F127 polymer brush chamber was used (Chapter 2).

Chapter 4

Enzyme diffusion in glycerol

4.1 Introduction

Another possible caveat of our prior work was the bulky polymers that we added in our chamber to facilitate single particle tracking. We used a surface polymer coating, Pluronic F-127, to prevent the unspecific binding of enzymes on the surface, and a large viscous polymer, methylcellulose (88KDa), to increase the viscosity and slow down the diffusion. However, both of these polymer additives could have potential, unknown effects on enzyme diffusion that were not easily quantifiable. To avoid adding polymers and to minimize the environmental complexity for enzyme diffusion, we replace the polymer brush coated surface with a SLB, and substitute the large viscous polymer, methylcellulose, with a smaller, well-characterized molecular viscosity agent, glycerol (Fig. 4.1). We test the reliability of this new experimental design by measuring the diffusion of particles with various sizes (R = 2.3, 4.8, 7.0, 99 nm) and in solutions of different viscosities (η = 2.73, 6.86, 12.76, 26.85, 41.30, 66.65, 113.85, 208.13 mPa·s). We find that the diffusion coefficients scale with particle size and solvent viscosity as expected from the Stokes-Einstein equation. We also compare two different data analysis approaches for SPT: the mean-squared displacement (MSD) analysis [45] and the jump-length analysis [62]. We

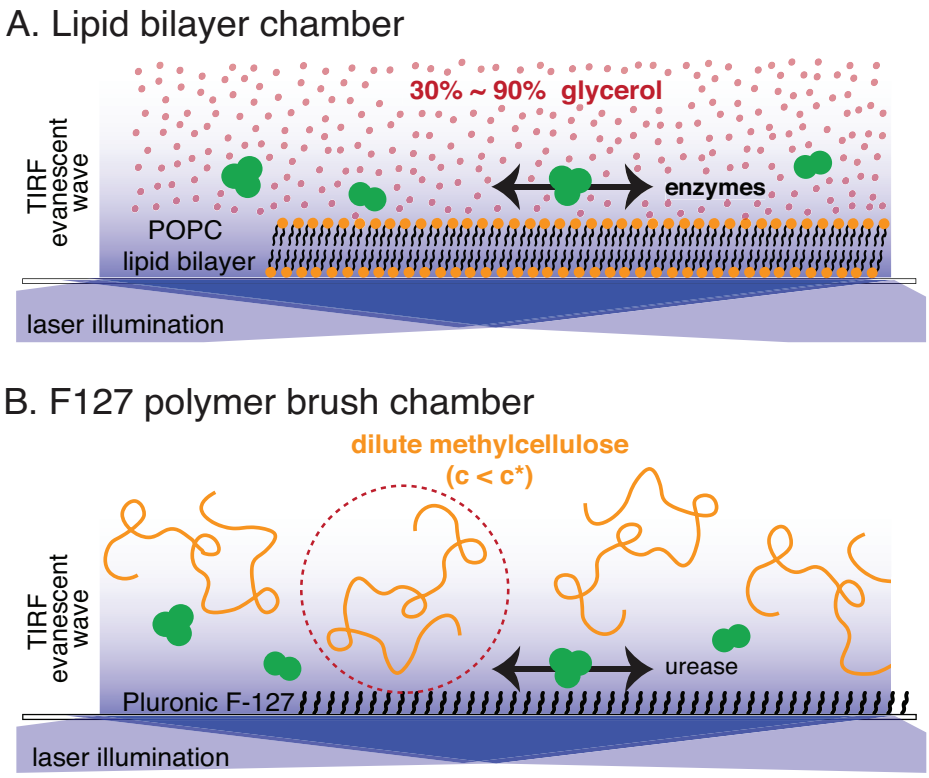

FIGURE 4.1: Schematics of experimental chamber designs. A) The SLB/glycerol chamber, where the surface is coated with SLB (orange and black) and a certain percentage of glycerol (red) is added as a viscous agent to slow down the mobility of enzymes. B) The F127 polymer brush chamber design used in our prior work (Chapter 2). Surface was coated by F127 block-copolymer (black); 3% dilute methylcellulose polymers (orange, $R_g \sim 30$ nm [43]) were used to slow down the mobility.

find that the MSD analysis requires high viscosity and large particle size to accurately report the diffusion coefficient, while the jump-length analysis depends less on the viscosity or size. Using this newly-designed SLB/glycerol chamber, we repeat the urease diffusion experiments in different concentrations of urea. However, this new chamber design fails to reproduce the enhanced diffusion of urease even in saturated urea concentration. We attribute this failure to the inhibited catalytic activity of urease due to the presence of glycerol.

4.2 Method

4.2.1 Enzyme preparation and activity assay

Experiments are prepared using commercially-available reagents. Urease from Jack Bean is purchased from TCI Chemicals. Aldolase from rabbit muscle is purchased from Sigma Aldrich. Green fluorescent protein (GFP) is purified following a standard protocol for His-tagged protein purification. Sub-micron multi-color plastic spheres (R = 99 nm) are purchased from Thermo Fisher. Enzymes are fluorescently labeled with Alexa Fluor 647 C_2 maleimide (Thermo Fisher) using a commercially available protein labeling kit following the optimized protocols provided by Thermo Fisher. The urease activity assay is performed following a published protocol in Ref.[42]. Briefly, we use phenol red as an color indicator which turns from yellow to red as pH increases, to estimate the urease activity. The assay mixture contains 10 nM urease, 28 μM phenol red, 2.5 mM urea, and 30% or 75% glycerol or 1$\times$ PBS buffer to contribute to a total volume of 1 ml. We measure the absorbance at 560 nm every 6 seconds to quantify the color-changing rate using UV-vis spectroscopy.

4.2.2 Glycerol/SLBs chamber setup

The supported lipid bilayers are made by fusing small unilamellar vesicles (SUVs) on the chamber surface [57]. SUVs are made of POPC (1-palmitoyl-2-oleoyl-glycero-3-phosphocholine) purchased from Avanti. First, 40 μl of 10 mg/ml POPC in chloroform is dissolved in 70 μl of chloroform and mixed well. Chloroform is then evaporated from the mixture under a gentle stream of N_2 gas for 10 min. The lipid mixture is further dried out in a vacuum desiccator for 30 min. The dried lipid is rehydrated in 100 μl PBS buffer and vortexed for 1 min to form giant unilamellar

vesicles (GUVs). The white opaque GUV suspension is then sonicated using a sonicator microtip probe (Sonifier) for 3 min to form a clear SUV solution. This clear SUV solution is stored at 4°C and used for the SLB surface coating.

To make SLB-coated flow chambers, 10 μl of SUV solution is first flowed in and incubated for 20 min to allow for the fusion of SUVs to the surface. Excess unfused SUVs are subsequently removed by washing the chamber with PBS buffer 7 times. The SLB-coated chambers are kept in a humid container to prevent dehydration and taken out immediately before use.

The final imaging chamber has $\sim$ 100 pM enzymes or proteins (diluted in PBS), a certain percentage of glycerol, an oxygen scavenging system (10 mM dithiothreitol (DTT), 15 mg/ml glucose, 0.15 mg/ml catalase, and 0.05 mg/ml glucose oxidase) to extend the lifetime of the fluorescent dyes and minimize photobleaching and also enzyme substrate at the desired concentration (Fig. 4.1B). All chambers are imaged using a custom-built TIRF microscope immediately after loading and kept measuring for a maximum of 30 minutes before discarding.

4.2.3 TIRF imaging

Single-particle imaging is performed using total internal reflection fluorescence (TIRF) microscopy with a custom-built laser system (50 mM 488 nm laser and 100 mW 638 nm laser from CrystaLaser) constructed around a Nikon Ti-E microscope. Imaging is performed with a 60×, 1.49 NA TIRF objective (Nikon), and then magnified an additional 2.5× before being projected onto an EM-CCD camera (IXON electron-multiplier CCD, Andor). The camera has 512 × 512 square pixels of 16.2 μm on each side, giving a final magnified pixel size of 107 nm/pixel. Movies were recorded at a rate of 17 frames/s (Δt = 60 ms/frame, ROI = 512×512 pixels) or 105 frames/s (Δt = 9.5 ms/frame, ROI = 512×76 pixels) with a 30 ms or 4 ms exposure using

the Nikon Elements software. Laser power and EMCCD gain settings were kept constant for all movies.

4.2.4 Data analysis

MSD analysis

The mean squared displacement (MSD) analysis is performed using the same protocol as described in Ref. [13]. A popular tracking plugin in ImageJ/FIJI, called ParticleTracker 2D/3D [44], is used to extract trajectories from microscopy videos. Homemade MATLAB codes based on Ref. [45] are applied for trajectory analysis. For each trajectory, we compute the time-averaged mean squared displacements (MSD) over different lag times by $\left\langle (\Delta r_i(t))^2 \right\rangle = \left\langle [\vec{r}_i(\tau + t) - \vec{r}_i(\tau)]^2 \right\rangle_\tau$, where $r_i(t)$ is the position of the ith trajectory at lag time t, and the brackets $\left\langle \cdots \right\rangle$ indicate a time average over τ. We plot the MSDs as a function of lag time t, and derive the diffusion coefficient, D, from the slope of the MSD plot after fitting to the Einstein's diffusion equation in 2D:

$$\left\langle (\Delta r_i)^2 \right\rangle = 4Dt \tag{4.1}$$

Since the diffusion coefficients obtained from SPT measurements follow a log-normal distribution empirically [58–61], we first log-transform the diffusion coefficients extracted for each experimental group and bin it into a histogram. Each histogram is then fit with a Gaussian, for which the mean is taken as the apparent diffusion constant after transforming back to the normal D scale.

The parameters used in ParticleTracker 2D/3D plugin are: Particle size = 3-5 pixels; cutoff = 0.001; Percentile = 1%-5%; Link range = 4; Displacement = 4-7; Dynamics type = Brownian, for optimal tracking. Usually, thousands of trajectories can be detected for each experimental group by ParticleTracker 2D/3D, but not all

are used for MSD analysis. Two thresholds are applied to select trajectories for analysis: 1) the minimum trajectory length, N, and 2) the goodness of the MSD-fit, R^2. In our analysis, only trajectories of at least 10 frames ($N \geq 10$) with the goodness of MSD-fit greater than 0.9 ($R^2 \geq 0.9$) contribute to the histogram of logarithmic diffusion coefficients for each case.

Jump-length analysis

Trajectories are also analyzed by the "jump-length" method, which uses the statistics of jump-lengths (the displacements of particles over different lag times) to deduce the corresponding diffusion properties [62]. Briefly, for a particle starting at the origin and freely diffusing in 2D, the probability of finding it at position r after a lag time Δt can be described by:

$$P(r, \Delta t) = \frac{r}{2D\Delta t} \exp\left[\frac{-r^2}{4D\Delta t}\right] \tag{4.2}$$

where D is the diffusion coefficient. Thus, by fitting the jump-length distributions of particles for different lag times to the above probability function, the diffusion coefficient can be assessed. We use a semi-analytical kinetic model-based jump length analysis called Spot-On to perform the jump-length analysis. This model was developed by Hansen et al in Ref.[62]. In their model, several factors are taken into account to distinguish different diffusion ensembles from the population and to compensate the biases from fast-moving particles, such as 'motion-blur' (Fig. 4.2). In this approach, all trajectories detected by the tracking algorithm are treated equally and contribute to the jump length histogram with no thresholds applied. This model-based jump-length analysis approach was first adopted in single enzyme diffusion experiments by Chen et al. in Ref.[21]. In their work, single enzymes

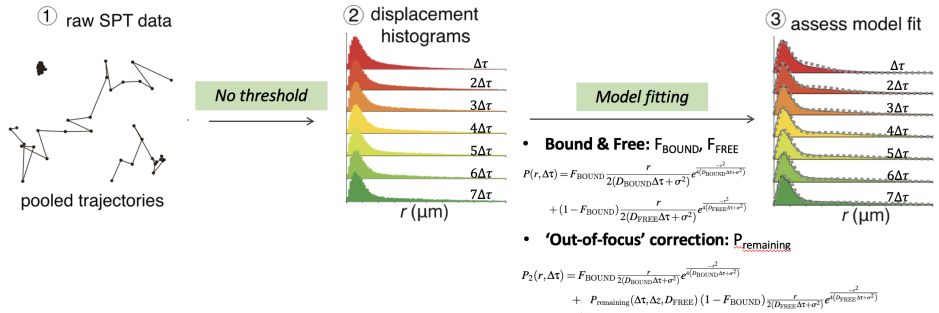

FIGURE 4.2: An overview of how Spot-On works. Figures adapted from ref [62].

were localized and tracked using a custom-written MATLAB implementation of the multiple-target tracing algorithm (MTT algorithm) [63]. To be consistent, we exploit the same MTT algorithm for particle tracking in the following jump-length analysis.

We use the following settings for the MTT algorithm: LocalizationError = -6.25; EmissionWavelength = 647; ExposureTime = 60 or 9.5 ms; NumDeflationLoops = 0; MaxExpectedD ($D_{\max}$) = 1.4-70 $\mu m^2/s$; NumGapsAllowed = 3 or 2 (see Supplemental Information for more details about the parameter settings in MTT). For Spot-On analysis we use: TimeGap = 60 or 9.5 ms; GapsAllowed = 2 or 1; dZ = 0.700; TimePoints = 2; UseEntireTraj = yes; D_Free_2State = [0.01, $D_{\max}$ used in MTT]; D_Bound_2State = [0.0001, 0.001]; ModelFit = CDF.

During the analysis, we find that the diffusion coefficient reported by Spot-On analysis depends linearly on the $D_{\max}$ that we set in the MTT algorithm. To determine the optimized $D_{\max}$ for each case, we repeat the analysis over different $D_{\max}$ values and find the corresponding D from Spot-On. We plot the D as a function of $D_{\max}$, and expect three regimes: 1) a linear regime in which D increase as $D_{\max}$ increases; 2) a plateau when D no longer depends on $D_{\max}$; 3) another linear regime when D is proportional to $D_{\max}$ again. We use the $D_{\max}$ value at the plateau as the most optimized value for each case.

4.3 Reliability of glycerol/SLBs chamber setup

Freely diffusing nanoscale particles usually undergo Brownian motion. Their diffusion coefficients are described by the Stokes-Einstein equation: $D = \frac{k_B T}{6\pi\eta R}$. Normally, the diffusion constant D scales inversely with solvent viscosity η and particle size R. To test the efficacy of the SLB/glycerol chamber setup, we measure the diffusivity of different particles in solutions of different viscosities in this new experimental design. We also compare two data analysis approaches, MSD analysis and the jump-length analysis, under the same scenario.

4.3.1 Diffusion of a constant-size particle at different viscosities

We first fix the particle size and measure how the diffusion coefficient changes with viscosity. We examine the diffusion of a single type of enzyme, aldolase (R = 4.8 nm [64]), for different viscosities. Solvent viscosity is tuned by varying the percent volume of glycerol in the buffer solution. We applied two different data analysis approaches, MSD analysis and the jump-length analysis, to analyze the same set of enzyme diffusion videos. Analysis results from each method are then compared side-by-side.

We first performed the MSD analysis following the same protocols as described in our prior work [13]. The distributions and Gaussian fits of log-transformed diffusion coefficients of aldolase under different glycerol percentages are shown in Fig. 4.3A. The mean log$D$ of each distribution, after transforming back to the typical diffusion units, is used as the apparent diffusion coefficient D_{MSD} for each case (triangle, Fig. 4.3C). We also applied the jump-length analysis (Spot-On) on the same data set. We find the distributions of aldolase jump lengths for each glycerol percentage (Fig. 4.3B), and derive the diffusion coefficient $D_{\text{jump-length}}$ from the kinetic

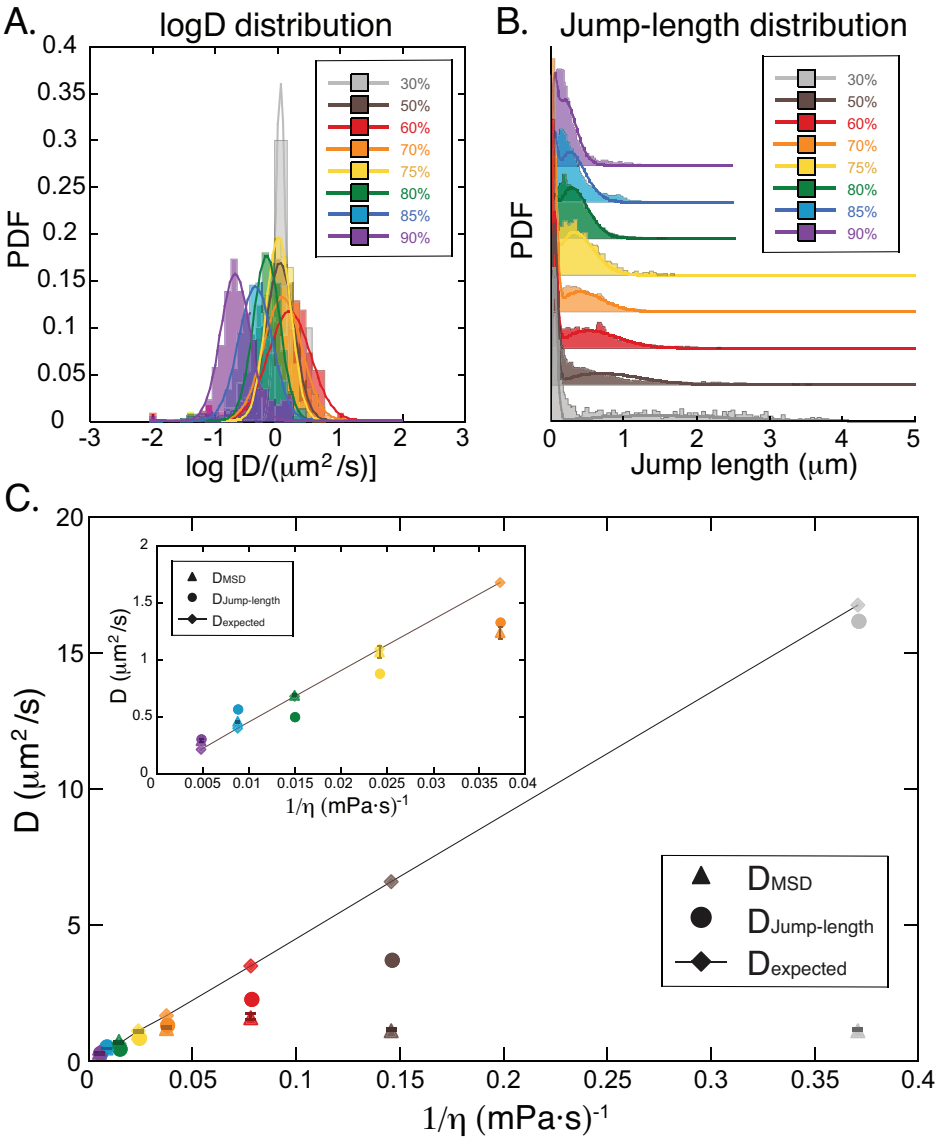

FIGURE 4.3: A) Histograms of logarithm of diffusion coefficients for aldolase under different glycerol percentages: 30% (gray region, N = 10), 50% glycerol (brown region, N = 420), 60% (red region, N = 109), 70% (orange region, N = 313), 75% (yellow region, N = 97), 80% (green region, N = 676), 85% (blue region, N = 736), 90% (purple region, N = 213). Colored lines show the corresponding Gaussian fits to the log$D$ histograms. B) Distributions of jump-length for aldolase over one lag time $\Delta t = 60$ ms at different glycerol percentages. Colored lines are the corresponding kinetic model fits from Spot-On analysis. C) Comparisons of D_{MSD} (triangle), $D_{\text{jump-length}}$ (circle) and D_{expected} (diamond) of aldolase at different viscosities. Inset: enlarged version of the high viscosity regime with glycerol% $\geq$ 70%. Guide line shows the linear relationship between D and $1/\eta$ suggested by the Stokes-Einstein equation $D = k_B T/6\pi\eta R$. Error bars are determined from the standard errors of the mean of the Gaussian fits.

model fitting following the procedures as described in Ref. [21] and Methods (circle, Fig. 4.3C). We compare the diffusion coefficients derived from MSD analysis, D_{MSD}, jump-length analysis, $D_{\text{jump-length}}$, and their expected value determined by the Stokes-Einstein equation, D_{expected}, in Fig. 4.3C. In order to highlight the linear dependence of diffusion on the inverse of the viscosity, D_{MSD}, $D_{\text{jump-length}}$ and D_{expected} are plotted as a function of the inverse of the viscosity $1/\eta$.

We find that, at high viscosity ($1/\eta < 0.025$ (mPa·s)$^{-1}$, or glycerol% $> 70\%$), both analysis methods report D similar to D_{expected} (Fig. 4.3C, inset). D_{MSD} seems to match with the expected value better than $D_{\text{jump-length}}$ at high viscosities (see supplemental information for more detailed data). However, at low viscosity ($1/\eta > 0.08$ (mPa·s)$^{-1}$, or glycerol% $< 60\%$), D_{MSD} shows to be lower than to the expected value, deviating from the linear dependence on $1/\eta$ and appearing to plateau as viscosity decreases (Fig. 4.3C, triangle). We attribute this underestimation of the diffusion constant to the under-counting of fast-diffusing particles when using MSD analysis. Specifically, at low viscosity, particles move faster and exit the focal plane quickly, making it hard to track and acquire long trajectories. Only slowly moving particles, like large protein aggregates, remain in focus for long enough to be captured. Since our MSD analysis only analyzes trajectories of at least N frames (usually, $N = 10$ in our experiments), the short trajectories from fast-diffusing molecules are completely filtered out during the analysis process. As a result, slow-diffusing tracks account for the vast majority of trajectories analyzed, leading to an underestimation of the overall diffusion coefficient reported. From the data, we suggest that a minimum viscosity, $\eta_c = 26.8$ mPa·s (or glycerol% $= 70\%$), is required for MSD analysis to yield valid diffusion coefficients. While MSD analysis fails at low viscosities, we find that the jump-length analysis results are still close to D_{expected} (Fig. 4.3C, circle). Thus, jump-length analysis seems more appropriate for the low

viscosity regimes than the MSD analysis.

We notice that the diffusion coefficients given by jump-length analysis seem to depend heavily on one of the parameters set in the tracking algorithm, called $D_{\max}$. This parameter defines an area that a particle is assumed to explore during one lag time. This area is then used to search for the same particles between frames to connect and form trajectories. When using larger $D_{\max}$ values, the possibility to mistakenly link two different particles into the same trajectory is increased, which in turn could lead to the report of a higher diffusion coefficient than expected. Therefore, care must be taken when choosing parameters for jump-length analysis.

4.3.2 Diffusion of different-size particles at fixed viscosity

We next examine how well the SLB/glycerol chamber could work for measuring the diffusion of different-size particles at a fixed viscosity ($\eta = 41.3$ mPa·s, or glycerol% = 75%). Similarly as before, we adopt two approaches, the MSD analysis and the jump-length analysis, to analyze the diffusion videos. We quantify the diffusion of four species of particles: GFP ($R = 2.3$ nm [65]), aldolase ($R = 4.8$ nm [64]), urease ($R = 7.0$ nm [66]), and sub-micron multi-color plastic spheres ($R = 99$ nm). From MSD analysis, we plot histograms of logarithmic diffusion coefficient for the four different particles (Fig. 4.4A). The apparent diffusion coefficient for each particle species is determined by the mean of each Gaussian fit after transforming log$D$ back to the normal D scale as described before (triangle, Fig. 4.4C). For jump-length analysis, the distributions of jump-length over one lag time are shown for each particle species (Fig. 4.4B). The corresponding diffusion coefficients are derived from the kinetic model fitting in Spot-On and depicted as circles in Fig. 4.4C. Again, we plot D as a function of the inverse radius $1/R$ to demonstrate the inversely proportional relationship between diffusion rate D and particle size R more

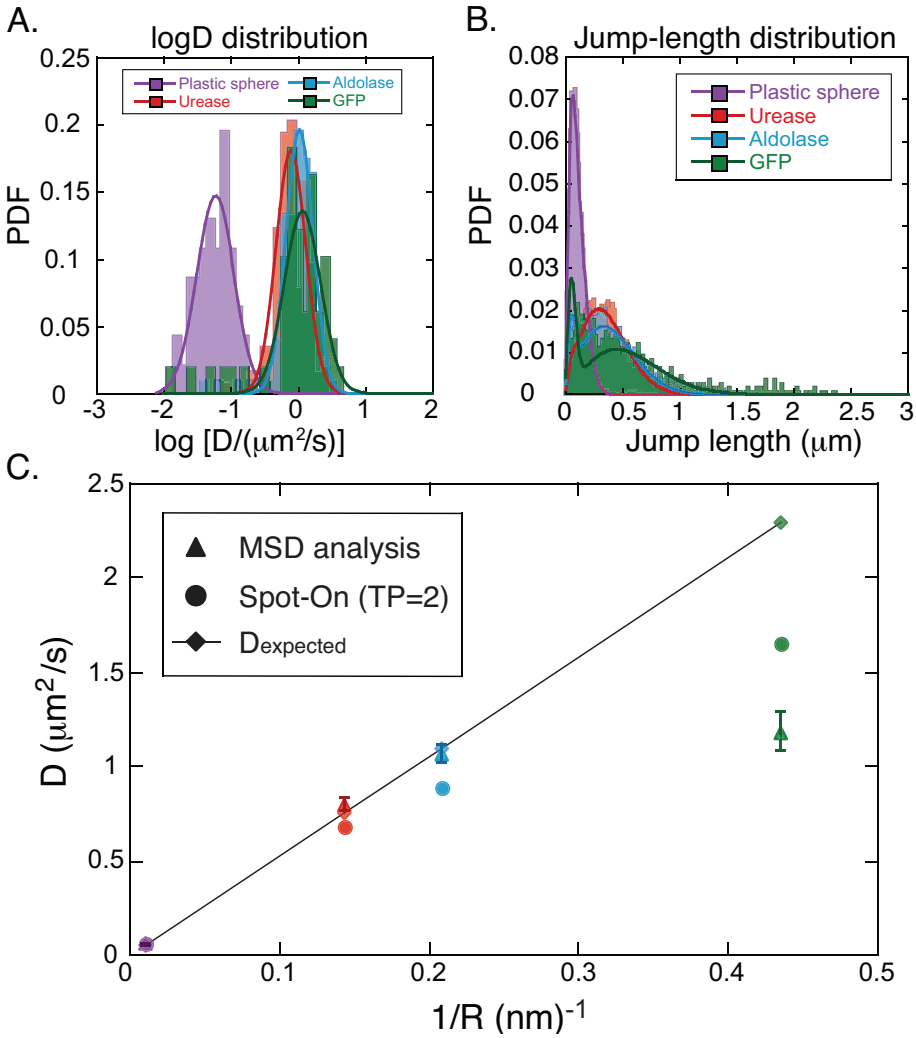

FIGURE 4.4: A) Histograms of log-transformed diffusion coefficients for different-size particles in 75% glycerol: plastic spheres (purple region, $N = 46$), urease (red region, $N = 113$), aldolase (blue region, $N = 97$), GFP (green region, $N = 49$). Colored lines show the corresponding Gaussian fits to log$D$ histograms. B) Distributions of jump-length at one lag time $\Delta t = 60$ ms for different-size particles in 75% glycerol. Colored lines are the corresponding kinetic model fits from Spot-On analysis for the jump-length distributions. C) Comparisons of D_{MSD} (triangle), $D_{\text{jump-length}}$ (circle) and D_{expected} (diamond) for different-size particles in 75% glycerol. Guide line represents the inverse proportional relationship between D and R suggested by the Stokes-Einstein equation $D = k_B T / 6\pi\eta R$. Error bars are determined from the standard errors of the mean of the Gaussian fits.

clearly.

We find that for relatively large particles, including the plastic sphere, urease, and aldolase, both MSD analysis and jump-length analysis report diffusion coefficients that match with the expected values (Fig. 4.4C). For smaller particles, such as GFP, MSD analysis again underestimates the expected diffusion coefficients. This underestimation of diffusion coefficients of smaller particles is likely due to the same issue described previously for low viscosity. Since smaller particles diffuse faster, most of the short trajectories from small fast-moving particles would be filtered out, leading to an under-counting of the fast population, which in turn results in the slower diffusion reported. As above, this suggests that a minimum size threshold, R_c, should be set for MSD analysis when using SLB/glycerol chambers to get reasonable diffusion measurements. Jump-length analysis seems to report a diffusion coefficient closer to the expected value, implying an advantage in analyzing fast-diffusing particles.

In conclusion, in an attempt to perform better SPT experiments, we replace the bulky polymers with well-characterized molecular components: lipids on the surface and glycerol in solution. We examine the the reliability of this new SLB/glycerol chamber by measuring the diffusion of different-size particles in different viscosity solutions. We find that the particle diffusion in SLB/glycerol chamber behaves as the Stokes-Einstein equation suggests. The measured diffusion constants scale inversely with solvent viscosity η and particle size r, which confirms the efficacy of SLB/glycerol chamber for SPT experiments. We also compare two data analysis methods: the MSD analysis and the jump-length analysis, using the SLB/glycerol chamber. We find that the MSD analysis is reliable at high viscosity and large particle size, which is the physical situation needed for relatively slow diffusion. Jump-length analysis seems to have less limitations on solvent viscosity and particle size,

and has the advantage that it can analyze fast-moving particles. However, the diffusion coefficients reported from jump-length analysis depend strongly on the tracking parameters settings, specifically, $D_{\max}$. Thus, care must be taken when choosing parameters for this approach. Also, all key parameters used for the data analysis should be reported to ensure the reproducibility of the results, as suggested in Ref. [62].

4.4 Urease diffusion in glycerol/SLBs chamber

We next seek to reproduce the enhanced diffusion of active urease with the presence of urea using the newly-designed SLB/glycerol chamber. We find in the former section that MSD analysis performs better at high viscosity regimes, while jump-length analysis is more preferable at low viscosity environments. Thus, we make two sets of diffusion measurements on urease in two viscosity regimes: 1) the high viscosity regime using 75% glycerol analyzed by MSD analysis and 2) the low viscosity regime using 30% or no glycerol analyzed by jump-length analysis.

4.4.1 Urease diffusion in the High Viscosity Regime

We first measure the diffusion of urease at seven different urea concentrations using the SLB/glycerol chamber with 75% glycerol ($\eta = 41.3$ mPa·s). We choose 75% because it is the lowest glycerol percentage for MSD analysis that yields accurate diffusion coefficients. Histograms of log-transformed diffusion coefficients of urease are illustrated in Fig. 4.5B for four representative urea concentrations and are compared with our prior results when using F127 polymer brush chambers (Fig. 4.5A from Ref.[13]). In the prior chamber design, urease appeared to diffuse faster with the presence of only 10 μM urea in solution. However, with the newly-designed

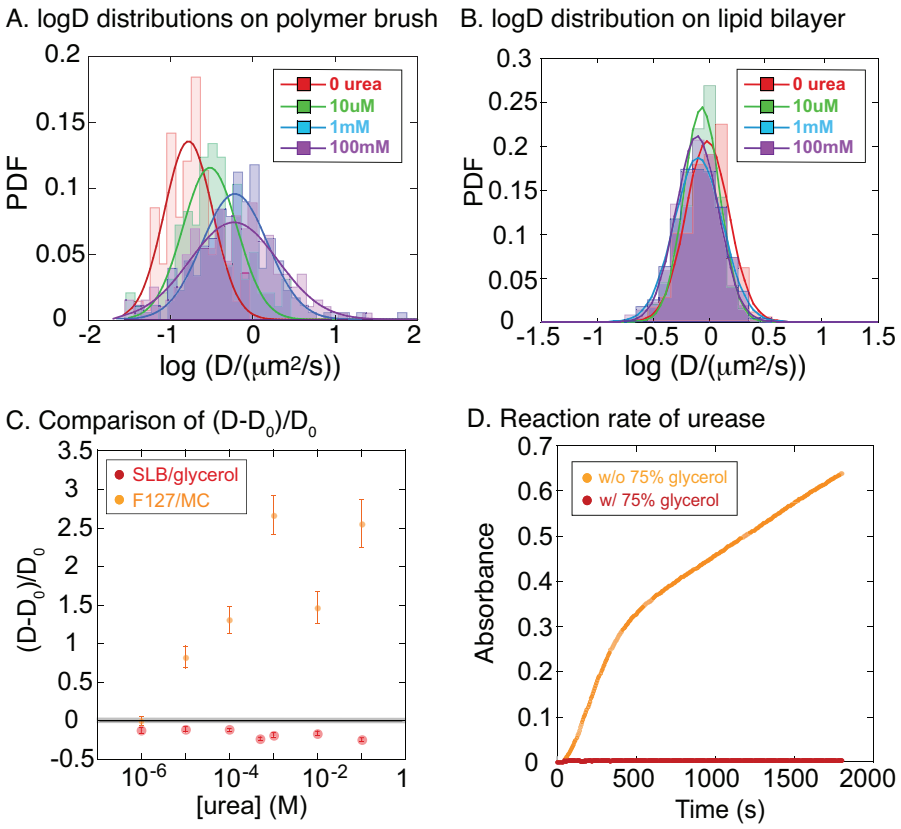

FIGURE 4.5: A) Representative probability distribution of log-transformed diffusion constants log$D$ at four different urea concentrations: 0 (red region, N = 141), 10 μM (green region, N = 97), 1 mM (blue region, N = 178), 100 mM (purple region, N = 203), when using polymer brush chamber design. Colored lines show the Gaussian fits to the corresponding histograms. B) Representative histograms of logarithmic diffusion coefficients at different urea concentrations: 0 (red region, N = 178), 10 μM (green region, N = 205), 1 mM (blue region, N = 390), 100 mM (purple region, N = 357) when using SLB/glycerol chamber. Colored lines show the Gaussian fits to the corresponding log$D$ histograms. C) The relative increase in D, $(D - D_0)/D_0$, as a function of urea concentration observed in the prior polymer brush chamber (orange dots) and the SLB/glycerol chamber (red dots), where D_0 is the diffusion constant when no urea is present. Error bars are determined from the standard errors of the mean of the Gaussian fits. D) Comparisons of urease-catalyzed reaction rate with (red) and without (orange) the presence of 75% glycerol.

SLB/glycerol chamber, we do not find any enhancement in urease diffusion even at the saturation concentration of urea (100 mM). To illustrate the relative increase in diffusion coefficient of urease more clearly, we plot the relative changes in D, $(D - D_0)/D_0$, as a function of urea concentration (Fig. 4.5C), where D_0 is the diffusion rate when no urea is present. In contrast to the ~3-fold increase previously observed in the polymer brush chamber (Fig. 4.5C, orange dots), no relative increase is observed for urease diffusing in the SLB/glycerol chamber at any urea concentrations (Fig. 4.5C, red dots).

Given our ability to reproduce the enhanced diffusion of urease in the presence of urea by using the polymer brush chamber (Chapter 2) and by tethering urease on SLB (Chapter 3), we were surprised by the lack of enhancement in the SLB/glycerol chamber. The main difference among these experiments is the high percentage (75%) of glycerol used in the SLB/glycerol chamber. We speculate that such high amounts of glycerol might interfere with the urease activity, resulting in the failure to observe the enhanced diffusion. In order to determine if 75% glycerol poisons the enzyme activity, we measure the activity of urease with and without the presence of 75% glycerol using a colormetric assay. We find that the urease activity is completely inhibited by the presence of 75% glycerol (Fig. 4.5D). Thus, with no catalytic activity, no matter how much substrate is present in the solution, the enzyme diffuses as it does in buffer, and no enhanced diffusion is observed. Interestingly, this result is the opposite of what was previously reported for urease activity in high glycerol in an original paper published in 1967 [67]. We believe that the modern techniques we employ here are better for addressing these questions than the technique used over 50 years ago. Therefore, when choosing viscous agents for enzyme diffusion experiments, extra care must be taken to make sure the enzyme activity is preserved.

4.4.2 Diffusion of Active Urease at Low Viscosity Regime

We next quantify the diffusion of active urease at low viscosities using the jump-length analysis. Based on what we have found in the former section, 30% glycerol ($\eta = 2.7$ mPa·s) appears to be an appropriate viscosity range for jump-length analysis to work. We first measure the urease diffusion in the absence and presence of 200 mM urea at 30% glycerol. Fig. 4.6A (top) shows the jump-length distributions of urease with and without the presence of urea in our 30% glycerol chamber. No obvious shift is observed for the urease jump-length when urea is present. After kinetic model fitting from Spot-On, we derive the diffusion coefficient for each case and plot the results in Fig. 4.6B (left). We find that for the buffer case (no urea) $D_{\text{buffer, 30\% gly}}$=9.65 μm^2/s, while for the urea case $D_{\text{urea, 30\% gly}}$=10.04 μm^2/s. Consistent with what has been implied by the jump-length distributions in Fig. 4.6A (top), almost no relative increase (only ∼4%) in D is found for urease.

To examine the reason for the lack of enhancement, we perform the same colorimetric assay for urease to check its activity in 30% glycerol. We find that although urease still remains active under 30% glycerol, its catalytic activity is moderately suppressed (Fig. 4.6C). The enzymatic catalysis rate is not as fast as before. This implies that even a slight amount of change on enzyme activity might result in the failure to observe the enhanced enzyme diffusion.

To avoid adding glycerol, we make the same diffusion measurements for urease in buffer solution (no glycerol, $\eta = 1$ mPa·s). Fig. 4.6A (bottom) and Fig. 4.6B (right) show the jump-length distributions and the apparent diffusion coefficients reported by Spot-On analysis, respectively. With no glycerol present, a slight increase ∼17% in D is observed for urease diffusing in urea solution ($D_{\text{buffer, no gly}}$=20.65 μm^2/s,

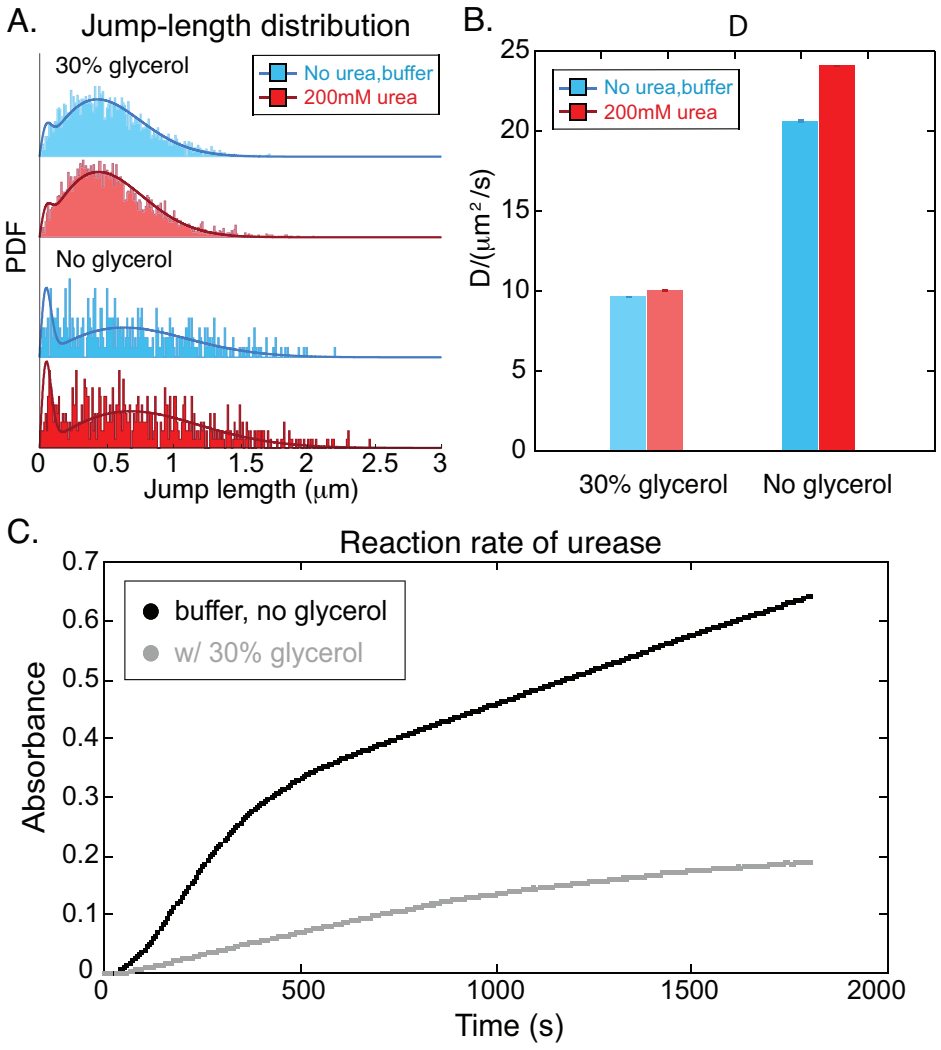

FIGURE 4.6: A) Jump-length distributions of urease at $\Delta t = 9.5$ ms with (red) and without (blue) the presence of 200 mM urea in 30% glycerol (top) and in buffer solution (bottom). Colored line shows the corresponding kinetic model fit from Spot-On analysis for each jump-length distribution. B) Apparent diffusion coefficients reported by Spot-On analysis for urease diffusing in 30% glycerol (left) and in buffer solution (right) with (red) and without (blue) the presence of 200 mM urea. C) Comparisons of urease-catalyzed reaction rate with (gray) and without (black) the presence of 30% glycerol.

$D_{\text{urea, no gly}}$=24.09 $\mu m^2/s$). This 17% increase is much lower than the 3-fold enhancement that we have observed in our prior polymer brush design (Chapter 2) or the tethered urease experiments (Chapter 3). Interestingly, this slight enhancement is similar to the increase reported in the prior studies of enhanced urease diffusion using FCS measurements [6, 11, 20].

We surmise that this underestimation of relative increase in D is likely due to the inaccurate tracking of very fast-moving particles, which is limited by the spatial and temporal scales set in our TIRF microscope. Several facts imply that this may be the case: 1) the apparent diffusion coefficients derived from the jump-length analysis are much lower than the expected value estimated from the Stokes-Einstein equation (D_{expected}=31.38 $\mu m^2/s$); 2) the noisiness of the jump-length distributions in the absence of glycerol (Fig. 4.6A (bottom)) indicates that fewer trajectories are analyzed compared to the 30% glycerol scenario (Fig. 4.6A (top)). Few data points could result in inappropriate model fitting and an inaccurate D. Therefore, at extremely low viscosities, even jump-length analysis may not be applicable. In the first Spot-On analysis paper, the authors only tested D within the range of $0.5 \sim 14.5$ $\mu m^2/s$ [62], implying that this method might not be able to capture faster-diffusing particles. Despite that, follow-up papers have used the Spot-On analysis to measure diffusion rates as fast as ~ 50 $\mu m^2/s$, giving us confidence to try this method on our cases [21].

4.5 Conclusion

To minimize the chamber complexity, we design a new chamber with a SLB coated surface and a small viscous molecule, glycerol, to replace the bulky polymers used

in the prior F127 polymer brush design. We confirm the efficacy of the newly-designed SLB/glycerol chamber by measuring the diffusion of different-size particles in different viscosity solutions. We find that particles diffuse as the Stokes-Einstein equation predicts: their diffusion coefficients scale inversely with solvent viscosity η and particle size R.

We also compare two data analysis methods for SPT: the MSD analysis and the jump-length analysis. We find that MSD analysis is appropriate for analyzing slowly diffusing species, when high solvent viscosity or large particle size are preferable. While analyzing fast diffusion, MSD analysis under-counts the population of fast-moving particles, leading to an underestimation of the actual diffusion coefficient. Jump-length analysis seems to be applicable for a wider range, from very slow diffusion to relatively fast motion. However, we also notice that for jump-length analysis the diffusion coefficients reported depend heavily on the parameters, especially one of the input parameters in MTT tracking algorithm, $D_{\max}$. Thus, care must be taken when choosing parameters and a dataset of all key parameters used for the analysis should be reported specifically to allow for reproducibility and transparency when using this method.

We next examine how urease diffuses in the SLB/glycerol chamber with and without the presence of urea. We measure the diffusion of urease at two viscosity regimes: the high viscosity regime with 75% glycerol and the low viscosity regime with 30% glycerol. However, no enhanced diffusion is observed for urease at either viscosity due to the inactivation of urease by glycerol. To avoid adding glycerol, we make the same urease diffusion measurements in buffer solution (no glycerol), yet we find that our analysis methods are unable to achieve accurate tracking and adequate data analysis at such low viscosity. Our results imply that a moderate

slowing down of diffusion is needed for accurate SPT of enhanced enzyme diffusion, but care must be taken when choosing viscosity agents to preserve enzyme activity.

Taken together, we find that the previously employed F127 polymer brush chamber in Chapter 2 seem to be excellent at slowing down enzyme motility without inhibiting its activity. The tethered enzyme experimental design demonstrated in Chapter 3 is also a viable strategy. Overall, an optimized experimental design, as well as a more intuitive, less parameter-dependent data analysis approach, are still needed for future investigations of enhanced enzyme diffusion.

Chapter 5

Single-molecule imaging of enzyme-conjugated DNA origami

5.1 Introduction

Active matter is comprised of a large number of energy-using components, which can exhibit remarkable non-equilibrium activities as found in living materials. Enzymes are such an energy-consuming, nanoscale active matter. Recent exciting findings about enzymes show that, when performing chemical reactions, these nanoscale active constituents can propel themselves and display an enhanced diffusion as described in the former chapters (Chapter 2, 3, 4). Using enzymes as propulsive units and coupling onto the surface of other objects, like plastic spheres or silica tubes [4, 5], people have constructed self-propelled active particles at the micrometer-scale. Here, we will create a new suite of programmable active particles ranging from nanometres to micrometres using DNA origami and enzymes. DNA origami technology has been used to build well-defined nanostructures ranging from tens of nanometres to sub-micrometres from bottom-up fabrication [23, 29–32]. Basically, a long, circular strand of DNA (scaffold) is annealed with ~ 200 single-stranded DNA oligomers (staples) and folded into a prescribed three-dimensional shape via base

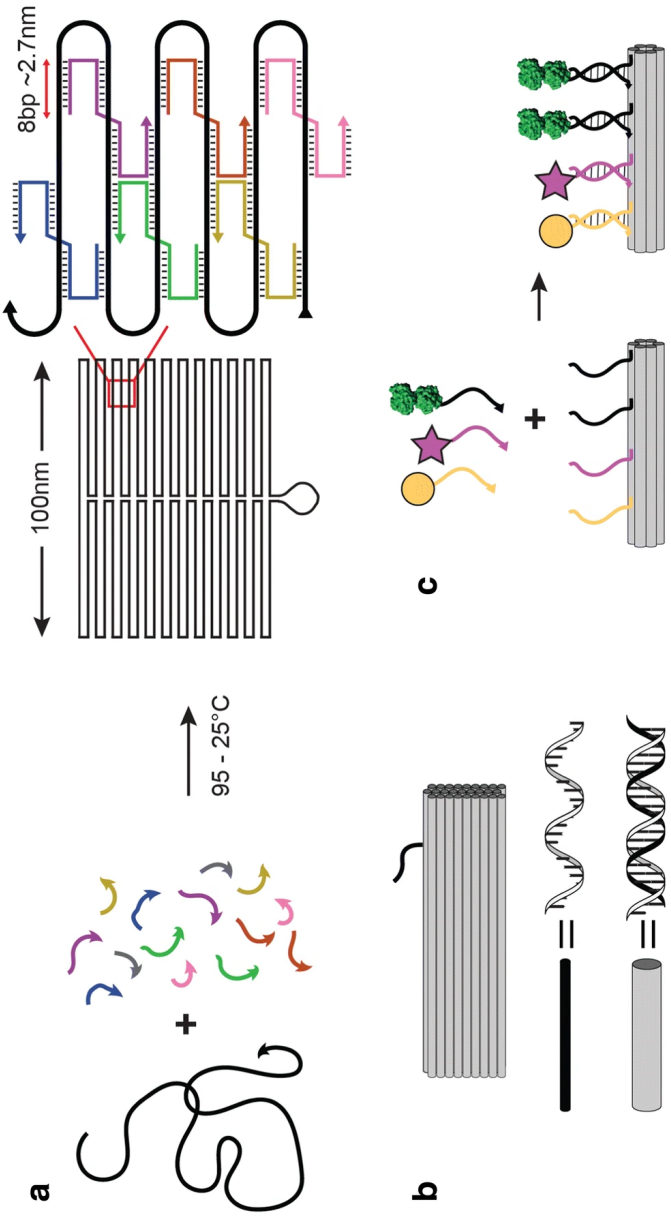

FIGURE 5.1: A) Basic concept of DNA origami: a long single-stranded DNA scaffold (black, usually a circular strand of DNA) is folded up into a double-stranded DNA shape, which is cross-linked by $\sim$ 200 short 'staple' oligonucleotide strands (coloured). B) DNA-origami nanostructures are often depicted by representing each DNA duplex with a rigid cylinder of width 2.6 nm (grey) and single-stranded DNA regions with a flexible line (black). C) DNA-origami nanostructures can be functionalized by adding single-stranded DNA 'handles' ('sticky end') to the end of staple strands on the surface of the structure (coloured). Each staple sequence is unique, so handle locations are uniquely addressable. Guest molecules, such as metallic nanoparticles (yellow), fluorophores (pink) or proteins (green), are covalently linked to complementary 'anti-handle' sequences. On incubation with the DNA-origami nanostructure, guest molecules are scaffolded by the origami with precision of up to $\sim$ 6 nm. Adapted for ref [68].

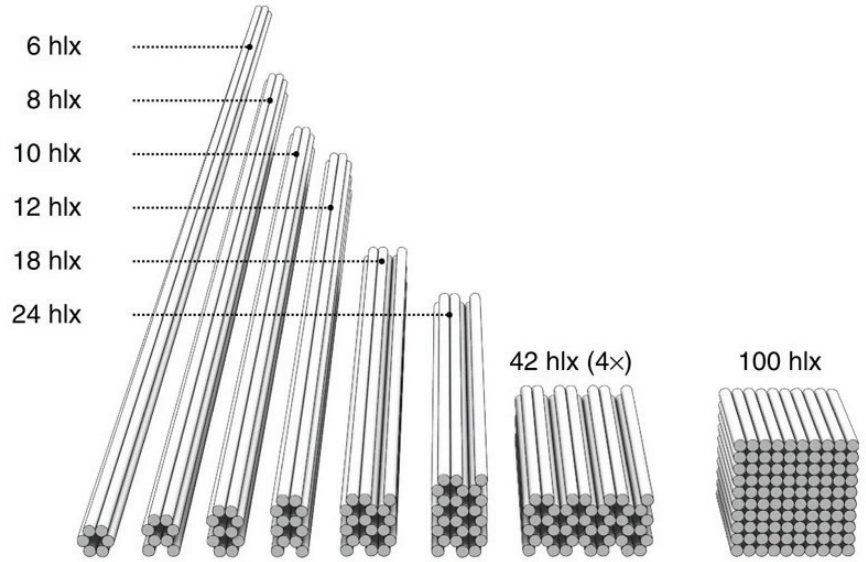

FIGURE 5.2: DNA bundles with various lengths and aspect ratios. Adapted from ref [69].

pairing (Fig. 5.1A) [22]. Since each of the $\sim$ 200 the staple has its unique sequence and can be extended out to form a 'sticky end' to bind with other molecular components (e.g., fluorophores or enzymes), nearly every position on the DNA origami structure can be functionalized independently (Fig. 5.1B-C).

Using active enzyme as propulsive units and coupled onto the highly programmable DNA origami, we can create a new suite of enzyme-powdered programmable active particles. For example, we can build DNA straight bundles with different aspect ratio (Fig. 5.2), rigidity (Fig. 5.3A), and various enzyme-coated patterns (Fig. 5.3B), and study the propulsion mechanism from bottom-up. We can also design asymmetric DNA origami structures as nanoscale probes to investigate the wind of active enzyme bath (Fig. 5.3C). Here, we started with the simplest structure, DNA origami six-helix bundle (6HB). It was composed of six parallel helices with a hexagonal cross section. We decorated the two ends of the DNA 6HB with different Alexa fluorophores and enzymes, making two-fluorophores labeled red-green 6HB and urease-conjugated 6HB.We studied the structure properties and diffusion

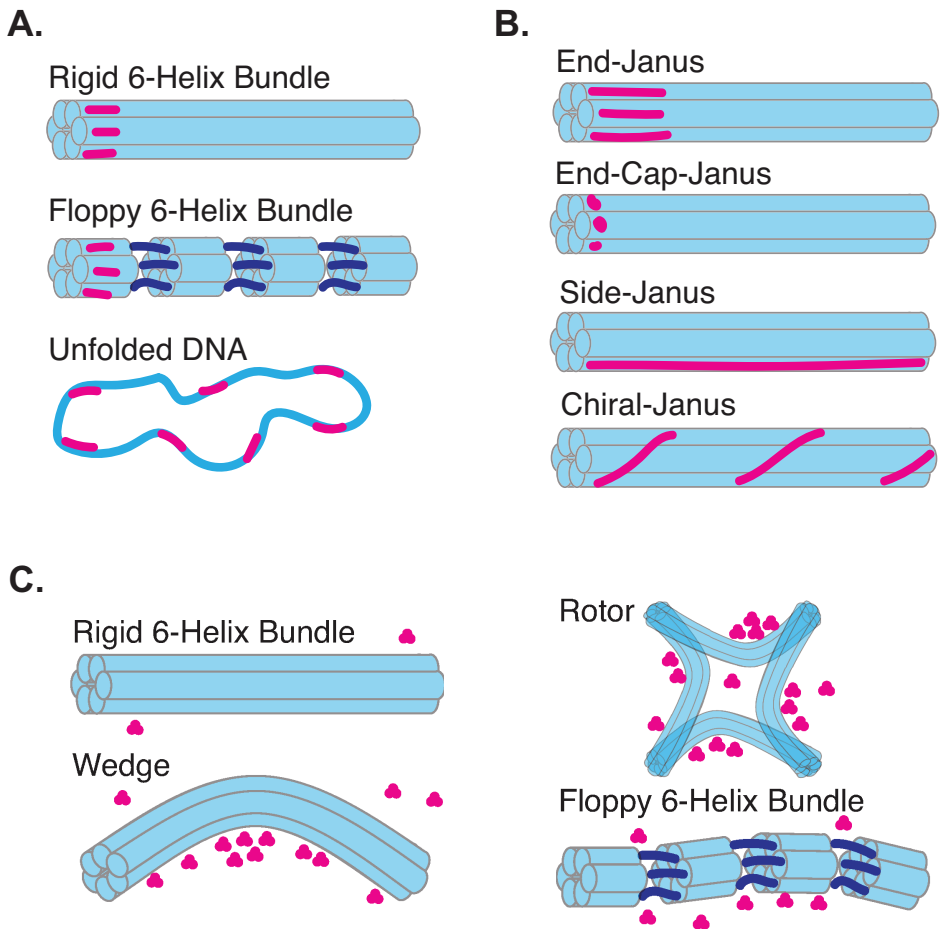

FIGURE 5.3: A) Example designs of various enzyme-coated patterns on rigid 6-helix bundle. Enzymes (pink) can decorate one third, the very end, along the edge, or in a chiral pattern. B) Example designs for different rigidity of DNA-based particles with enzyme (pink) coated on a 6-helix bundle, the same 6-helix bundle with flexible joints, and the same DNA scaffold. C) Example designs of various DNA origami geometries to probe the winds of active enzyme baths. Passive particles rectify the active bath to generate large-scale, persistent motion. A bent wedge and a floppy bundle are predicted to move persistently; A rotor built up from the bent wedges are supposed to rotate persistently. The rigid 6-helix bundle can serve as a control.

dynamics of these functionalized DNA 6HBs using single-molecule imaging techniques as before.

5.2 Method

5.2.1 Fluorescent labeling and Single-strand DNA modification of enzyme

Urease from Jack Bean is purchased from TCI Chemicals. We first fluorescently labeled the urease with Alexa Fluor 647 C_2 maleimide (Thermo Fisher) using a commercially available protein labeling kit following the optimized protocols provided by Thermo Fisher as before. Then we modified the fluorescently labeled urease with thiol-modified DNA oligos (thiol modifier C6 S-S, IDT) following a similar protocol as provided in [70]. Briefly, 100 μl of 7.8 μM fluorescently labeled Alexa647-urease was mixed with 100 μl of 25 μM thiol-modified single-strand DNA (ssDNA) at a mole ratio of 1 to 3. The 200 μl reaction mixture was incubated at 4 °C for 72-96 hr to allow for complete reaction. Afterwards, the free unbound ssDNA was removed by ultrafiltration (MWCO 100kDa, 0.5 ml unit, MilliporeSigma Amicon) for 3 times following the protocols provided by MilliporeSigma. Specifically, The reaction mixture was transferred into the filtration device and centrifuged at 14k rcf for 10 min at room temperature for 3 times. The final concentrated filtrate was collected by putting the filtration device upside down and spun at 1000 rcf for 2 min at room temperature. The concentration of the purified Alexa647-ssDNA-urease was determined by measuring the sample absorbance at 280nm using a UV/Vis spectrophotometer.

5.2.2 Self-assembly and fluorescent labeling of DNA six-helix bundle

Self-assembly of DNA six-helix bundle

DNA six-helix bundle (6HB) was synthesized by mixing a single-stranded scaffold DNA (type p8064, tilibit nanosystem) with 195 different short DNA oligonucleotides (staples, IDT) in a folding buffer. Among the 195 staple strands, 155 were body staple strands (located in the middle of the 6HB), 20 were left handle staple strands (distributed at the first 55nm to the left end) and the other 20 were right handle staple strands (distributed at the first 55nm to the right end). Each of the handle staples has two sequence versions. The active version can hybridize with its complementary DNA strands, thus can be used to conjugate different components on the 6HBs via DNA hybridization, while the passive handle version can not. For each folding reaction mixture, all of the 155 body staples were added, but depending on the number of active handles on each end being needed, different combinations of the 40 handle staples were applied. For example, we can make 6HBs with 20 active handles on each end (20A-20A 6HB), or only 10 active handles on the left (10A-0A 6HB) and so on. For each of these different 6HB versions, we added different handle combinations in the folding mixture.

To be specific, 20 nM of scaffold DNA solution was mixed with 200 nM of each staples (195 in total) in folding buffer with 15 mM magnesium chloride (5 mM TRIS, 1 mM EDTA, 20 mM $MgCl_2$ and 5 mM NaCl; pH 8). The folding reaction mixture was then subjected to a thermal annealing ramp in a thermal cycler (eppendorf): first heated to 65 °C for 15 min and then gradually cooled down from 62.6 °C to 59.6 °C by 1 °C per hour. The folded structures were purified using PEG precipitation to remove the unfolded DNA staple strands. Briefly, 100 μl of the folded

solution was mixed with 100 μl precipitation buffer (15% PEG-8000, 500 mM NaCl), spun at 21k rcf for 30 min at room temperature. Afterwards, the supernatant was removed and the sample (pellet at the bottom of the tube) was redissolved in 100 μl of the folding buffer with 5 mM magnesium chloride (5 mM TRIS, 1 mM EDTA, 5 mM $MgCl_2$ and 5 mM NaCl; pH 8) by incubating at 37 °C for 30 min. Concentration and purification yield of the folded DNA structure was determined by measuring the absorbance of the sample at 260nm using Nanodrop (Thermo Fisher). Purified 6HB was stored at 4 °C until further use.

Fluorescent labeling of DNA six-helix bundle

AlexaFluor-modified DNA oligos were conjugated to active handles on DNA 6HBs via DNA hybridization. There were two types of AlexaFluor-modified DNA oligos: AlexaFluor488-left-anti-handle strands (NHS Ester, complementary to left active handles, IDT) and AlexaFluor647-right-anti-handle strands (NHS Ester, complementary to right active handles, IDT). To conjugate fluorescent dyes on 6HB, AlexaFluor-modified DNA oligos were mixed with a certain version of purified 6HBs (20A-20A, 10E-10E or 5E-5E) at a handle molar ratio of 2:1 (two AlexaFluor-anti-handle strands to one active handle). The reaction mixture was incubated at 30 °C for a 30 min to allow for complete DNA hybridization between AlexaFluor-modified DNA anti-handle strands and active handles on 6HB. The free, unconjugated AlexaFluor-modified DNA strands were then removed by PEG precipitation as described before. The purification yield of the Alexa-6HB was determined by measuring the sample absorbance at 260nm using Nanodrop (Thermo Fisher). Purified Alexa-6HB was stored at 4 °C and protected from light until further use.

5.2.3 Conjugation of enzyme on DNA six-helix bundle

The conjugation of urease on 6HB was performed using the similar protocols as provided in [70]. We first decorated the left end of the 20A-20A 6HB with Alexa488-modified DNA oligos to form a fluorescently labeled Alexa488-20A-6HB. Then, Alexa647-ssDNA-urease (with DNA strands that were complementary to the 20 active right-handles on 6HB) was mixed with Alexa488-20A-6HB at a handle molar ration of 10:1 (ten Alexa647-ssDNA-urease to one active right-handle). The reaction mixture was kept at room temperature overnight to allow fully hybridization. The free, unconjugated ureases were then removed by 4% PEG precipitation. Specifically, 100 μl of the reaction mixture was mixed with 100 μl precipitation buffer (8% PEG-8000, 500 mM NaCl), spun at 4500 rcf for 30 min at room temperature, removed the supernatant and redissolved the sample in 1xPBS buffer with 5 mM magnesium chloride. The purified urease-conjugated 6HB was imaged immediately or at kept 4 °C protected from light and used within a day.

5.2.4 Chamber setup

The flow chambers used for imaging DNA origami samples were the same as that used for imaging single enzymes as described in Chapter 2. Chambers are made from a glass slide, a cover slip (No. 1.5 Fisherbrand, Thermo Scientific), and two pieces of double stick tape. The tape is sandwiched between the slide and the cover slip, acting as a spacer and forming a 5-mm-wide channel. The chamber volume is limited to $\sim$ 10 μl by the thickness of the tape (80 $\sim$ 100 μm in height).

Photobleaching chamber

For photobleaching experiments, to fix the fluorophore-tagged 6HB on the surface, we used silanized coverslips. As described in Chapter 2, coverslips were first cleaned with ultra-violet and ozone (UVO) for 25 min, followed by soaking in acetone for 1 hr, 1 mM KOH for 15 min, and allowed to air dry. Then, the cleaned, dry coverslips were immersed in 2% dimethyldichlorosilane (GE Healthcare, Wauwatosa, WI) for 5 min to be silanized. The silanized coverslips were washed with distilled water for 3 times and were ready to be used after air dry. We used these silanized coverslips to make flow chambers, as described above.

Diffusion chamber

To observed the diffusion of fluorescently labeled 6HB, we applied the lipid bilayer coated chamber as described in Chapter 4. The supported lipid bilayers are made by fusing small unilamellar vesicles (SUVs) on the chamber surface [57]. SUVs are made of POPC (1-palmitoyl-2-oleoyl-glycero-3-phosphocholine) purchased from Avanti. First, 40 μl of 10 mg/ml POPC in chloroform is dissolved in 70 μl of chloroform and mixed well. Chloroform is then evaporated from the mixture under a gentle stream of N_2 gas for 10 min. The lipid mixture is further dried out in a vacuum desiccator for 30 min. The dried lipid is rehydrated in 100 μl PBS buffer and vortexed for 1 min to form giant unilamellar vesicles (GUVs). The white opaque GUV suspension is then sonicated using a sonicator microtip probe (Sonifier) for 3 min to form a clear SUV solution. This clear SUV solution is stored at 4°C and used for the SLB surface coating.

To make SLB-coated flow chambers, 10 μl of SUV solution is first flowed in and incubated for 20 min to allow for the fusion of SUVs to the surface. Excess unfused SUVs are subsequently removed by washing the chamber with PBS buffer 7 times.

The SLB-coated chambers are kept in a humid container to prevent dehydration and taken out immediately before use.

Each chamber contained $\sim$ 100 pM fluorescently labeled 6HB/enzyme-conjugated 6HB to optimize single-molecule imaging, a certain percentage of glycerol, an oxygen scavenging system (10 mM dithiothreitol (DTT), 15 mg/ml glucose, 0.15 mg/ml catalase, and 0.05 mg/ml glucose oxidase) to extend the lifetime of the fluorescent dyes and minimize photobleaching and also enzyme substrate at the desired concentration. DNA 6HB and enzyme samples are imaged immediately after loading and kept measuring for a maximum of 30 minutes before discarding.

5.2.5 Two-color TIRF imaging

Fluorescently labeled DNA 6HB with Alexa488-fluorophores tagged on the left end and Alexa647-fluorophores tagged on the right was imaged using a total internal reflection fluorescence (TIRF) microscope. The TIRF microscope was constructed around a Nikon Ti-E microscope with a custom-built laser system (50 mM 488 nm laser and 100 mW 638 nm laser from CrystaLaser). Imaging is performed with a 60$\times$, 1.49 NA TIRF objective (Nikon), and then magnified an additional 2.5$\times$ before being projected onto an EM-CCD camera (IXON electron-multiplier CCD, Andor). The camera has 512 $\times$ 512 square pixels of 16.2 μm on each side, giving a final magnified pixel size of 107 nm/pixel. Movies were recorded at a rate of 17 frames/s (Δt = 60 ms/frame, ROI = 512$\times$512 pixels) with a 30 ms exposure time using the Nikon Elements software. Laser power and EMCCD gain settings were kept constant for all movies.

We also applied a two-color TIRF imaging system to observe and track the diffusion of the fluorescently labeled 6HB. The two-color TIRF imaging was performed

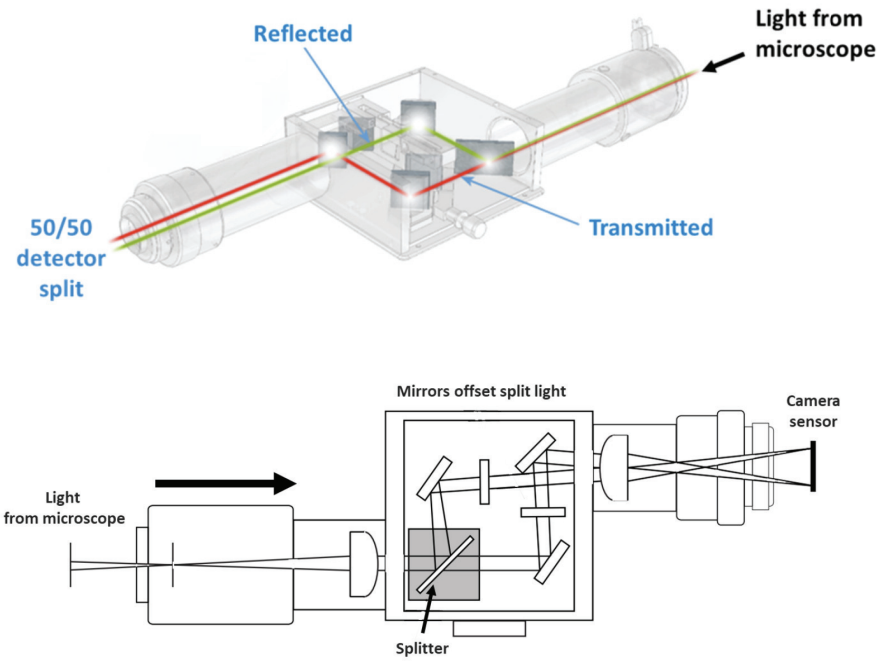

FIGURE 5.4: Schematics of internal components and optical path inside the OptoSplit II image splitter. Emitted light from the sample passes from the microscope to the splitter, which is usually a dichroic mirror. The dichroic mirror then splits the emitted light into two distinct beams of different wavelengths. The two beams are manipulated by mirrors to be re-aligned on the same camera sensor. The sensor is split vertically into two halves. Ideally, each beam is projected on one half of the camera sensor, thus two images of different wavelengths are acquired from one sample.

by adopting a OptoSplit II image splitter to split the image light from the microscope based on wavelength and project it onto different sections of the camera sensor (Fig. 5.4). This way, it allows for a single camera to acquire two emission images at different wavelengths simultaneously, eliminating any delay or need to manually switch filters.

5.3 Single-molecule imaging of fluorescently labeled six-helix bundle

The DNA origami six-helix bundle (6HB) structure was designed and optimized by our collaborator Daichi Hayakawa (Rogers lab, Brandeis University) using caDNAno [71] and an elastic network-guided MD simulation, ENRG-MD simulations [72]. caDNAno is an open-source software that was initially developed in William Shih's laboratory to facilitates the design of a three-dimensional DNA origami nanostructures. The initial designs from caDNAno were then simulated and modified by ENRG-MD simulations to further optimized. Using an elastic network of restrains, ENRG-MD simulation enables the simulation of large DNA-origami objects in a reasonable time.

The final structure of the DNA origami six-helix bundle design was provided in the Appendix B. The total length of the rod-like 6HB was 460 nm and the diameter was 6 nm (aspect ratio $\sim$ 75). The first 55 nm to each end was decorated with single-stranded DNA active handles, so that we can conjugate different components to each end via DNA hybridization among complementary DNA strands (Fig. 5.5A-C). We folded the DNA origami structure from a single-stranded circular DNA scaffold with 8064 bases (isolated from M13mp18 bacteriophages by Florian Praetorius [73]), and 195 short DNA oligonucleotides as staples. The scaffold and staples were mixed in a folding buffer with a certain amount of magnesium chloride ($MgCl_2$) following a thermal annealing ramp. To figure out the optimal folding conditions for our DNA origami six-helix bundle, we performed several initial folding screen tests: magnesium concentration screen (5, 10, 15, 20, 25, 30 mM $MgCl_2$), staple-to-scaffold stoichiometry screen (scaffold:staples = 1:4 or 1:10), and general temperature interval screen (T1: 50.1°C-47.1°C, T2: 52.3°C-49.3°C, T3:

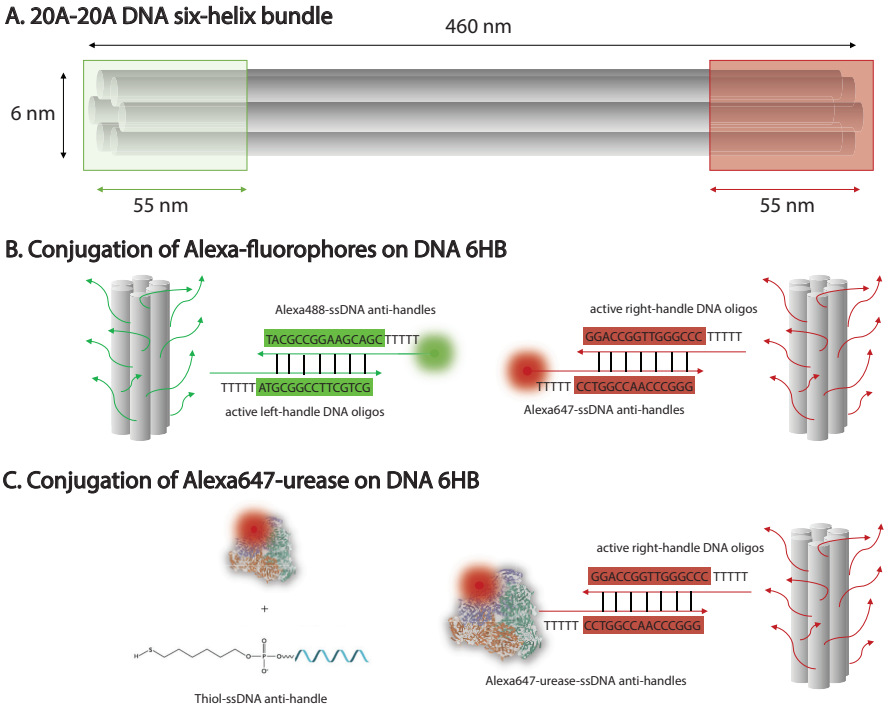

FIGURE 5.5: Schematic of A) DNA six-helix bundle with active handles distributed on first 55 nm to each end, B) conjugation of two different Alexa-fluorophores, Alexa488 (left) and Alexa647 (right), on each end of the 6HB via DNA hybridization, C) conjugation of Alexa647 labeled urease on the right-end of 6HB via DNA hybridization.

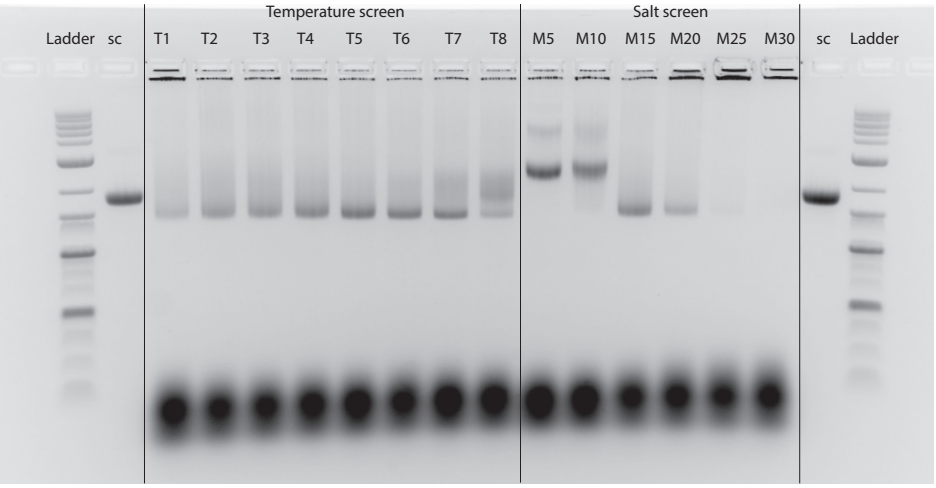

FIGURE 5.6: Initial folding screen of 20A-20A DNA six-helix bundle. Temperature screen was done at 15 mM $MgCl_2$; salt screen was annealed at T4 temperature interval; staple-to-scaffold ratio was all kept as 10:1. Agarose gel: 1.5% agarose, gels ran for 2.5 hours at 110 V on ice. (Ladder: DNA ladder, sc: scaffold)

54.0°C-51.0°C, T4: 55.8°C-52.8°C, T5: 57.7°C-54.7°C, T6: 59.5°C-56.5°C, T7: 62.6°C-59.6°C, T8: 64.1°C-61.1°C,). After folding, we run gel electrophoresis for the folding products on an 1.5% agarose gel (Fig. 5.6, 5.7). The lowest bands are the excess unfolded staple strands since they were added with ten times excess. The bands in the middle are the folded structure that we desired. The upper bands are the pockets, that remains the aggregates of misfolded structures. From the folding screen tests (Fig. 5.6, 5.7), we concluded that the optimum folding condition for making the DNA origami six-helix bundle would be in 15 mM magnesium concentration with a 1:10 scaffold-to-staple ratio and at the T7 (62.6°C-59.6°C) temperature interval. Fig. 5.8 shows the schematic and negative stain TEM images of the folded DNA six-helix bundle (6HB) under different magnifications. The TEM images were provided by our collaborator Daichi Hayakawa (Rogers lab, Brandeis University). The persistence length of the 6HB was $L_p \sim$ 1-2 μm [74].

To better visualize the structure of the folded DNA six-helix bundle (6HB) under

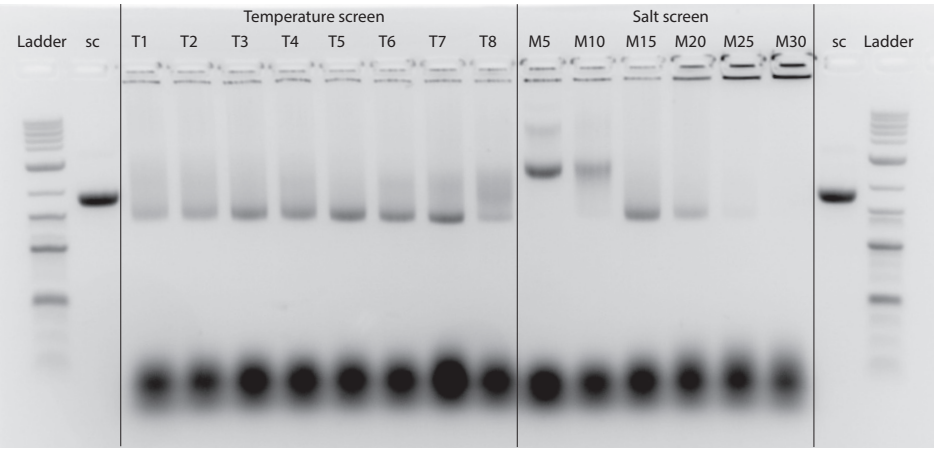

FIGURE 5.7: Initial folding screen of 10A-10A DNA six-helix bundle. Temperature screen was done at 15 mM $MgCl_2$; salt screen was annealed at T4 temperature interval; staple-to-scaffold ratio was all kept as 10:1. Agarose gel: 1.5% agarose, gels ran for 2.5 hours at 110 V on ice. (Ladder: DNA ladder, sc: scaffold)

the TIRF microscope, we first conjugated two different fluorophores on each end of the 6HB rod, AlexaFluor 488 (green) on the left and AlexaFluor 647 (dark red) on the right (Fig. 5.5B). We performed the two-color TIRF imaging for the fluorescent labeled red-green DNA 6HB. Fig. 5.9B shows the 2D projection florescent micrograph of each red-green DNA 6HB fixed on the surface. Suppose most of the DNA 6HBs lie parallel to the surface, we could then estimate the end-to-end distance for each DNA origami rod by measuring the distance between the center of green and red dot. Fig. 5.9C-D shows the distribution of the end-to-end distance measured for DNA 6HB rod. The mean of the end-to-end distance was roughly 415nm. Consider the fluorophores were distributed on the first 55 nm segment to each end, the center of the green and red dot should locate at the middle of each segment for each end, giving the an expected end-to-end distance as 415nm. Thus, the end-to-end distance of the red-green 6HB measured from the two-color 2D projection fluorescent micrograph agreed with the expected value well, which in turn suggested that

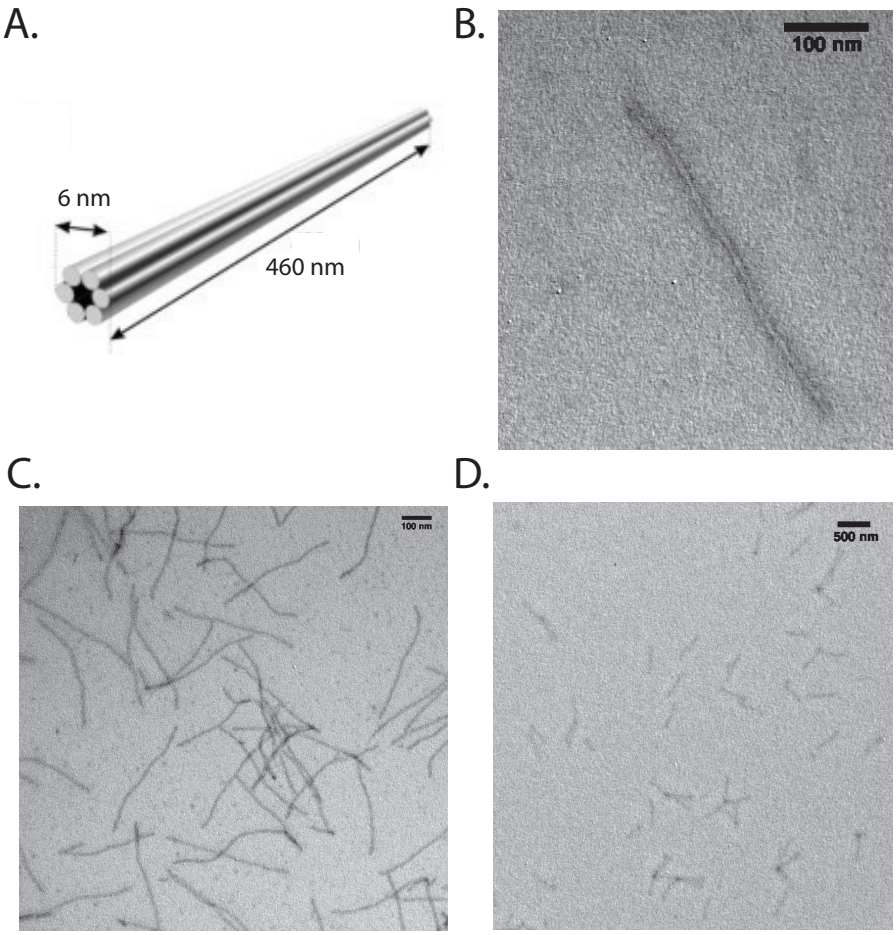

FIGURE 5.8: A) Schematic of DNA origami six-helix bundle. Negative stain TEM of DNA six-helix bundle under different magnifications B) 14000×, C) 11000× and D) 1800×.

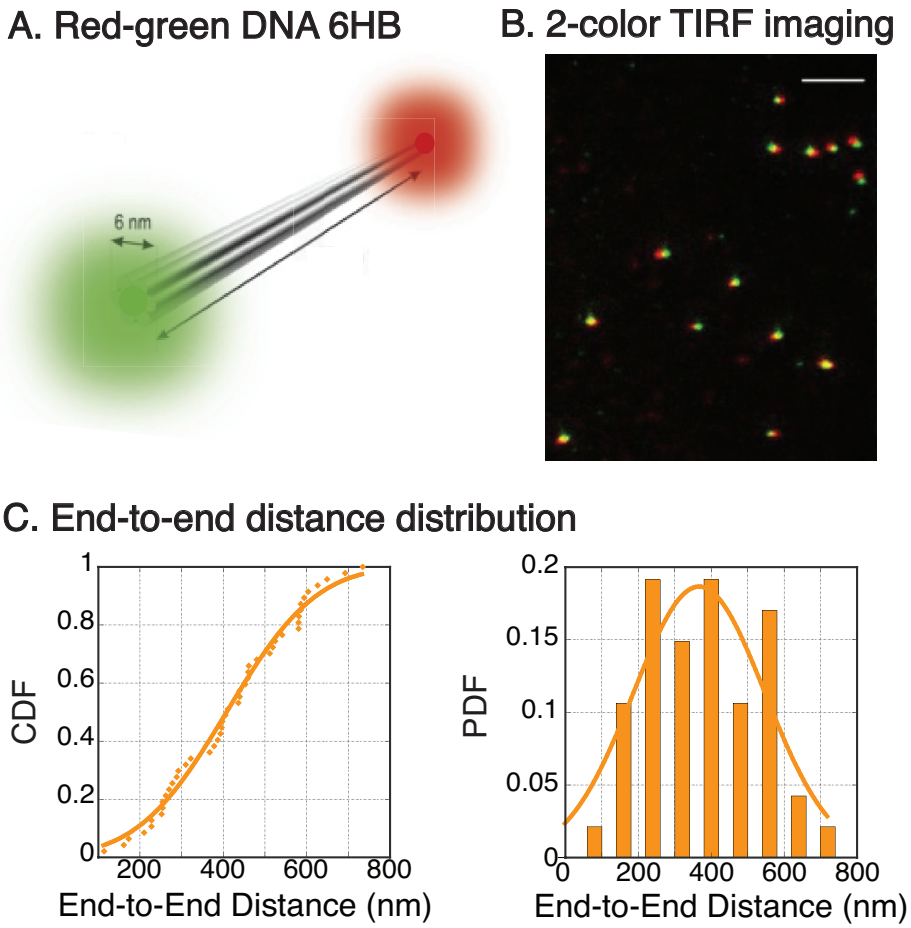

FIGURE 5.9: A) Schematics of fluorescently labeled red-green DNA origami six-helix bundle (6HB) with AlexaFluor 488 (green) on the left and AlexaFluor 647 (dark red) on the right. B) Two-color TIRF imaging of the red-green DNA six-helix bundle (6HB) (scale bar: 5 μm). C) Cumulative distribution (CDF) and probability distribution (PDF) of the end-to-end distance for red-green DNA 6HB. The mean distance is roughly 415 nm, as expected.

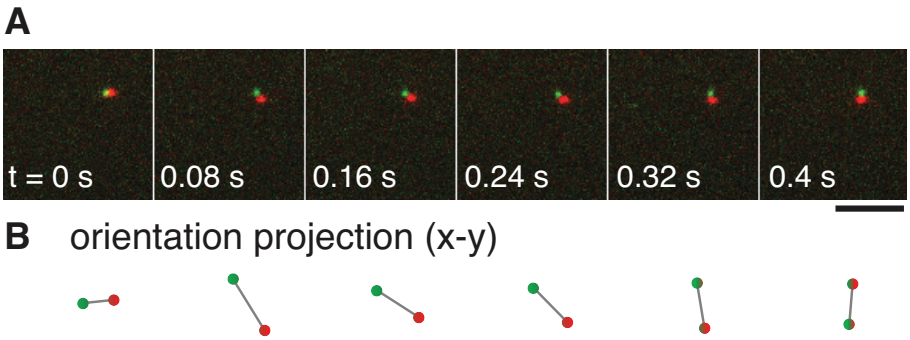

FIGURE 5.10: A) Time series of a single 6HB diffusing over time and B) its orientation at each time stamp (scale bar: 5 μm).

the DNA 6HB rod preferred to lying parallel to the surface. With two different fluorophores tagged on each end, we were also capable of recording the orientation of each red-green DNA 6HB from its two-color 2D projection fluorescent micrograph. Fig. 5.10 shows the time series of a single DNA origami 6HB rod diffusing over time on SLB and its orientation derived from the 2D projection fluorescent micrographs.

5.4 Single-molecule imaging of urease-conjugated six-helix bundle

Next, we tried to combine the active enzymes as discussed in Chapter 2, 3, 4 with the highly programmable DNA origami to build some enzyme-powered nano-rockets as a new suite of self-propelled active particles. The simplest case would be to decorate one end of the DNA 6HB with active enzymes to generate an End-Janus particle. The enzymes equipped on the end were supposed to act as motors, propelling the DNA origami rod moving forward. Based on our former DNA 6HB design, we conjugated AlexaFluor 647 labeled urease on the right end of the 6HB via DNA hybridization, while the left end of the 6HB rod was still coupled with AlexaFluor 488 fluorphores (Fig. 5.5C). Fig. 5.11 shows the TEM images of the urease-conjugated

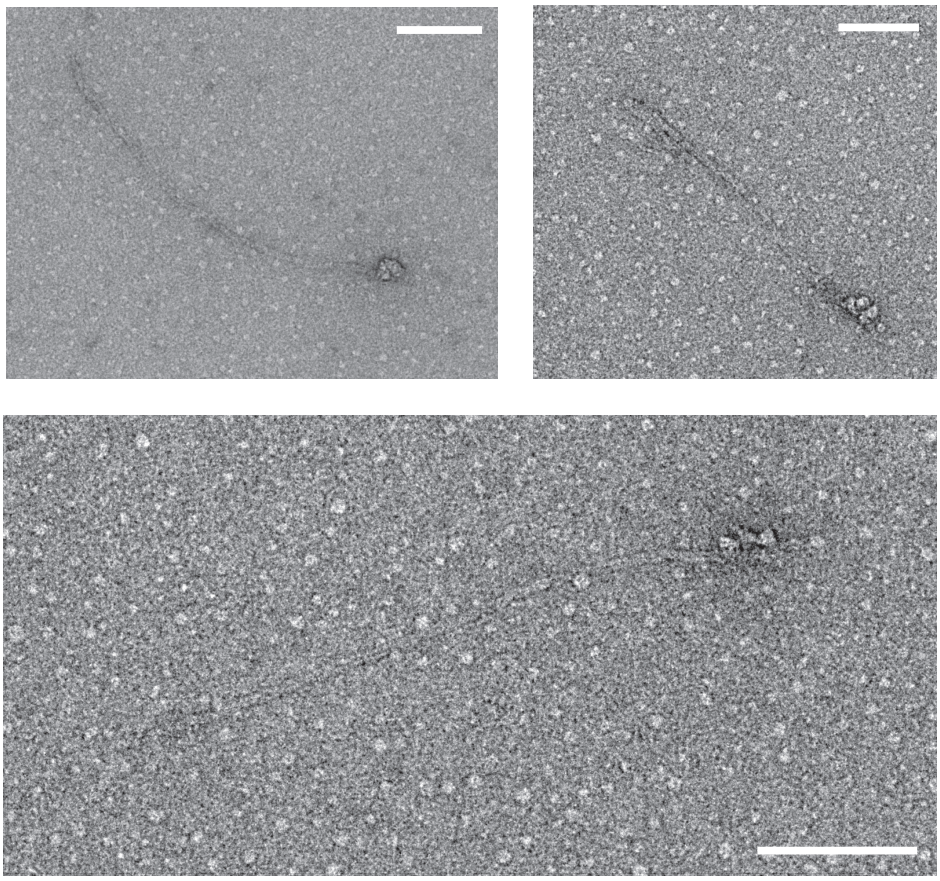

FIGURE 5.11: Negative stain TEM images of urease-conjugated DNA 6HB (scale bar: 100 nm).

6HB, provided by our collaborator Thomas Videbaek (Rogers lab, Brandeis University).The big blobs on the end were the ureases coupled onto the 6HB.

5.4.1 Quantification of urease conjugated on six-helix bundle by photobleaching

In order to quantify the number of urease conjugated on each six-helix bundle, we repeated the photobleaching experiments for the urease-conjugated 6HB as we have previously done for the single enzyme in Chapter 2. Each urease-conjugated 6HB

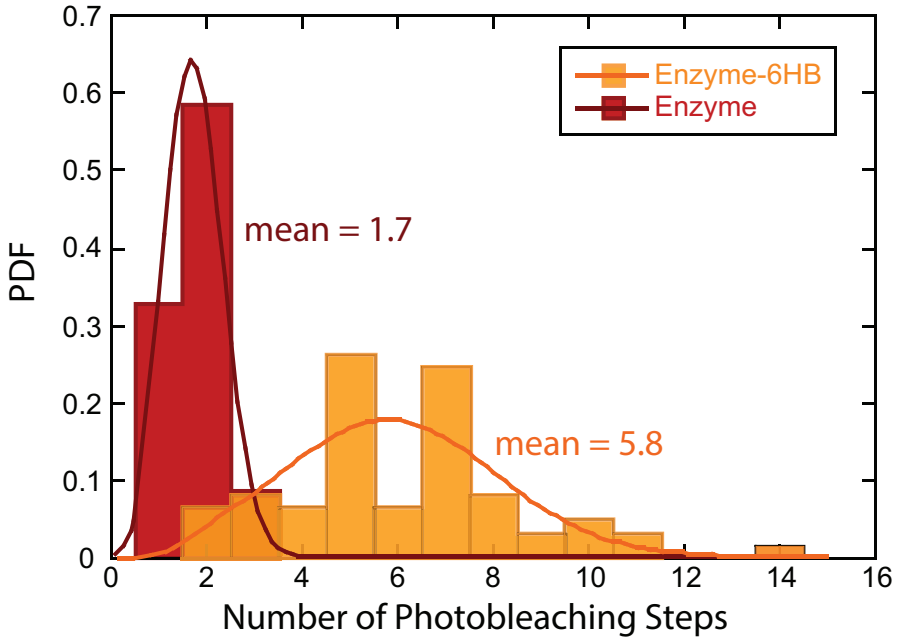

FIGURE 5.12: Histograms of photobleaching steps for urease-conjugated 6HB (orange, $N = 61$) and single urease (red, $N = 58$).

was affixed on the silanized cover glass, making the local laser illumination and z-height constant for the entire measurement. We used the dark red laser line (638nm) of the TIRF microscope to image the urease-coupled end of the 6HB. We found the AlexaFluor 647 fluorophores labeled on urease on the right end of the 6HB photobleached in a stepwise manner over time as expected.

We then counted the number of photobleaching steps for each fluorescent spot, and created a histogram of the number of bleaching events for urease-conjugated 6HB (Fig. 5.12, orange). We also performed the same photobleaching experiments and generated a similar bleaching step histogram for single AlexaFluor647-urease, that was taken from the same batch used for 6HB conjugation (Fig. 5.12, red). Comparing with the photobleaching step histograms for both the urease-conjugated 6HB and the single urease, we found there were only $4 \sim 5$ ureases coupled on each DNA 6HB rod, even if we have 20 enzyme binding sites on it (since we have

20 active handles on the right end).

5.4.2 Steric hindrance simulation

One possible hypothesis for such a low binding efficiency of enzyme would be the steric hindrance. For the right end of the DNA 6HB, there are 20 handles randomly distributed on the 55 nm rod-like segment. The diameter of the rod was 6 nm. The length of the handle was 7.6 nm. The diameter of urease was 14 nm. So, the spacing between two adjacent active handles might not be large enough to allow for both handles being occupied by enzymes. To test for this hypothesis, we run a Monte Carlo simulation to simulate different scenarios for enzyme loading on the end of 6HB. The simulation was performed by our collaborator Daichi Hayakawa (Rogers lab, Brandeis University). Briefly, each urease was assumed as a sphere with a diameter of 14nm and the position was represented by its center. The sphere center was then place on the surface of a 55 nm (height) $\times$ 17.6 nm (Radius = 3 nm (radius of 6HB) + 7.6 nm (length of handle) + 7 nm (radius of urease)) cylinder to mimic the enzyme binding on 6HB via a 7.6 nm-handle. Fig. 5.13 shows the simulated results of how enzyme loading efficiency changes as a function of minimal allowed distance between enzyme centers in different configuration. We found that when the minimal allowed distance between enzyme centers was larger than 17 nm (comparable to the enzyme diameter 14 nm), the maximum number of enzyme being loaded was only around 10 $\sim$ 12. This finding was also in agreement with what we observed in our photobleaching experiments (Fig. 5.12): the maximum photobleaching steps were 14, which roughly corresponded to 8 $\sim$ 9 enzymes loaded (comparable to the simulated result of 10 $\sim$ 12 enzymes).

We also noticed that the configurations of how enzyme located on the cylinder

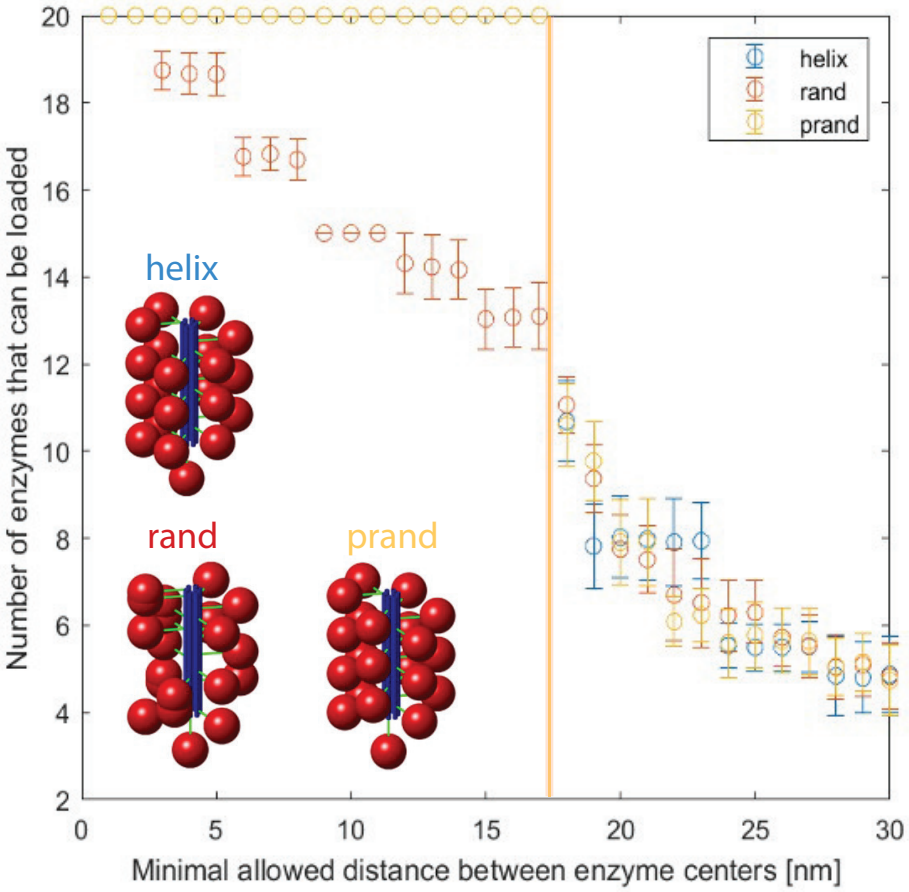

FIGURE 5.13: Simulation results of how enzyme loading efficiency changes as a function of minimal allowed distance between enzyme centers in different configuration. (helix: helix configuration; rand: random configuration; prand: periodic random configuration.)

seemed no longer affect the enzyme loading efficiency too much when the minimal allowed distance was larger than 17nm. This implied that, in reality, when the minimal allowed distance between enzymes was always larger than 14 nm, the configurations of how handles distributed on the 6HB would only have a slight impact on the enzyme binding efficiency. Our photobleaching experiments showed that there were only 4 or 5 ureases conjugated on each DNA 6HB. Combining with the simulation results in Fig. 5.13, when $4 \sim 5$ enzymes being loaded, the minimal distance between enzymes should be at least 30 nm. This might imply that enzymes prefer to have a spacing larger than 30 nm in the real case.

To further check the steric hindrance hypothesis, we performed another set of photobleaching experiments. We made three different versions of DNA 6HB with different spacing among adjacent handles: 5E-5E, 10E-10E and 20A-20A. By exploiting the highly programmable nature of DNA origami, we can easily achieve this by selectively activating specific handles on each end. Since each end was designed to have 20 active handle maximum, for 5E-5E or 10E-10E version, only five or ten handles were activated to be able to conjugate with enzymes or fluorophores. These handles were choose equally distribute along the 55 nm on each end. Thus, versions with fewer handles would have a larger distance between two adjacent handles and have lower steric hindrance effect. The spacing among handles for these three versions would be: $d_{\text{5E-5E}} > d_{\text{10E-10E}} > d_{\text{20A-20A}}$, and correspondingly, we would expect the loading efficiency among the three versions to be: $E_{\text{5E-5E}} > E_{\text{10E-10E}} > E_{\text{20A-20A}}$. This was in agreement with what we found in our photobleaching experiments (Fig. 5.14). For 5E-5E, the average number of loaded enzymes was $2 \sim 3$, giving a loading efficiency as $d_{\text{5E-5E}} = 41\%$; for 10E-10E, the average loading number was $3 \sim 4$ and loading efficiency was $d_{\text{10E-10E}} = 26\%$; for 20A-20A, the average number was $4 \sim 5$ with a loading efficiency $d_{\text{20A-20A}} = 17\%$. However, as shown in Fig. 5.14, even for

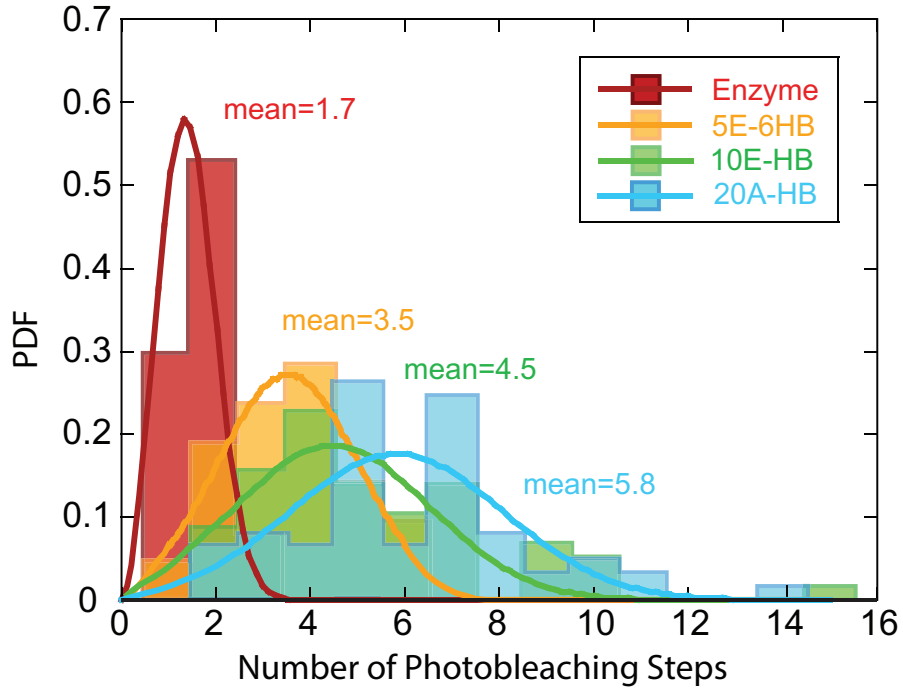

FIGURE 5.14: Histograms of photobleaching steps for urease-conjugated 20A-20A 6HB (blue, $N = 61$); 10E-10E 6HB (green, $N = 57$); 5E-5E 6HB (orange, $N = 42$) and single urease (red, $N = 58$).

the largest spacing version 5E-5E, the loading efficiency was still very low, only $\sim$ 41%. Therefore, there might be other factors that also play a role in limiting enzyme occupancy.

Another possible scenario would be the undesired entanglement among adjacent active handles. Since the active handles are single-strand DNA oligos, they are sticky. They might be mispairing with its neighbor handles and preventing the desired hybridization with their complementary strands. To avoid this scenario, a larger spacing among handles is promoted, and the sticky sequence of the active handle should be carefully designed to prevent self-pairing.

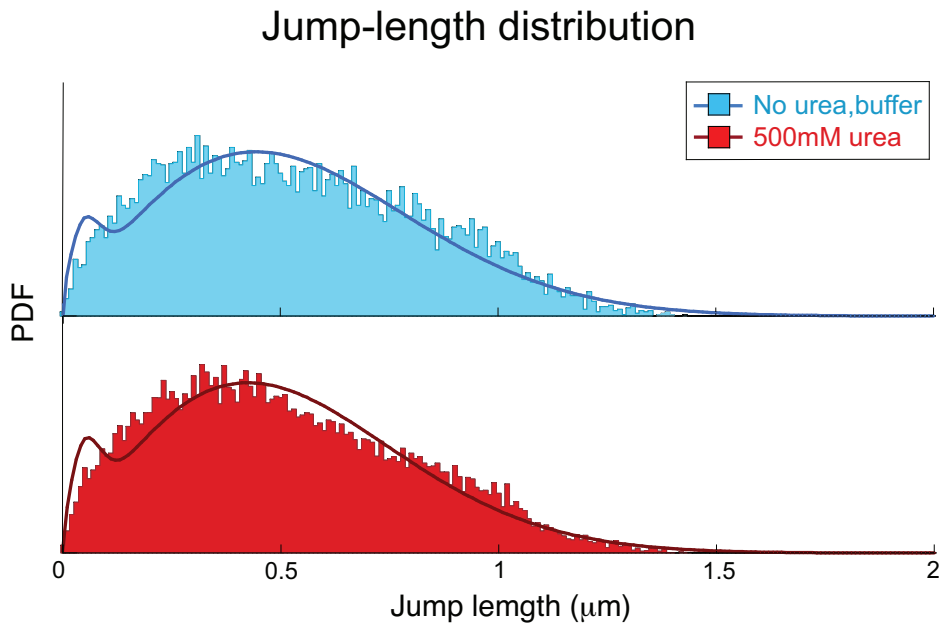

FIGURE 5.15: Jump-length distributions of urease-6HB diffusing in buffer and 500 mM urea. Solid dark line shows the corresponding kinetic model fit from Spot-On analysis for each jump-length distribution.

5.4.3 Diffusion of enzyme-conjugated DNA six-helix bundle with and without the presence of urea

We also performed the diffusion experiments for urease-conjugated 6HB (20A-20A) with and without the presence of urea. Fig. 5.15 shows the jump-length distributions of urease-conjugated 6HB in buffer and in 500 mM urea solution. No obvious shift is observed in jump-length for the urease-conjugated 6HB diffusing in urea conditions. After kinetic model fitting from Spot-On, we derive the diffusion coefficient for each case: D_{buffer} = 4.334 μm^2/s, while D_{urea} = 3.953 μm^2/s. Thus, no relative increase but even a slight decrease was found for urease-conjugated 6HB diffusing in 500 mM urea. We were not surprised by the lack of enhancement for urease-conjugated 6HB. Since there were only 4 $\sim$ 5 enzymes coupled on the huge 460 nm-6HB rod, with such few motors conjugated, it's reasonable that we cannot

tell any self-propulsion or enhanced diffusion as expected.

5.5 A new DNA origami design — 24-helix bundle

In attempt to maximize enzyme loading, we constructed a new DNA origami bundle structure of twenty-four helix bundles with more enzyme loading sites (68 active handles for enzyme binding maximum) and a larger inter-handle spacing (Fig. 5.16A). We also adopted a new set of DNA handle sequences to better stabilize the enzyme conjugation and minimize self-pairing (Fig. 5.16B). This new design and the new handle sequences were provided by our collaborator Daichi Hayakawa and Thomas Videbaek (Rogers lab, Brandeis University) (Appendix B). The 24-helix bundle was folded by mixing the same circular DNA scaffold (8064 bp isolated from M13mp18 bacteriophages, 50 nM) with 211 short DNA staples (200 nM) in folding buffer with 15 mM magnesium chloride and following a thermal annealing ramp (65 °C for 15 min, 58 °C to 48 °C 1 °C per hour). Fig. 5.17A showed the gel electrophoresis results of the folded 24-helix bundle with no active handles, all 68 active handles and 38 selected handles. Compared with the band of 6-helix bundle with 20 active handles, the yield for 24HB was extremely high, with only a few unfolded staples left over. The band of 68A-24HB and 38A-24HB ran a little behind that of the 0A-24HB because of those fluffy active handles extending out from the bundle surface. Fig. 5.17B showed the negative stain TEM images of the folded 24-helix bundle with zero active handles and all 68 active handles, provided by our collaborator Daichi Hayakawa (Rogers lab, Brandeis University).

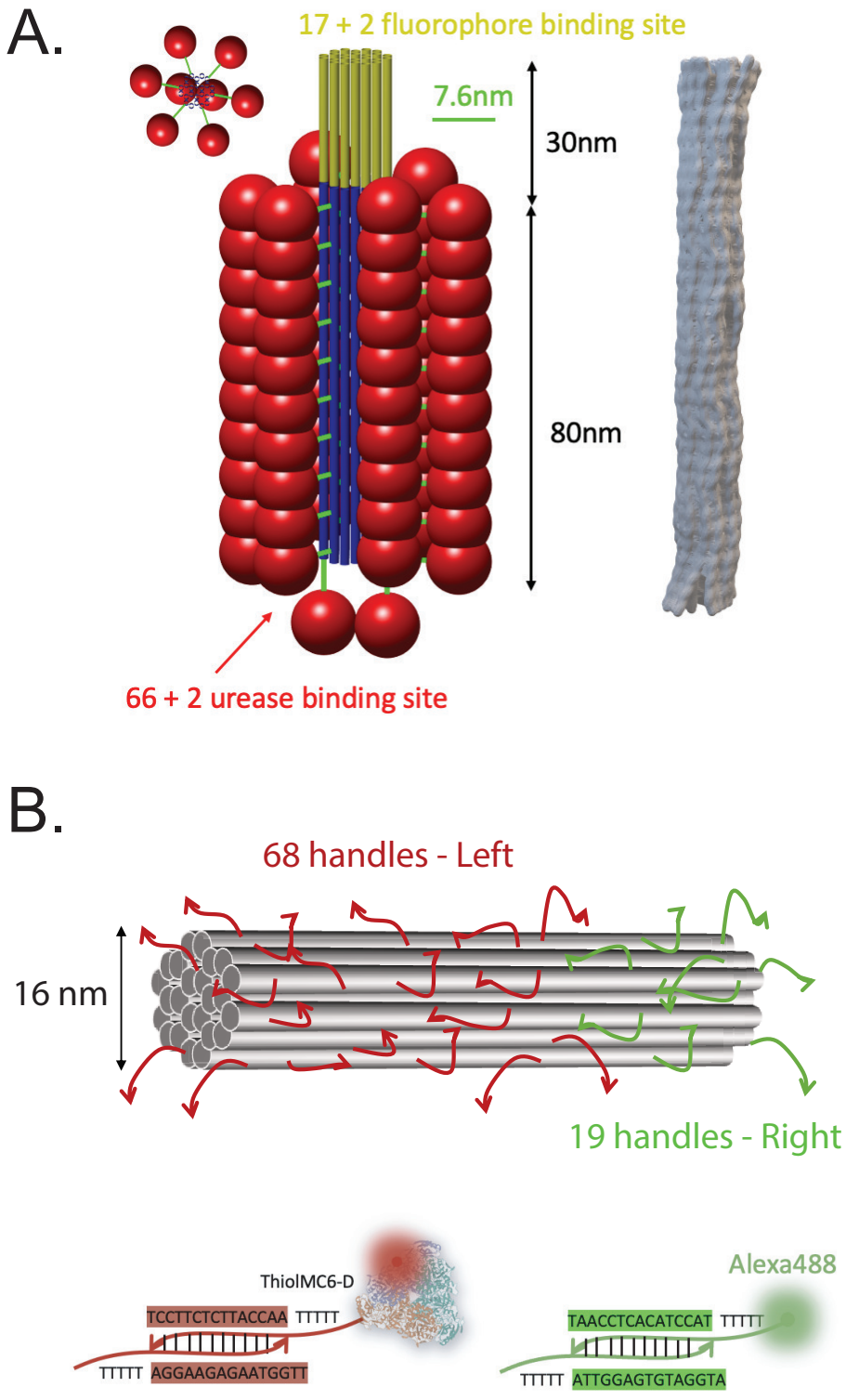

FIGURE 5.16: A) Schematics of enzyme-conjugated 24-helix bundle with maximum 68 enzymes (red sphere, attached on blue part of the bundle) and 19 fluorophores (not shown, distributed on yellow part of the bundle) loaded; B) Schematics of 24-helix bundle with active handles on each end (Red: for enzyme conjugation; Green: for fluorophore conjugation) and the new set of handle sequences.

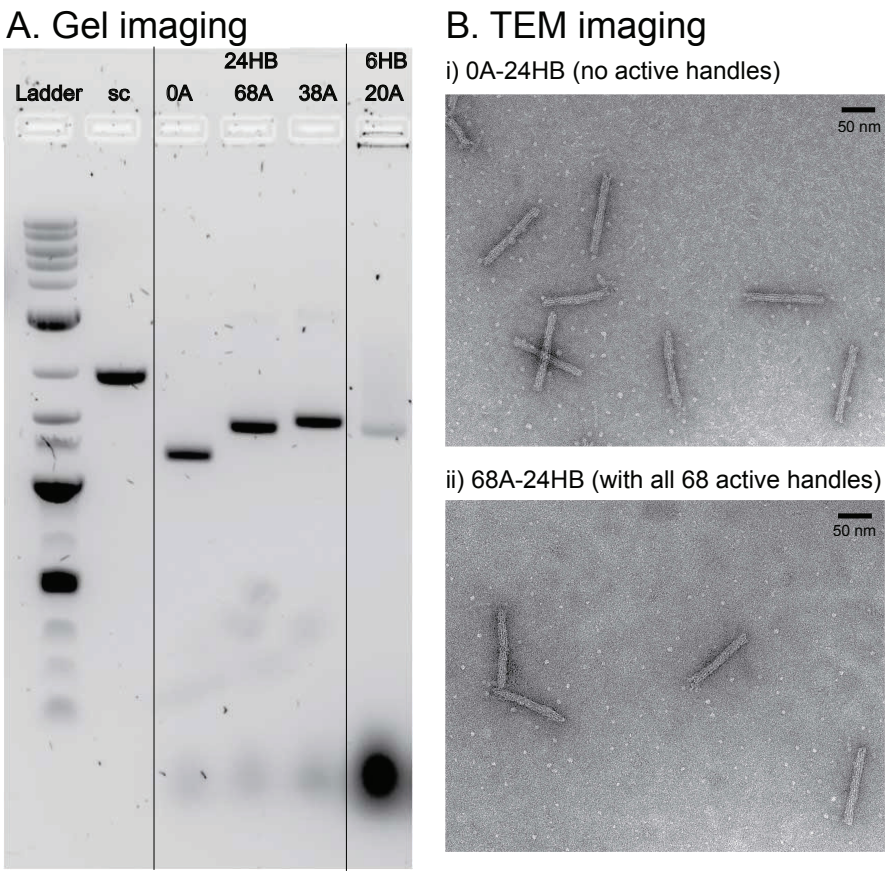

FIGURE 5.17: A) Gel imaging of 24HB (0A, 68A, 38A) and 6HB (20A); B) Negative stain TEM images of 0A-24HB and 68A-24HB. Fluffy active handles cannot be recognized due to the limitation of the resolution (magnification: 40000×).

5.6 Conclusion

In this chapter, we seek to combine the active enzymes that have been fully studied in the former chapters (Chapter 2, 3, 4) with highly programmable DNA origami to build some enzyme-powered nano-rockets as a new suite of self-propelled active particles and study the mechanism of propulsion from the bottom-up. We started with the simplest DNA origami structure, six-helix bundle. We found the optimum folding conditions for making DNA six-helix bundle by running several initial folding screen tests and verified the rod-like structure under transmission electron microscope (TEM). We also conjugated two different fluorophores on each end the DNA 6HB and estimated the end-to-end distance of 6HB as 415 nm using two-color TIRF imaging. We then tried to conjugate urease on one end of the 6HB to create an End-Janus particle. The urease-conjugated 6HB was imaged by both TEM and two-color TIRF microscope. We found there were only 4 to 5 ureases conjugated on each DNA 6HB by photobleaching experiments. With such few enzyme conjugated, we did not observe any self-propulsion or enhanced diffusion of the urease-conjugated 6HB in the presence of urea as expected. We suspected this low binding efficiency was due to the steric hindrance of the current design. We ran a Monte Carlo simulation and found the optimal spacing for urease to load was at least 30 nm. Thus, a larger handle spacing and a less self-pairing handle sequence is needed for the future designs. We therefore constructed a new DNA origami straight bundle with twenty-four parallel helices (24HB) for more enzyme loading sties and larger inter-handle spacing as the beginning of the next step.

Chapter 6

Conclusion and Outlook

The aim of this work is to use a distinct method to measure the diffusion of enzymes and test if the enhanced diffusion was genuine or an artifact of the previously reported FCS measurements. Excitingly, we verified that the enhanced diffusion of urease occurred on a truly single molecule level. We found that the enhanced diffusion was Brownian - not anomalous. We also observed a higher increase in diffusion rates, by a factor of three, in comparison with the $\sim$ 30% increase previously reported. The large increase in diffusion was difficult to account for based on current physical models of heat release or collective interactions. To test if the huge enhancement was caused by the dissociation of enzyme multimers, we directly measured the oligomerization state of the enzymes using single molecule imaging techniques, and excluded this possibility. Finally, we applied the same single-molecule diffusion measurements on aldolase, a slow and endothermic enzyme. We observed a two-phase changing of aldolase diffusion behavior: a reduced diffusion at low substrate concentration and a $\sim$ 30% enhanced diffusion at high substrate concentration. We also compared different experimental designs and different data analysis methods for single-molecule imaging of enhanced enzyme diffusion experiments. We found that the 2D confinement of urease to a fluid lipid bilayer conserved the enhanced enzyme diffusion, recapitulating the 3-fold

enhancement of urease at the saturation concentration of urea, as we previously observed. To minimize the chamber complexity, we designed a new chamber with a well-characterized SLB coated surface and a small viscous molecule, glycerol, to replace the bulky polymers used in the prior F127 polymer brush design. We confirmed the efficacy of the newly-designed SLB/glycerol chamber by measuring the diffusion of different-size particles in different viscosity solutions. We found that particles diffused as the Stokes-Einstein equation predicts: their diffusion coefficients scaled inversely with solvent viscosity η and particle size R. For the two data analysis methods for SPT: the MSD analysis and the jump-length analysis, we found that MSD analysis was appropriate for analyzing slowly diffusing species, when high solvent viscosity or large particle size are preferable. While analyzing fast diffusion, MSD analysis under-counted the population of fast-moving particles, leading to an underestimation of the actual diffusion coefficient. Jump-length analysis seemed to be applicable for a wider range, from very slow diffusion to relatively fast motion. However, we also noticed that for jump-length analysis the diffusion coefficients reported depend heavily on the parameters, especially one of the input parameters in MTT tracking algorithm, $D_{\max}$. Thus, care must be taken when choosing parameters and a dataset of all key parameters used for the analysis should be reported specifically to allow for reproducibility and transparency when using this method. We also examined how urease diffused in the SLB/glycerol chamber with and without the presence of urea. We measured the diffusion of urease at two viscosity regimes: the high viscosity regime with 75% glycerol and the low viscosity regime with 30% glycerol. However, no enhanced diffusion was observed for urease at either viscosity due to the inactivation of urease by glycerol. When we performed the same urease diffusion experiments in buffer solution

without glycerol, the enzymes diffused too fast in buffer to allow for accurate diffusion measurements. Taken together, we found that the previously employed F127 polymer brush chamber seemed to be excellent at slowing down enzyme motility without inhibiting its activity. The tethered enzyme experimental design demonstrated in this work was also a viable strategy. We also combined the active enzymes with highly programmable DNA origami to build some enzyme-powered nano-rockets as a new suite of self-propelled active particles and study the mechanism of propulsion from the bottom-up. We started with the simplest DNA origami structure, six-helix bundle. We found the optimum folding conditions for making DNA six-helix bundle by running several initial folding screen tests and verified the rod-like structure under transmission electron microscope (TEM). We also conjugated two different fluorophores on each end the DNA 6HB and estimated the end-to-end distance of 6HB as 415 nm using two-color TIRF imaging. We then tried to conjugate urease on one end of the 6HB to create an End-Janus particle. The urease-conjugated 6HB was imaged by both TEM and two-color TIRF microscope. We found there were only 4 to 5 ureases conjugated on each DNA 6HB by photobleaching experiments. With such few enzyme conjugated, we did not observe any self-propulsion or enhanced diffusion of the urease-conjugated 6HB in the presence of urea as expected. We suspected this low binding efficiency was due to the steric hindrance of the current design. We run a Monte Carlo simulation and found the optimal spacing for urease to load was at least 30nm. Thus, we constructed a new DNA origami bundle structure with 24-helix bundles to have more enzyme loading sites and a larger inter-handle distance for future investigations.

For the enhanced enzyme diffusion project, we expect the direct imaging technique will be a powerful, complementary method and contribute new insights into

the future investigations of the mechanism behind enhanced enzyme diffusion. While an optimized experimental design, as well as a more intuitive, less parameter-related data analysis approach, are still in demand. For the programmable active particles project that combines enzyme with DNA origami, a more optimized DNA origami design is needed to allow for more enzyme to be loaded and achieve enzyme-powered propulsion. Also, to better acquire the translational motion as well as the rotational motion of the DNA 6HB rod, a more advanced microscope setup is required for a 2-color, 3D-imaging. Otherwise, we can also tether the DNA 6HB on the lipid surface to confine the motion to 2D as what we have done for the single enzyme. There are also some other future directions that combines enzymes both with lipid and DNA origami might be worthwhile a try. We can try building self-propelled liposomes by tethering active enzymes on lipid vesicles via DNA hybridization or biotin-avidin linkers. Enzyme cascades can also be introduced on the lipid vesicles to see if any emergent pattern formation would occur. Inspired by the former work about DNA origami nanopores, we can also try building liposomes with nanopores and enzymes encapsulated to create a new version of enzyme-powered Janus-particles. Finally, enzymes can also be incorporated into the studies of synthetic cells, acting as one of the molecule building blocks and contributing to the final construction of a self-functionalized artificial cell that can shape, divide by itself from the bottom-up.

Appendix A

Fit Parameters

Gaussian fit:

$$PDF = A \times \exp\big[-\frac{(log(D) - < log(D) >)^2}{2\sigma^2}\big], \tag{A.1}$$

We fit the histograms of log$D$ with Eqn. A.1. The mean of each Gaussian fit is transformed back to the typical diffusion units, acting as the apparent diffusion coefficient for each case. Error bars are obtained from the standard error of the each Gaussian fit. The top of the error bar is determined by adding the mean by the standard error to determine the right-most edge of the Gaussian width and then taking that as the power of 10 to transform it back to D. The bottom of the error bar is determined by the same way except subtracting the standard error. The fit parameters for each experiment are given in the Table A.1. N denotes the number of trajectories contributing to each distribution histogram and was used to calculate the standard error of each Gaussian fit. χ^2 denotes the Chi-Square goodness of the fit.

[urea]	N	A	$< log(D/(m^2/s)) >$	σ	χ^2
buffer	141	0.135 ± 0.010	-12.77 ± 0.02	0.295 ± 0.025	0.0119
10μM	97	0.115 ± 0.007	-12.51 ± 0.02	0.330 ± 0.025	0.0076
100μM	207	0.086 ± 0.005	-12.41 ± 0.03	0.474 ± 0.034	0.0054
1mM	178	0.095 ± 0.005	-12.21 ± 0.02	0.400 ± 0.025	0.0043
10mM	161	0.084 ± 0.003	-12.38 ± 0.02	0.458 ± 0.022	0.0023
100mM	203	0.074 ± 0.004	-12.22 ± 0.03	0.538 ± 0.032	0.0031

TABLE A.1: Fit parameters to Gaussian fit Eqn. A.1 for log transformed diffusion data under each urea concentration shown in Fig. 2.5.

[urea]	N	A	$<\log(D/(\mu m^2/s))>$	σ	χ^2
buffer	178	0.047 ± 0.002	-1.084 ± 0.050	1.176 ± 0.071	0.0035
200 mM	484	0.053 ± 0.002	-0.627 ± 0.040	1.371 ± 0.077	0.0034

TABLE A.2: Fit parameters to Gaussian fit Eqn. A.1 for log transformed diffusion data under each urea concentration shown in Fig. 3.2.

[urea]	N	A	$<\log(D/(\mu m^2/s))>$	σ	χ^2
buffer	663	0.056 ± 0.002	-0.197 ± 0.036	1.424 ± 0.073	0.0025
1 mM	877	0.060 ± 0.003	0.036 ± 0.040	1.628 ± 0.106	0.0041

TABLE A.3: Fit parameters to Gaussian fit Eqn. A.1 for log transformed diffusion data under each urea concentration shown in Fig. 3.4.

glycerol%	N	A	$<\log(D/(\mu m^2/s))>$	σ	χ^2
30%	10	0.359 ± 0.031	0.061 ± 0.008	0.082 ± 0.008	0.0331
50%	420	0.168 ± 0.004	0.055 ± 0.007	0.223 ± 0.007	0.0019
60%	109	0.116 ± 0.006	0.202 ± 0.020	0.339 ± 0.020	0.0052
70%	313	0.131 ± 0.005	0.092 ± 0.013	0.303 ± 0.013	0.0033
75%	97	0.196 ± 0.006	0.029 ± 0.008	0.198 ± 0.008	0.0037
80%	676	0.176 ± 0.004	-0.162 ± 0.006	0.213 ± 0.006	0.0018
85%	736	0.143 ± 0.002	-0.341 ± 0.005	0.269 ± 0.005	0.0006
90%	213	0.122 ± 0.004	-0.533 ± 0.013	0.313 ± 0.013	0.0026

TABLE A.4: Fit parameters to Gaussian fit Eqn. 2.1 for log transformed diffusion data under each urea concentration shown in Fig. 4.3.

Particle	N	A	$<\log(D/(\mu m^2/s))>$	σ	χ^2
GFP	49	0.135 ± 0.013	0.073 ± 0.030	0.268 ± 0.030	0.0218
aldolase	97	0.196 ± 0.006	0.029 ± 0.007	0.198 ± 0.007	0.0037
urease	113	0.180 ± 0.008	0.097 ± 0.016	0.220 ± 0.016	0.0129
plastic sphere	46	0.147 ± 0.011	-1.223 ± 0.017	0.278 ± 0.017	0.0082

TABLE A.5: Fit parameters to Gaussian fit Eqn. A.1 for log transformed diffusion data under each urea concentration shown in Fig. 4.4.

[urea]	N	A	$<\log(D/(\mu m^2/s))>$	σ	χ^2
buffer	178	0.205 ± 0.009	-0.011 ± 0.009	0.193 ± 0.009	0.0065
1 μM	188	0.200 ± 0.004	-0.074 ± 0.005	0.201 ± 0.005	0.0017
10 μM	205	0.244 ± 0.009	-0.060 ± 0.007	0.160 ± 0.007	0.0059
100 μM	701	0.207 ± 0.004	-0.055 ± 0.004	0.191 ± 0.004	0.0014
500 μM	456	0.208 ± 0.003	-0.113 ± 0.003	0.190 ± 0.003	0.0006
1 mM	390	0.187 ± 0.002	-0.092 ± 0.003	0.215 ± 0.003	0.0004
10 mM	383	0.199 ± 0.007	-0.078 ± 0.008	0.201 ± 0.008	0.0043
100 mM	357	0.211 ± 0.003	-0.101 ± 0.004	0.189 ± 0.004	0.0010

TABLE A.6: Fit parameters to Gaussian fit Eqn. A.1 for log transformed diffusion data under each urea concentration shown in Fig. 4.5.

[FBP]	N	A	$<\log(D/(\mu m^2/s))>$	σ	χ^2
buffer	149	0.176 ± 0.004	-0.705 ± 0.006	0.219 ± 0.006	0.0020
1 μM	117	0.150 ± 0.007	-0.831 ± 0.014	0.253 ± 0.014	0.0062
10 μM	594	0.128 ± 0.004	-0.981 ± 0.012	0.303 ± 0.012	0.0029
100 μM	110	0.130 ± 0.007	-1.034 ± 0.017	0.284 ± 0.017	0.0063
1 mM	63	0.118 ± 0.005	-0.803 ± 0.016	0.326 ± 0.016	0.0039
10 mM	78	0.092 ± 0.008	-0.681 ± 0.036	0.380 ± 0.039	0.0104
100 mM	306	0.194 ± 0.005	-0.548 ± 0.006	0.207 ± 0.006	0.0024

TABLE A.7: Fit parameters to Gaussian fit Eqn. A.1 for log transformed diffusion data under each FBP concentration shown in Fig. 2.11.

Hyperbolic fit:

$$(D - D_0)/D_0 = A \times \frac{[urea]}{[urea] + K'}, \tag{A.2}$$

A	K (mM)	χ^2	R^2
2.2 ± 0.3	0.03 ± 0.03	1.2	0.78

TABLE A.8: Fit parameters to Eqn. A.2 for the data shown in Fig. 2.5 B, with amplitude constant A and kinetic rate constant K.

Parameter settings used for MTT algorithm:

Experiments	ExposureTime	$D_{\max}$	Gaps
aldolase in 90% gly	60	1.4	3
aldolase in 85% gly	60	2	3
aldolase in 80% gly	60	2	3
aldolase in 75% gly	60	5	3
aldolase in 70% gly	60	7	3
aldolase in 60% gly	60	8	3
aldolase in 50% gly	60	20	3
aldolase in 30% gly	60	25	3
GFP in 75% gly	60	10	3
urease in 75% gly	60	3	3
plastic spheres in 75% gly	60	1	3
urease, 30% gly, no urea	9.5	30	2
urease, 30% gly, 200mM urea	9.5	40	2
urease, buffer, no urea	9.5	50	2
urease, buffer, 200mM urea	9.5	70	2

TABLE A.9: Parameter settings used in MTT algorithm for each experimental case, with LocalizationError = -6.25, EmissionWavelength = 647, NumDeflationLoops = 0 for all cases. (gly: glycerol; $D_{\max}$: MaxExpectedD; Gaps: NumGapsAllowed)

Appendix B

DNA origami sequence

Sequence of short single-stranded oligonucleotides (staples, 5′-3′):

TABLE B.1: 6HB staple sequence - body1

Well	Name	Sequence-body1
A1	Body 1	TCTGTCCAGCCGATTAAAGGGATTTTAGACCGAGT
B1	Body 2	ACTATGGTCGTTAGCGGTACGCCAGAAT
C1	Body 3	GGTGGTTGGTCAGTCAGTGCCACGCTGATATTAACAAAACAT
D1	Body 4	AATATCTCCGAAATATTAGTCTTTAATGCGCGAGTGTTTGAT
E1	Body 5	GAACTGATAGCCCTACCGCCTGCATACATTTGAGGAAAGTTT
F1	Body 6	CGTCAATAGATAAATGGCAAATCAACAGAAATCCTAACATTA
G1	Body 7	CGTTATTGCGGAACGCCCCAGCAGGCGATTGAAAGTTAGAGC
H1	Body 8	TCATTTTAATTTTAATTTAGAAGTATTATAATAGAGAATTGA
A2	Body 9	TTCGACATTCTTTAGGAGCACTAACAACGACTTTAGCCCGAA
B2	Body 10	GGAAGGTCTGGTTTAAAGAAACCACCAGATCCTTTCAAACAA
C2	Body 11	TCATCATGGGTTAGAACCTTCGTATTAAAAGGAGCGCAAGCG
D2	Body 12	GTCCACGTATCTAAAATATTTACATCGGAGTTGCAGGAATTA
E2	Body 13	AATGGAAATTCCTGCCTGGCCCTGAGAGGAGAAACACAGTAA
F2	Body 14	CAGTACCACACCATATCAAAATTATTTGTGAATATAATAACG
G2	Body 15	ATTGCCCCTGATTGGGTTTAACGTCAGACACGTAATCTGAAT
H2	Body 16	GATTCGCTTCACCGATTATCAGATGATGTTATACTAACAGAA
A3	Body 17	ATAAAGAAATTGCACCTGATTGTTTGGAGCAATTCACAGCTG
B3	Body 18	TACGTAGATTTTCACTTTGAATACCAAGACGGGCAATCAATA
C3	Body 19	TATATTAATTAATTTTTTCACCAGTGAGTTACAAAAATTAAT
D3	Body 20	CATCAAGTTGAATTTGCTTCTGTAAATCGTCGCATTTTAACA
E3	Body 21	ATTTCATAAAACAAATCGCGCAGAGGCGGTTTTTCTTCCCTT
F3	Body 22	TGAGTGATTGAAAATGGGCGCCAGGGTGAATTATTAAACAAA
G3	Body 23	AGAATCCATAACCTACCTTTTTTAATGGGATGATGCATTTCA
H3	Body 24	ATTACCTTGCGTATCATAGCGATAGCTTAAAATCAATATATG

Well	Name	Sequence-body1
A4	Body 25	ATATGTACTTCTGACCTAAGCAAAAGAAAAACAGTACATACT
B4	Body 26	ATTTCATAATGCTGAGGTTGGGTTATATAGATTAAGGGGAGA
C4	Body 27	GGCGGTTGAATTTAATGGTTTGAAATACAACGCGCGACGCTG
D4	Body 28	TTAACCTTCAATAGTTAATGAATCGGCCCGACCGTTTAGTTA
E4	Body 29	AGAAGAGCCGGCTTATGCAAATCCAATCATATATTGTGATAA
F4	Body 30	TCGTGCCGTTAAATGAAAACTTTTTCAAGCAAGACTACCTTT
G4	Body 31	ATAAGGCAGCTGCATGAATTTATCAAAATCATAACAAACCTG
H4	Body 32	GTGGTCTGAGAGACAAAGAACGCACAGTAGGGCTTATATAAA
A5	Body 33	AGCCAACGCTCAGAAAGAATAAACACCGAGTCGGGCGACAAA
B5	Body 34	CCAGTAAGTAATTCACTGCCCGCTTTCCGAATCATAGTATAA
C5	Body 35	AGGTAAATAAGAGAAATTGAGAATCGCCTCTTACCAATTACT
D5	Body 36	CAACATGTTTCATATGCGTTATACAAATATATTTATTTCGAG
E5	Body 37	AGAAAAATGCGCTCTGTCCAGACGACGAGAGGCATACAACGC
F5	Body 38	TTCAGCTAGCATGTAGAAAATTTAGGCACAATAAACACATTA
G5	Body 39	ATTGCGTGCCTGTTTAGTATCATCGTAGGCTAACTCAACATG
H5	Body 40	ATTTACGAATGCAGTGCCTAATGAGTGAGAATCATCAAGCCG
A6	Body 41	TTTTTATTACCAATCAATAATCGGCTGTGAACAAGTACCGCG
B6	Body 42	TGTAAAGGCAAGCAACCGCACTCATCGACTTTCCTCATCCTA
C6	Body 43	CCCAATACCTGGGGAACGCGCCTGTTTAAATATCCTATCATT
D6	Body 44	CCAAGAACGGGTATTGAACAAGAAAAATTCAACAACATAAAG
E6	Body 45	CTATTAAACCAAGTAATCAGATATAGAACCGGAAGTAGATAA
F6	Body 46	GTTATTATTTATCCACACAACATACGAGGGCTTATTTAGTTG
G6	Body 47	GCCTTAACAATTTTGTTACAAAATAAACAGCCACCTTTGCAC
H6	Body 48	CCAGCTAATCAAGACCGGTATTCTAAGACAATTCCCAATCCA
A7	Body 49	AGCCTAAAACGATTTTGTTATCCGCTCAACGCGAGTTTTGAA
B7	Body 50	AATAAGATTTGCCAATCCTGAATCTTACCGGGAGGGCGTTTT
C7	Body 51	AGCGAACTGTGAAATTTTGTTTAACGTCGAGCGTCTTTCCAG
D7	Body 52	GTAATTGCAATAGCTATCTCCCGACTTGCAACGCTAACGAGG
E7	Body 53	GAAATAGAGCGCTACCTGAACAAAGTCAAAAAATGATAGCTG
F7	Body 54	TTTCCTGCTTACCGAAGCCCTTTTTAAGCATGGTCAAAATAG
G7	Body 55	AATTAACTACAGAGCTCGAATTCGTAATAAAAGTAAAACAAT
H7	Body 56	CAGCCTTTGAACACATATCAGAGAGATAGAGCAAGAGCAGAT
A8	Body 57	CCCCGGGCAAAGTTAAGCCCAATAATAAACCCACAACGGGAG
B8	Body 58	AGCCGAATACCGAGAGAATAACATAAAAACAGGTGTGAGGAT
C8	Body 59	TAGAAGCGCATTAGAGAATTGAGGTAGAAAATACAAAATTCA
D8	Body 60	ATGTTAGCAAACTTACCAGAAGGAAACCTCACAGTGTTTACC
E8	Body 61	TCACAATAAGACAAGTCCGTGAGCCTCCGAGGAAAACGCAGT
F8	Body 62	AGCGCCACAATAGATACATAAAGGTGGCCCTTATTCGCAATA
G8	Body 63	ACGCAAACTAACTGGCATGATTAAGACTAACATATTATTTTG
H8	Body 64	ATAACGGTCTTCGCAAGGGCGACATTCAATAAGTTAAAAGAA

Well	Name	Sequence-body1
A9	Body 65	GGAAGGTAGCAAAATCACCCACCACGGAACCGATTGCACGCG
B9	Body 66	TGCCTGTAATACCCAAAAGTTAGCGTCATCTGCCAGAGGGAG
C9	Body 67	TAGAGCCAAATATTTCATACCGGGGGTTGACTGTAAGAATCA
D9	Body 68	AGTTTGCGAAGTAGCACCATTACCATTATAGCGACGCGCGTT
E9	Body 69	GGCCGTTGCATTTTAGCACCGTAATCAGGCAAGGCTGGGAAT
F9	Body 70	TTCATCGTTCACGGGACGGAAATTATTCAGCCATTCGGAAAC
G9	Body 71	GTCACCAATGAACCCCGTCACCGACTTGATTAAAGTGCGGCG
H9	Body 72	AAACCATCGATAGCCGGTCATAGCCCCCGCCAGAAGTGAATT
A10	Body 73	ATATTGGCCTTGATTCTGTGGTGCTGCGTTATTAGCCCTCAG
B10	Body 74	CCTCAGACACCACCGGTTGAGGCAGGTCAGACGCAGCCACCC
C10	Body 75	TCAGAGCGCCGCCACGTTTGCCATCTTTTGTGCACATTCACA
D10	Body 76	CAGCATTAAATCCTTGTCACTGCGCGCCTCATAATCCGCCTC
E10	Body 77	AACAAATGACAGGACTCAGAGCCGCCACACCGGAACAAAATC
F10	Body 78	ACCGGAAAGCGCAGCATTAAAGCCAGAACACAGAGCCGCCGC
G10	Body 79	GCCTTGAAAGAGGCTGAGAAGAGCCACCCAGAACCACCACGT
H10	Body 80	AAGTATTGTAACAGAGTTTTAACGGGGTTGGAAAGGCATCAG
A11	Body 81	ACGATCCCCCTCCTCAAGAGAAGGATTAGCCCCCTCGCAGTC
B11	Body 82	GTGTACTTTACCGTCCAGCGGTGCCGGTGGATTAGAACATGA
C11	Body 83	TCTGAATGGTAATATGCCCGTATAAACAATTCTGACGGGGTT
D11	Body 84	CGGGTTAGTACCAGTTTCGGAACCTATTGTTAATGTACAGGA
E11	Body 85	TTGCTCACCTGCAGTCCAGTAAGCGTCATACATGTCAGATGC
F11	Body 86	TCGGCTTTTGATGACCCCCTGCCCCGCCACCCTCACTGAGTT
G11	Body 87	CCACCCTCAGAATAGCGGATAAGTGCCGACGGCATCACCAGT
H11	Body 88	CATGTACACAACGCTCAGCAAATCGTTATCGAGAGAGTACCG
A12	Body 89	ACAAACTCGTAACAGAACCGCCACCCTCGAGGTTTGGTTGAT
B12	Body 90	CATTTTCCCGGTGTATCACCGTACTCAGAGAGCCAAGGAACC
C12	Body 91	ATAAGTAGGTGTGTCTGTAGCATTCCACGCCCAATCCACCCT
D12	Body 92	GTTAGCGTTCAACAGTTTCGGATAGCAAAGACAGCACATCCC
E12	Body 93	TTACACTTAGCCCGGAATATTTAATTGTGTCATAACCTCATA
F12	Body 94	AACAACTTAACGATAGGTTTCTTTGCTCATCGGTTGGCTCCA
G12	Body 95	AAAGGAGAGAGCGGAGTGAGAATAGAAAAAAAAAATATCAGC
H12	Body 96	CTGGTAACGAGGTGGTTGAAAATCTCCAGGAACAATTTGCTA

TABLE B.2: 6HB staple sequence - body2

Well	Name	Sequence-body2
A1	Body2 1	TTGCTTTTGGGTAACTAAAGTTTTGTCGATGGGATCTAAAGG
B1	Body2 2	AATTGCGAATAAGGAATGAATTTTCTGTTCTTTCCCCTGCGG
C1	Body2 3	AATAATTTTTTCACAATTTCTTAAACAGCTGTTGCAGACGTT
D1	Body2 4	AGTTCATGAGGAAGTATGAGCCGGGTCACTTGATAGGAGTTA
E1	Body2 5	GCTGAGGTCGTCACTTTGAGGACTAAAGACTTTTACCGCTTT
F1	Body2 6	TGCGGGACTTGCAGCCGATAGTTGCGCCGTTGCGGTTTCCAT
G1	Body2 7	ACGGCTAGTAAAATATCCGCCGGGCGCGGACAATGTTCGGTC
H1	Body2 8	TAAACGGCAGAGGCCCTCAGCAGCGAAACGATATAACAACAA
A2	Body2 9	CCATCGCGCACTCAACGTAATGCCACTAAAACGAGGGTAGCA
B2	Body2 10	GAGATTTGTCAATCATAAGACGCATAACGACAGCATCGGACG
C2	Body2 11	GCAGACGGTATCATGCGAAACAAAGTACCGAAGGCTTGCAGG
D2	Body2 12	CGCTTTCCCGGAACCGAACTGACCAACTGGGGTCAACCAACC
E2	Body2 13	CGATTATAAAGAGGTGTCCAGCATCAGCTTGAAAGACGAGGC
F2	Body2 14	TAAAACGACCAAGCCGCCTGATAAATTGAGCCGGAAGGACAG
G2	Body2 15	CTTACGGGTGTACAGCTCCATGTTACTTTGTCGAACCCCCAG
H2	Body2 16	ATGAACGCTGGAGGCAAAAGAATACACTAAAACCCCAACCAG
A3	Body2 17	TAACTCATCTTTGAATCCGCGACTTCAGTGAATAATGTGAAT
B3	Body2 18	CAAAGCTGCTCACTGACCAGGCGCATAGTCCCACGTTATGCG
C3	Body2 19	TCAACTTGAACTGGCGTCGGTGGTGCCAGCTGGCTAACGTAA
D3	Body2 20	ATTTTAATAATCATGGCTTGCCCTGACGCCAAATCGACCTTC
E3	Body2 21	GAGTAGTATAGAACCGGATATTCATTACAGAAACATTTAATT
F3	Body2 22	ATCAAGAGCAGCACCTCATTATACCAGTGAGATGGCCAGAAC
G3	Body2 23	GAAAAATCCACATTCAACTATTGGGCTTCAGGACGCAAGAAT
H3	Body2 24	GCCAACGGTAATCTTGACAAGCGAGAGGGCAACCGTTGGGAA
A4	Body2 25	AGGAATACTACGTTTGGTCTGGTCAGCACTTTTGCCGATAAA
B4	Body2 26	AACCAAAAAAATGCAGATACATAACGCCCAGACGAAAAAGAA
C4	Body2 27	CGTCAGCCAGAGGGTAACCCTCGTTTACAAAAGGAGAGATTT
D4	Body2 28	GTTTTGCGTGGTGCAATAAAACGAACTAATCAGTTATTACGA
E4	Body2 29	GGCATAGTAAGAATAGGTAGAAAGATTCACGGAACTGTAGAA
F4	Body2 30	GAGCAACACTATCAGGTAATAGTAAAATCCGGACTAACATTA
G4	Body2 31	TTCTTCAAATATCGCATAACGGAACGTGGTTTAGAAAAACGA
H4	Body2 32	TTTAAACAATCAGGTAAGAGGAAGCCCGAAAGAACGACCATA
A5	Body2 33	AATCAAAAGTTCAGCTGGATAGCGTCCAACATCCTCGTTTTA
B5	Body2 34	TGCATCACTTCAAACCTCCGGCCAGAGCATACTGCCAAATGC
C5	Body2 35	ATTCGAGAAAAGATTCTTTACCCTGACTTCCCCCTGGAATCG
D5	Body2 36	TCATAAACTGGCAGGCGAACCAGACCGGAAAGCAAAGCGGAT
E5	Body2 37	TAATGCTCAATTCTGCGAATTCATTGAAATTATAGTCAGATA
F5	Body2 38	TGATTCCGTAGCTCGAGCTTAATTGCTGAAGCAAATTTTCGT
G5	Body2 39	CTCGTCGTACGAGTAGATTTAGTTTGACGTCCGTTCTCCAAC
H5	Body2 40	TTGCGGAGATTAGATTCCGGCAAACGCGCATTAGATAACAGT

Well	Name	Sequence-body2
A6	Body2 41	AGGTCAGTGGCTTAAACATGTTTTAAATTTCCATATACATTT
B6	Body2 42	GATGCTGGGTCAATGTCTGGAAGTTTCAATGCAACGTCATTT
C6	Body2 43	CGCAAATATTGCCGGAGTACCTTTAATTGCTCCTTGTTAAAC
D6	Body2 44	CTTTTTGATAAGAGTAAAGTACGACAGGCAAGGCATGTAATA
E6	Body2 45	CCAATAAATCATGTAACCTGTTTAGCTAGGGTAAATGCGGGA
F6	Body2 46	AAACATTTTATTTCCCTTTAGTGATGAATATTTTCTTAACAT
G6	Body2 47	GAAGCCTATGACCCAAGAATTAGCAAAAAGTAGCAATTTGGG
H6	Body2 48	CTCAGAGGGCATCAATTCTACTAATAGTTTAAGCAGTACCAA
A7	Body2 49	GCGCGAGCAGGCGGAACGCAAGGATAAAATCGGTTATAAAGC
B7	Body2 50	TCATATACCATCAATATGATAAAGCTAAAATTTTTTAAAAAA
C7	Body2 51	AGCCGCACTGAAAAGGTGGAGCAAACAAAATCCCGAGAACCC
D7	Body2 52	CAAATCATTTTAAACATCGACATAAAAAGAGAATCTTGCCTG
A11	Edge Left 1	TTTTTGCGGTCACGCTGACCATCACCCAAATCAAGTTTTTT
B11	Edge Left 2	TTTTTGAAAGCCGGCGAACGTTTTAGAGCTTGACGGGTTTTT
C11	Edge Left 3	CCCCCGAGGCGAGATAGGGCGCTGGCAAGTGTATTTTT
A12	Edge Right 1	TTTTTCCAGCTGGCGAAAGGGGGATGTGCTGTCGGTGC
B12	Edge Right 2	TTTTTTACAGCGCCATGTTTAAACAATCGGCGAAACGTTTTT
C12	Edge Right 3	CATCGTACAGTATCGGGCCTCTTCGCTATTACGTTTTT
D12	Edge Right 4	TTTTTTTTGAGGGGACGACGAACCGTGCATCTGCCAGTTTTT

TABLE B.3: 6HB staple sequence - active handle - left

Well	Name	Sequence-active handle
A1	Handles Left 1	TTTTTTTTTTGGGGTCGAGGTGCCGTAAAGCTACGTGACGCGTAATTTTTATGCGGCCTTCGTCG
B1	Handles Left 2	CCACCACCGGGCGCAAGGAAGGGAAGAAATCCCTAAAGGGAGTTTTTATGCGGCCTTCGTCG
C1	Handles Left 3	ATGCGCCCTAAACAGGAGGCGAAAGGAGACCCGCCGGGCGATTTTTTATGCGGCCTTCGTCG
D1	Handles Left 4	GGCCCACACTAAATCGGAACACGCAAATTCTATCAGCGCTTATTTTTATGCGGCCTTCGTCG
E1	Handles Left 5	GCGGGAGGCTACAGAGGGCGAAAAACCGTAACCGTAAAAGAGTTTTTATGCGGCCTTCGTCG
F1	Handles Left 6	GACTCCATTTGATTTAATCAGTGAGGCCACAGGAAAATCAGATTTTTATGCGGCCTTCGTCG
G1	Handles Left 7	TGTAGCAATACTTCACGTCAAGGCGCGTTTTTTATGCGGCCTTCGTCG
H1	Handles Left 8	CCTGATGATAACGTGCTTTCCTTGCTTTGAACGTGTTTTTATGCGGCCTTCGTCG
A2	Handles Left 9	CAGAAGTGTTTTTAAGTAATAACATCACTATTAAAGACGAGCTTTTTATGCGGCCTTCGTCG
B2	Handles Left 10	ACCTGGCCAACAGAGAACAAGAGTCCACTTGCCTGAAACGCTTTTTTATGCGGCCTTCGTCG
C2	Handles Left 11	CATTGCATTGACGCCAGTAATAAAAGGGACATTGTGAAATACTTTTTATGCGGCCTTCGTCG
D2	Handles Left 12	CTACATTACAGGAAAGTAGAAGAACTCACAGTTTGGATAGAATTTTTATGCGGCCTTCGTCG
E2	Handles Left 13	ACCAGTCGACCTGAGTTGAGTGTTGTTCAACTATCCGCCAGCTTTTTATGCGGCCTTCGTCG
F2	Handles Left 14	CCCTTCTACACGACTCAATCGTCTGAAAATATTACGGCCTTGTTTTTATGCGGCCTTCGTCG
G2	Handles Left 15	CTGGTAAAGATAGGAAGCGTAAGAATACAGATTGGCAGATTCTTTTTATGCGGCCTTCGTCG
H2	Handles Left 16	GAAGATATCTAAAGCATCATCCAGAACATGGATTATTTACCATTTTTATGCGGCCTTCGTCG
A3	Handles Left 17	TGAAAAAAAACAGACCGAACGAACCACCGTGGCACAAAAGAATTTTTATGCGGCCTTCGTCG
B3	Handles Left 18	TAGCCCGTACCTTGCTGAACCTCAAATAATAAATCAGACAATTTTTTATGCGGCCTTCGTCG
C3	Handles Left 19	CGCCATTAATGGCTCGGCAAAATCCCTTTCAAACCCAGCAAATTTTTATGCGGCCTTCGTCG
D3	Handles Left 20	ATTTTTGAAAAATAGGTGAGGCGGTCAGGAGCCAGCTCAATCTTTTTATGCGGCCTTCGTCG

TABLE B.4: 6HB staple sequence - active handle - right

Well	Name	Sequence-active handle
A7	Handles Right 1	AGAGTCTCATATTCAACCGTTCTAGCTGCAGGTCAGATGAACTTTTTCCCGGGTTGGCCAGG
B7	Handles Right 2	TGGGCGGGTAAAACTCTACAAAGGCTATATAAATTAGACAGTTTTTTCCCGGGTTGGCCAGG
C7	Handles Right 3	GGTAATCTTGTGTATGCAATGCCTGAGTAGGCCGGAATGCCGTTTTTCCCGGGTTGGCCAGG
D7	Handles Right 4	GAGAGGGTAGCTAACAAAAGGGTGAGAAAATGTGTCAGCAGTTTTTTCCCGGGTTGGCCAGG
E7	Handles Right 5	AAATTTTTGAGAGATAGCATGTCAATCATTGCCGCAGGTAAATTTTTCCCGGGTTGGCCAGG
F7	Handles Right 6	GATCATCAACATTAAAATTTCTGCTCATTATGTACTTTTGTTTTTTTCCCGGGTTGGCCAGG
G7	Handles Right 7	TGTAAACTTGTTAAGCCTTCCTGTAGCCAGCTTTTTTCGCATTTTTTCCCGGGTTGGCCAGG
H7	Handles Right 8	TAAATTTGTTAATACCCGGTTGATAATCCAAACTTAATGTGATTTTTCCCGGGTTGGCCAGG
A8	Handles Right 9	ATAATTCACAACCCCAGAAACAGCGGATAGAAAAGTTTAAATTTTTTCCCGGGTTGGCCAGG
B8	Handles Right 10	GCGAGTAGCGTCTGATCAGCTCATTTTTGCAAATACCCCAAATTTTTCCCGGGTTGGCCAGG
C8	Handles Right 11	AACAGGAAGAGACGGTCGGATTCTCCGTACACGCCATCAAAATTTTTCCCGGGTTGGCCAGG
D8	Handles Right 12	GGCAAAGGACGTTGTAAAAATTGTATAATAACCAATAGGACATTTTTCCCGGGTTGGCCAGG
E8	Handles Right 13	CAGTCACCGCCATTTTCTGGTGCCGGAAGGGAACAGCTCTCATTTTTCCCGGGTTGGCCAGG
F8	Handles Right 14	CGGAAAAAGCGACGGCCAGTGCCAAGCTAGGGATAAACGGCGTTTTTTCCCGGGTTGGCCAGG
G8	Handles Right 15	CTTTCCGCGTAATGTTTCTCCGTGGTGATTCAGAGGTTTTCCTTTTTCCCGGGTTGGCCAGG
H8	Handles Right 16	GATTGACGCACCGCCGCCATTCAGGCTGCGCCAGGGTGGAGCTTTTTCCCGGGTTGGCCAGG
A9	Handles Right 17	TGTGAGAGGAACGGATTAAGTTGGGTAACGCAACTCAGCCAGTTTTTCCCGGGTTGGCCAGG
B9	Handles Right 18	CGCCACGGATAGACGGATAGGTCACGTTCGCACTCGTTGGGATTTTTCCCGGGTTGGCCAGG
C9	Handles Right 19	GGCCTCAGGAAGATGGTGTAGCGGAATTTTTTTCCCGGGTTGGCCAGG
D9	Handles Right 20	AGGGCGACAAGGCGATAACCTCACCGGACCAGTCCATGGGCGTTTTTCCCGGGTTGGCCAGG

TABLE B.5: 6HB staple sequence - passive handle - left

Well	Name	Sequence-passive handle
A1	Passive Handles Left 1	TTTTTTTTTTGGGGTCGAGGTGCCGTAAAGCTACGTGACGCGTAA
B1	Passive Handles Left 2	CCACCACCGGGCGCAAGGAAGGGAAGAAATCCCTAAAGGGAG
C1	Passive Handles Left 3	ATGCGCCCTAAACAGGAGGCGAAAGGAGACCCGCCGGGCGAT
D1	Passive Handles Left 4	GGCCCACACTAAATCGGAACACGCAAATTCTATCAGCGCTTA
E1	Passive Handles Left 5	GCGGGAGGCTACAGAGGGCGAAAAACCGTAACCGTAAAAGAG
F1	Passive Handles Left 6	GACTCCATTTGATTTAATCAGTGAGGCCACAGGAAAATCAGA
G1	Passive Handles Left 7	TGTAGCAATACTTCACGTCAAGGCGCGT
H1	Passive Handles Left 8	CCTGATGATAACGTGCTTTCCTTGCTTTGAACGTG
A2	Passive Handles Left 9	CAGAAGTGTTTTTAAGTAATAACATCACTATTAAAGACGAGC
B2	Passive Handles Left 10	ACCTGGCCAACAGAGAACAAGAGTCCACTTGCCTGAAACGCT
C2	Passive Handles Left 11	CATTGCATTGACGCCAGTAATAAAAGGGACATTGTGAAATAC
D2	Passive Handles Left 12	CTACATTACAGGAAAGTAGAAGAACTCACAGTTTGGATAGAA
E2	Passive Handles Left 13	ACCAGTCGACCTGAGTTGAGTGTTGTTCAACTATCCGCCAGC
F2	Passive Handles Left 14	CCCTTCTACACGACTCAATCGTCTGAAAATATTACGGCCTTG
G2	Passive Handles Left 15	CTGGTAAAGATAGGAAGCGTAAGAATACAGATTGGCAGATTC
H2	Passive Handles Left 16	GAAGATATCTAAAGCATCATCCAGAACATGGATTATTTACCA
A3	Passive Handles Left 17	TGAAAAAAAACAGACCGAACGAACCACCGTGGCACAAAAGAA
B3	Passive Handles Left 18	TAGCCCGTACCTTGCTGAACCTCAAATAATAAATCAGACAAT
C3	Passive Handles Left 19	CGCCATTAATGGCTCGGCAAAATCCCTTTCAAACCCAGCAAA
D3	Passive Handles Left 20	ATTTTTGAAAAATAGGTGAGGCGGTCAGGAGCCAGCTCAATC

TABLE B.6: 6HB staple sequence - passive handle - right

Well	Name	Sequence-passive handle
A7	Passive Handles Right 20	AGAGTCTCATATTCAACCGTTCTAGCTGCAGGTCAGATGAAC
B7	Passive Handles Right 19	TGGGCGGGTAAAACTCTACAAAGGCTATATAAATTAGACAGT
C7	Passive Handles Right 18	GGTAATCTTGTGTATGCAATGCCTGAGTAGGCCGGAATGCCG
D7	Passive Handles Right 17	GAGAGGGTAGCTAACAAAAGGGTGAGAAAATGTGTCAGCAGT
E7	Passive Handles Right 16	AAATTTTTGAGAGATAGCATGTCAATCATTGCCGCAGGTAAA
F7	Passive Handles Right 15	GATCATCAACATTAAAATTTCTGCTCATTATGTACTTTTGTT
G7	Passive Handles Right 14	TGTAAACTTGTTAAGCCTTCCTGTAGCCAGCTTTTTTCGCAT
H7	Passive Handles Right 13	TAAATTTGTTAATACCCGGTTGATAATCCAAACTTAATGTGA
A8	Passive Handles Right 12	ATAATTCACAACCCCAGAAACAGCGGATAGAAAAGTTTAAAT
B8	Passive Handles Right 11	GCGAGTAGCGTCTGATCAGCTCATTTTTGCAAATACCCCAAA
C8	Passive Handles Right 10	AACAGGAAGAGACGGTCGGATTCTCCGTACACGCCATCAAAA
D8	Passive Handles Right 9	GGCAAAGGACGTTGTAAAAATTGTATAATAACCAATAGGACA
E8	Passive Handles Right 8	CAGTCACCGCCATTTTCTGGTGCCGGAAGGGAACAGCTCTCA
F8	Passive Handles Right 7	CGGAAAAAGCGACGGCCAGTGCCAAGCTAGGGATAAACGGCG
G8	Passive Handles Right 6	CTTTCCGCGTAATGTTTCTCCGTGGTGATTCAGAGGTTTTCC
H8	Passive Handles Right 5	GATTGACGCACCGCCGCCATTCAGGCTGCGCCAGGGTGGAGC
A9	Passive Handles Right 4	TGTGAGAGGAACGGATTAAGTTGGGTAACGCAACTCAGCCAG
B9	Passive Handles Right 3	CGCCACGGATAGACGGATAGGTCACGTTCGCACTCGTTGGGA
C9	Passive Handles Right 2	GGCCTCAGGAAGATGGTGTAGCGGAATT
D9	Passive Handles Right 1	AGGGCGACAAGGCGATAACCTCACCGGACCAGTCCATGGGCG

TABLE B.7: 6HB staple sequence - fluorophore/thiol

Name	**Sequence-fluorophore/thiol-modification**
Fluorophore Left	Alexa488-TTTTTCGACGAAGGCCGCAT
Fluorophore Right	Alexa647-TTTTTCCTGGCCAACCCGGG
Thiol Right	ThioMC6-D/TTTTTCCTGGCCAACCCGGG

TABLE B.8: 24HB staple sequence - body1

Well	**Name**	**Sequence-body1**
A1	Body1 1	TTTTTCGCTATTAATTAATTTTCCTACCATATCAAAATTATTTTTTTT
B1	Body1 2	TTTTTAGACGCTGAGAAGAGTCAATAGTGAGTGAAAACATAGCGATAGCTTAGATTATTTTT
C1	Body1 3	TTTTTGAGACTACCTTTTTAACCTCCGGCTTTTAATTTATCAAAATCATAGGTCTGATTTTT
D1	Body1 4	TTTTTAACAGTACATAAATCATACCTTTTTTAATGGATTTTT
E1	Body1 5	TTTTTGATTATACTTCTGAATTAATCCTGATTGTTTGTTTTT
F1	Body1 6	TTTTTCAAAATTAATTACATTACAAACATCAAGAAAATTTTT
G1	Body1 7	TTTTTTTTAACGTCAGATGAATATACAGTAATTTGCCCGATTGCGTAGATTTTCAGGTTTTT
H1	Body1 8	TTTTTTTTTCAAATATATTTTAGTACATCGGGAGAAACAATAATTTTT
A2	Body1 9	TTTTTATTATTCATTTCAATTAATCGCGCAGAGGCGATTTTT
B2	Body1 10	TTTTTACTATATGTAAATGCTGATGCAAATCATAGAACCCTTAGGTTGGGTTATATATTTTT
C2	Body1 11	TTTTTGCACGTAAAACAGAAATAAAGAAAACTAGAACC
D2	Body1 12	TTTTTCGGATTCGCCTGATTGCTTTGAATGGACCTTTT
E2	Body1 13	TAACCAAGTTACAAACCTGAGCAAAAGCGCAATTC
F2	Body1 14	GCGGAACAAAGAGTGTTATTAATGGCTACTGACCT
G2	Body1 15	ATCAATAAATGGAATTTGAATATATATGTGACACCGCCTGCAAAAATCT
H2	Body1 16	CGGTCAGTATTAAGTCAACGAACCACCA
A3	Body1 17	TGCGCGATTTTTGAATTTTAATAAATCCCAATTTAGAAGTATATTATCA
B3	Body1 18	GAAAGCGAACAGAGCAATTCACCAGTCACTCGTATAAGTTTG
C3	Body1 19	GACCTAAATACATTTGAGGGTAGCACTAACAACTA
D3	Body1 20	AAGGAATATTCCTGTAGACTTTACAACCGCCGTCAATAGATA
E3	Body1 21	TGATGCGCCGCTACGTATAACGTGCTCCCTCAATC
F3	Body1 22	TTCTTTGAACTCAAACCCTAAAGACAATTCGACAA
G3	Body1 23	AATATCACCAGCAGATTATCACGCATTATCATTTTGCAGAAGATAAAGT
H3	Body1 24	ACCGCCATGCTGGTGTAGAAGATTAGTATAACCGTTGTAGCAGAGGCCAACTAAAT
A4	Body1 25	AATACCGCGCTAGGGGCGAACCACTACGTGAACAT
B4	Body1 26	ACCACACTGTAGCGGAGCGGGACCGTGTTGACGCTCAATCGT
C4	Body1 27	TTATAATAGGATTTTAGACAGGAACGGTACGCCTCGCGCTAAACAGGAG
D4	Body1 28	TTGCAACCGGGGAAAGGGAGCCCCCGAT
E4	Body1 29	ATCAGAGCGGGACAGCTTTGACGAGCACAGGGCGCGATGGCCGTGGCGA
F4	Body1 30	TGCCTGAAATATCCAGGCCTCCTCACAGTAATCATGGTCACT
G4	Body1 31	ACAGAATCCTGAGAAAAGAGTCTGTCAG
H4	Body1 32	GAAAGGAAGGGATTCCGTCTAGTCCACTCTGTCGT
A5	Body1 33	TCGCGTCCGTGAAAACGCTCATGGAAGT
B5	Body1 34	TGTAAAGAGTGTTGTTCCAGTTAGCCCGGAATTCG
C5	Body1 35	AAGGCGTGTAGAAAGCGAAAGGTCACGCTGTTGCCCTTCACCCACGCTG
D5	Body1 36	GGCAACAGCTGACGGGGGCGCCAGGGTGCGAAAAAGCCCCAG
E5	Body1 37	ACATCCCTTACAGGCGGCTGGTAATGGGTAAAGGTTTCTTCGCTCACAA
F5	Body1 38	CCGTCGGGAGGTGTTTGCCGCAAAAATCCCGTATG
G5	Body1 39	CACCGGATGCAGCAAAATCCTTCAACGTCAAAGGGGTTTTTCTTTTCGA

Well	Name	Sequence-body1
H5	Body1 40	ATTGTTACGAGCTCAGATAGGGTAAAAA
A6	Body1 41	TAATGAAGGGAAACATTAAAGAACGTGGACTCCAT
B6	Body1 42	GTCGCGTATCATAATGTGGTGCTGCGGCCGGGGGT
C6	Body1 43	TCAATCCGGGGTCAACGGCTGTGGTGCCAGAATGCCAACGGCACGTCAG
D6	Body1 44	TTTCTGCGTTTAAACGATGCTTCGTCTC
E6	Body1 45	GCCAGCAGTCGGCATCAGATGCCGGGTT
F6	Body1 46	CTGTTTATCACTGCGCGCCTGAGACGATAAAGTGA
G6	Body1 47	ACCTGCAACCTGGTGTGTTCACAGGCGGCCTTTCA
H6	Body1 48	GGACTTGGATGGCAGCCTCCGGCCAGAGCACATGACGCGGTC
A7	Body1 49	AAAAAGCCGTTTTTGATTGCCGGATCAATGGGCGGCCAGCTTTTGCAGGCGGAAGA
B7	Body1 50	AATTTGTGAGAGGTATCGGCGGGAACAATCAACAT
C7	Body1 51	GCCCTCATAACGGACTGGTCTGGTCAGGAAACAGCGTTCCGG
D7	Body1 52	CAGGCCAGTGCCAAGCTTTCAGAGGTATAACCAGTCACGACGTTGTAAAACGACAA
E7	Body1 53	ATGTTTAATACCCGTCGGATTCTCCGTGAAACGTA
F7	Body1 54	TATCGGCCTCAGCTCCAACCGTGCATCT
G7	Body1 55	TCGCACTGGAAACCAGGCAAATTATAGACTTTCTCCGTGGTGTGGTGCC
H7	Body1 56	TAAATGTTCCTGTAAGTTAACCAATAGGGGAACGGCAGCGCC
A8	Body1 57	CAAGAGACAATCATGTAGCATGAGGAGCCGCCACG
B8	Body1 58	TGAGTAATGTGTACTGTTGGGCGCCAGCCTCACGG
C8	Body1 59	GGCTGCGCCGCTTCAAGGGATAGTACCAGTCCCGGGCCAGTTTGAGGGC
D8	Body1 60	TATAAGCAGGCAAATAACATCCAATAAATAAAACTAGCATGT
E8	Body1 61	AGCCTTTGACCCTGAAATCGGAAGCCAATTAAAATTCGCATT
F8	Body1 62	TATTTTTTACTAATAGATATTTTCATTT
G8	Body1 63	CAGTATATTGTACCTAGCAAAACCTGTTTAGCTCTTGGGATAAAAATTT
H8	Body1 64	AAAAGGGTGAGAAGTTAAATGCAATGCCTTAGAACGTCAATA
A9	Body1 65	GAGAGGGGGATCAATATGATATTCAACCGTTCTGATCAAGGCCGGAGAC
B9	Body1 66	CAAGCTGATAAATTCTACAAAGGCTAAAAGGAAAA
C9	Body1 67	CAGGAAGTTGATAATCAGAAAAGTTTACCAGACGAAAAAGAAGTTTTCG
D9	Body1 68	ATTAAGCAATAAAGCCTCAGGACATTTCGATTCCCATTATAG
E9	Body1 69	CAGTAGGGAGAGCATAAAGCTTAATACTTTAACTCCAACAGGTTGATAA
F9	Body1 70	CTGGATACATTGAAGGAAGTTTCATTCCAACTAAACTTTTGC
G9	Body1 71	AAATGTTCGAGAGGGTACGGTTGAATATAATGCTG
H9	Body1 72	AGACCGGAAGCATGTAAAATATCGCGTTATTAGATTCATTTT
A10	Body1 73	ATAGGCTAACCGGAAATGCCAAAAAGAATACACCT
B10	Body1 74	TCCCTGACGAGAAAGGTTTAATTTCAGA
C10	Body1 75	TTTAACAGATTTAGGAATACCAGGAATTTAATTGC
D10	Body1 76	GCGGATTCCTGACTAATTCTGCGAACGAGTAGAGT
E10	Body1 77	CGCCATATTTAATTGGCTTAGACTTTAGTTTGACCTTAATTCGAGCTGG
F10	Body1 78	GTAAAATAGGAAACAAAGTACTGTCGAAATCCGCC
G10	Body1 79	TTCAGTGCAAATCATGACAAGGGCTGACGGTGTACAGACCAGGAACCGA
H10	Body1 80	GGCATAGATTATACCAGTCAGGACGTTGGGAAGTTACATGCGATTTTAA
A11	Body1 81	GTGAATTACCTTCAATTGGGCTTGAGATCACCAGAAAGAGGCCTACGAA
B11	Body1 82	TTTAGGCGTAGAAAGATTCATGGAACAAGTGCGAT
C11	Body1 83	TGGGAACGAGGCGCAACTTTGAAAGAAAGAGGAAG
D11	Body1 84	CAATCATTACGACCTGCTCCATGTTACTTAGCCCTCGCCTGA
E11	Body1 85	AGTAAATGAATTAGGTGTAACGATCTAAAGACAGCATCGGCT
F11	Body1 86	CTACAACCACTGAGTTTCGTCCAGGGAT
G11	Body1 87	GGCACCAGTAATCTACGTAACAATTCTGTATGGGAAGTGAGA
H11	Body1 88	GAGGACTCGCCCACGCATACCCAGATACCGATAGTTGCGCCGACAATAT
A12	Body1 89	CATGTAATAAATTGAACGGAGATTTGTATCGACAACAACCATAAAGACT
B12	Body1 90	AGCAAGCAGCCACCACCCGCCACCCTCAGGTCGCTGGGATCG
C12	Body1 91	TGCGAATAACAGTTACAGAGGGTCTCAGCAGCGAAAGTTTTG
D12	Body1 92	TTTTCATGCCACCCTCAGATAATTTTTTAAGGAGC
E12	Body1 93	GGATTAGTTCTGAACCCCTGCCTATTTC
F12	Body1 94	TTTTAACGGGGTCAGAGTGTACTGGTAA
G12	Body1 95	ATAGGTGAGCGGGGCCAGTAGCAACCGA
H12	Body1 96	AATATAAACAGAATATTACCAGTTTACCAGCGCTTCTCCATC

TABLE B.9: 24HB staple sequence - body2

Well	Name	Sequence-body2
A1	Body2 1	AAGCGCAATTAAAGCTCAAAGACAAAAG
B1	Body2 2	AGAGCCACCACCCTCCTCCCTCAGAGCC
C1	Body2 3	GTAAAGTGCAGCACCGTAATCAGTAGCGAGTACCGGCCCGGA
D1	Body2 4	GCCAGAATTACAGGAGGTTGAGGCAGGTCAGACGACACCACCAGAGCCGGGCGACA
E1	Body2 5	GACGGAACGACTTGTTAATGCACATGAAAGTATTAAGAGGCATACCGTATAAACAG
F1	Body2 6	GAGTAACAGTGCCCACATGGCTTTTGATCGTTCCAAAATATTTTCAACC
G1	Body2 7	AATCAAATCATATGTTAGCAAGGCCGGA
H1	Body2 8	ATCGATAAATTCTGGAGAGGGTTGATATAGGCGGA
A2	Body2 9	GATTGAGCCAGAACTTGGCCTTGTTATCCTGAATCAAACAGCCATATCA
B2	Body2 10	CCAGCTACAATTATTCCCTCCCGACTTGGTATGTTAGCAAAGAAACGCA
C2	Body2 11	GCCCCCTTTAGCGTCAGACTGTAGCGCGTTTTCTA
D2	Body2 12	GGATCGGCATTTTCGAACCAGAGCCAGATTGTCACCCAATGA
E2	Body2 13	ATAGCAAATCGTAGGAATCATAGAACGGGTATTAATCTTTCCCGTGAAC
F2	Body2 14	GACGACACAAGAAACAATGCCATTGAGCGCTAATAGAACAAA
G2	Body2 15	ATAATATTCAATAATCGGCTGACCAAGTTATTTTCGCAAATC
H2	Body2 16	AAAAATAGCAATAGGGAATAACATACAT
A3	Body2 17	TTTTTAGAAACGCAAAGACACCACCTATCTTAGCCGAA
B3	Body2 18	TTTTTAGAATTAACTGAACACCCTTCAGAGAATAAGAG
C3	Body2 19	TTTTTTGATTAAGACTCCTTACCCAAAAGAACTGGCATTTTT
D3	Body2 20	TTTTTCAAGATTAGTTGCTATTTTTGAAGCCTTAAATTTTTT
E3	Body2 21	TTTTTACAAGCAAGCCGTTTTACCGCACTCATCGAGATTTTT
F3	Body2 22	TTTTTAACGTCAAAAATGAAAATAGGGAAGCGCATTAGACGGGTTTTT
G3	Body2 23	ACAAAATTTACCAACGCTAACGAGCGTCTTTCCTTTTT
H3	Body2 24	TTTTTAGAGCCTAATTTGCCAGTTAAAGGTGGCAACATATAAATTTTT
A4	Body2 25	AAAAACAGCAGCCTTCCAAATAAGAAACGATTTTTTGTTTTTTTT
B4	Body2 26	TTTTTCAGAACGCGCCTGTTTACATGTTCAGCTAATGTTTTT
C4	Body2 27	TTTTTAGAAAAGTAAGCAGATACCGAAGCCCTTTTTATTTTT
D4	Body2 28	TTTTTAGCATGTAGAAACCAACCCATCCTAATTTACGTTTTT

TABLE B.10: 24HB staple sequence - active handle - right

Well	Name	Sequence-active handle
A6	Active Handle Right 19	CCCTCAGCCAATAGGAACCAACCTATTAGATCAGAACCGCCATTTTTATTGGAGTGTAGGTA
B6	Active Handle Right 18	TCACCGAGGCATGTACCGTAAGCCTGTAGCATTAGTTTTTATTGGAGTGTAGGTA
C6	Active Handle Right 17	AATTGTACTTAAACAGCTTAGTTTGCCTTATTAGCGTTTGTTTTTTTATTGGAGTGTAGGTA
D6	Active Handle Right 16	TATATTCGAACCGCCACCCTTTATCACCATAAGAGTTTTTATTGGAGTGTAGGTA
E6	Active Handle Right 15	ATTATCACCGTCACATTATTCGTCTCTGCATTAAATTTTTATTGGAGTGTAGGTA
F6	Active Handle Right 14	CCGCCAGCATTGTCAAACCGCCACCCTCTTTTTATTGGAGTGTAGGTA
A7	Active Handle Right 13	GAATTAGAGCCAGCAAAATCATTTTGCTAAGAGAATTTTTATTGGAGTGTAGGTA
B7	Active Handle Right 12	AACAAATAAATCCTAATTTACGATACAGGTGCCTTTTTTTATTGGAGTGTAGGTA
C7	Active Handle Right 11	AACGTCAAATCAATAGAAAATATCACCGGGTCATATTTTTATTGGAGTGTAGGTA
D7	Active Handle Right 10	TCCTGAGACTCCTCCAGTACCAAGTATAACAAAAGTTTTTATTGGAGTGTAGGTA
E7	Active Handle Right 9	AGCCATTTGGGAGGGGAAGGTGTAAGCGATTCACATTTTTATTGGAGTGTAGGTA
F7	Active Handle Right 8	GCTATTTATCCCAATTACAGAGACCACCGGAACCGCAGAGCCTTTTTATTGGAGTGTAGGTA
A8	Active Handle Right 7	AAGAAAACAAAGTTACCAGAAGGAAACCTAAGTGCTTATCATTTTTTATTGGAGTGTAGGTA
B8	Active Handle Right 6	CGCGAGGCGTTTTAGCGAAATGCGCCCATTTTTATTGGAGTGTAGGTA
C8	Active Handle Right 5	GGACGTAGAAAATAGTTTATTATAACATGTCAGAGTTTTTATTGGAGTGTAGGTA
D8	Active Handle Right 4	ATAAACAATCAACAATAGATAAGTCCTCTCCAGACTTTTTATTGGAGTGTAGGTA
E8	Active Handle Right 3	ATAATAACGGAATATTACGCACGGGAGGTTTGCACTTTTTATTGGAGTGTAGGTA
F8	Active Handle Right 2	TTTTTTCCGGTATTCTAAGAAAGATATAGAAGGCTTATTTTTATTGGAGTGTAGGTA
G8	Active Handle Right 1	TTTTTTGAGTTAAGCCCAATAGATAACCCACAAGAATTTTTTATTGGAGTGTAGGTA

TABLE B.11: 24HB staple sequence - passive handle - right

Well	Name	Sequence-passive handle
A10	Passive Right Handle 19	CCCTCAGCCAATAGGAACCAACCTATTAGATCAGAACCGCCA
B10	Passive Right Handle 18	TCACCGAGGCATGTACCGTAAGCCTGTAGCATTAG
C10	Passive Right Handle 17	AATTGTACTTAAACAGCTTAGTTTGCCTTATTAGCGTTTGTT
D10	Passive Right Handle 16	TATATTCGAACCGCCACCCTTTATCACCATAAGAG
E10	Passive Right Handle 15	ATTATCACCGTCACATTATTCGTCTCTGCATTAAA
F10	Passive Right Handle 14	CCGCCAGCATTGTCAAACCGCCACCCTC
A11	Passive Right Handle 13	GAATTAGAGCCAGCAAAATCATTTTGCTAAGAGAA
B11	Passive Right Handle 12	AACAAATAAATCCTAATTTACGATACAGGTGCCTT
C11	Passive Right Handle 11	AACGTCAAATCAATAGAAAATATCACCGGGTCATA
D11	Passive Right Handle 10	TCCTGAGACTCCTCCAGTACCAAGTATAACAAAAG
E11	Passive Right Handle 9	AGCCATTTGGGAGGGGAAGGTGTAAGCGATTCACA
F11	Passive Right Handle 8	GCTATTTATCCCAATTACAGAGACCACCGGAACCGCAGAGCC
A12	Passive Right Handle 7	AAGAAAACAAAGTTACCAGAAGGAAACCTAAGTGCTTATCAT
B12	Passive Right Handle 6	CGCGAGGCGTTTTAGCGAAATGCGCCCA
C12	Passive Right Handle 5	GGACGTAGAAAATAGTTTATTATAACATGTCAGAG
D12	Passive Right Handle 4	ATAAACAATCAACAATAGATAAGTCCTCTCCAGAC
E12	Passive Right Handle 3	ATAATAACGGAATATTACGCACGGGAGGTTTGCAC
F12	Passive Right Handle 2	TTTTTTCCGGTATTCTAAGAAAGATATAGAAGGCTTA
G12	Passive Right Handle 1	TTTTTTGAGTTAAGCCCAATAGATAACCCACAAGAAT

TABLE B.12: 24HB staple sequence - active handle - left

Well	Name	Sequence-active handle
A1	Active Handles Left 1	CTTAGAATGAATAACCTTGCTTCTGTAAATCGTTTTTTAGGAAGAGAATGGTT
B1	Active Handles Left 2	TAATTTCCGCAAGACAAAGAACGCGAGAAAACTTTTTTAGGAAGAGAATGGTT
C1	Active Handles Left 3	TTATCACCTTGCTGGGTCAGTTGGAAGATGATGAATAACAATTTTTTAGGAAGAGAATGGTT
D1	Active Handles Left 4	ATAAAACATCGCCATTAAAAATACCGCTTCTTTAATTTTTAGGAAGAGAATGGTT
E1	Active Handles Left 5	AAAGCCAGGAACCACCAGAAGGATGATGAAATCAAATATCTTTTTTTAGGAAGAGAATGGTT
F1	Active Handles Left 6	ATTTAATGGATTATTTACATTGGCAGATATCTTCTTTTTTAGGAAGAGAATGGTT
G1	Active Handles Left 7	GAGCGGACAAATGAACAGTGCCACGCTGCAACAGAGGTGAGGTTTTTAGGAAGAGAATGGTT
H1	Active Handles Left 8	GAAGGTTATCTAAACAGTTGAAATATCTAACCTCATTTTTAGGAAGAGAATGGTT
A2	Active Handles Left 9	TCTGGCCTAAGAATACGTGTATCGGCCTGCTAAAAGGGACATTTTTTAGGAAGAGAATGGTT
B2	Active Handles Left 13	AAGGTCGAGGTGCCGTAAAGCCCGAGTAAGTGTTTTTTTTAGGAAGAGAATGGTT
C2	Active Handles Left 11	ATAGATTAGAGCGCTGGCAAGCCCGCCCGCGCTTAAGTTTTTAGGAAGAGAATGGTT
D2	Active Handles Left 12	CACGACCAGTAACACTGAAATGGTTTGATTTTTAGGAAGAGAATGGTT
E2	Active Handles Left 10	AGTAAGAACGCACAGACAATAACTGATAGCCCTACTTTTTAGGAAGAGAATGGTT
F2	Active Handles Left 14	TCCATCACCCAAATGCCGATTAAAGGAGAATTCCTCGTTAGATTTTTAGGAAGAGAATGGTT
A3	Active Handles Left 20	AGCGGGGAGAGGCGGTTTGCGTATTGTTGCTGCATTTTTTAGGAAGAGAATGGTT
B3	Active Handles Left 18	TAAATAACGGCGGGCCATACCTACATTTGATAAATTTTTTAGGAAGAGAATGGTT
C3	Active Handles Left 16	CATAGCTGTTTCCTCAACATACGCATCACGCAAATATAACATTTTTTAGGAAGAGAATGGTT
D3	Active Handles Left 19	TTAAATCAAAAGAATTGGAACCCGGAAGTGAGCTATTTTTTAGGAAGAGAATGGTT
E3	Active Handles Left 17	CAAGTTTTTTGGGATCAGGGCGTACTATCGTAACCTTTTTAGGAAGAGAATGGTT
F3	Active Handles Left 15	AAAATCCCTTATAGAGCTTGAAGGAAAACAATATTTTTTTAGGAAGAGAATGGTT
A4	Active Handles Left 21	GATGGTGGTTCCGAAATCGGCTTTCACGCTGTTCTTTTTTAGGAAGAGAATGGTT

Well	Name	Sequence-active handle
B4	Active Handles Left 25	GGGTGCCGCGCTCACTGCCAGCATCAGCGCCGGGCGCGGTTGTTTTTAGGAAGAGAATGGTT
C4	Active Handles Left 23	CAGGCGAAGCGGTCGCCTGGCCCTGAGATAACCAGTGAGACGTTTTTAGGAAGAGAATGGTT
D4	Active Handles Left 24	TTGAGGATCCCCGGCGCGTGCGTCATACCAGAATGGAATAAATTTTTAGGAAGAGAATGGTT
E4	Active Handles Left 22	ACATTAATTGCGTTTAATGAGCATAAAGTTCCACAGTGTGAATTTTTAGGAAGAGAATGGTT
F4	Active Handles Left 26	CCCGCTTTCCAGTCTCGGCCAACGCGCATTTTTAGGAAGAGAATGGTT
A5	Active Handles Left 32	GCAAGCGCCATTCGATCGGTGCGGCAGCAACCGCAATCCCACTTTTTAGGAAGAGAATGGTT
B5	Active Handles Left 30	TTCAGCCAGCGGTGCTGCATCTGCACTCTTACTAGTTTTTAGGAAGAGAATGGTT
C5	Active Handles Left 28	AGCCGCAGCAAATCGTTAAACTCTGCTCGTCATAATTTTTAGGAAGAGAATGGTT
D5	Active Handles Left 31	CCTGCGGTATGAGCCGGGTCACTGTTGCTTCGCACTTTTTAGGAAGAGAATGGTT
E5	Active Handles Left 29	GTACATCGACATAACAGCAGTACTTAAACGTGGTGACGTGCCTTTTTAGGAAGAGAATGGTT
F5	Active Handles Left 27	TGAAGGGTAAAGTTTTGCCCCCCGGTCTTTTTTAGGAAGAGAATGGTT
A6	Active Handles Left 33	ATAACCTCACCGGACCAGCGCGCCAGCTTTTTTAGGAAGAGAATGGTT
B6	Active Handles Left 37	CCAGCCAGCTTTCCTAGGACGACGACAGTTTTTAGGAAGAGAATGGTT
C6	Active Handles Left 35	AAAAAGAGACGCAGCCTCTTCCTGCAAGTTTTTAGGAAGAGAATGGTT
D6	Active Handles Left 36	ATGCGTTATACAAATGTTAAATCAGCTCATTTTTGGTATCATTTTTTAGGAAGAGAATGGTT
E6	Active Handles Left 34	ACCGTAATGGGATAGTGTAGATGGGCGCATCGTTGCGGATTGTTTTTAGGAAGAGAATGGTT
F6	Active Handles Left 38	TTAAGTTGGGTAACGGATGTGGCTATTAAAGGGCGCCATTCATTTTTAGGAAGAGAATGGTT
A7	Active Handles Left 44	AGTCAAATCACCCACAAGGTAAAGATTCTTTTTAGGAAGAGAATGGTT
B7	Active Handles Left 42	AACGCCATCAAATGAAATTTTTTCTTACTTTTTAGGAAGAGAATGGTT
C7	Active Handles Left 40	ATCGATGCTGAGAGTCTGGAGCACGTTGGGTCAAATTTTTAGGAAGAGAATGGTT
D7	Active Handles Left 43	GGTGGCATCAATTCGAGAGATAATGCCGTTTTTAGGAAGAGAATGGTT
E7	Active Handles Left 41	GAAAGGGGCCAGGGTTTTCAAACATTATATTTCAACGCAAGCTTTTTAGGAAGAGAATGGTT
F7	Active Handles Left 39	CTGGCCTGAGCGAGTAACAGTACCCCGGATAATAATTCGCGTTTTTTAGGAAGAGAATGGTT
A8	Active Handles Left 45	TAGCTCAACATGATACAGGCAAAATATTCCAAAAATTTTTAGGAAGAGAATGGTT
B8	Active Handles Left 49	TCTTTTAAATATGCATATAACTCGTCATAACAGTTTTTTTAGGAAGAGAATGGTT
C8	Active Handles Left 47	GGGGCGCGAGCTTTGCAAATGCCTCATACGGGAGATTTTTAGGAAGAGAATGGTT
D8	Active Handles Left 48	GCTTAATACTAATGCAGTTAATATTTTGCGCTCAATTTTTAGGAAGAGAATGGTT
E8	Active Handles Left 46	ATGCCAGAGGGGGTATACTGCGGTCAGGTCATTGCAACGGTATTTTTAGGAAGAGAATGGTT
F8	Active Handles Left 50	GCTTAAGAGGAAGCCCGAAAGACTTCTTAAGCAAATTTTTAGGAAGAGAATGGTT
A9	Active Handles Left 56	TATCAGGTCTTTACGCATCAAAAAGAGCTTTTTAGGAAGAGAATGGTT
B9	Active Handles Left 54	CGATAAAAACCAAATAAGAGCCGCCAAAACATTCATGAGAATTTTTTAGGAAGAGAATGGTT
C9	Active Handles Left 52	AAACGAGAATGACCTGCTTTAAAATATTGCGTCCAAATAGTATTTTTAGGAAGAGAATGGTT
D9	Active Handles Left 55	CCTCAAAATAAATCAAAAATTCATTACCAATAAGGCTTGCCCTTTTTAGGAAGAGAATGGTT
E9	Active Handles Left 53	TGCGGATGCTCCTTTCAGGATTAGAGAGAATCAAAGCGAACCTTTTTAGGAAGAGAATGGTT
F9	Active Handles Left 51	TCATAACCCTCGCCTAAATTGTAAACGATACATAAAACACTATTTTTAGGAAGAGAATGGTT
A10	Active Handles Left 57	TATACCAAGCGCCTACAAACGTAATAGATTTTTAGGAAGAGAATGGTT
B10	Active Handles Left 61	CTTTGACCCCCATAAAAACGAACGAGTACTGCTCATTTTTAGGAAGAGAATGGTT
C10	Active Handles Left 59	TTTCCATTAAACGGACTGACCAGACGGTTTTTTAGGAAGAGAATGGTT
D10	Active Handles Left 60	TTAAAAATCTACGTAACTAACCAGTTGAACGCCAATTTTTAGGAAGAGAATGGTT
E10	Active Handles Left 58	GTTAAAACACTCATGAACTGGCTCATAGTAACTTTAATCATTTTTTTAGGAAGAGAATGGTT
F10	Active Handles Left 62	AAAAGGAACAACTAAAAATCTCCGGACAGATGAACCTTCATCTTTTTAGGAAGAGAATGGTT
A11	Active Handles Left 68	TTCGAGGTGAATTTTCGGTTTGCTCCAACACGTTGAAGGAATTTTTTAGGAAGAGAATGGTT
B11	Active Handles Left 66	TTTTCGAGCCAGTAGTACTCAGGAGGTTTAGTAAGAGAGGCATTTTTAGGAAGAGAATGGTT
C11	Active Handles Left 64	TCGTCGATACCACAGACAGCCCTCATAGTTAGCAAGTACAAATTTTTAGGAAGAGAATGGTT
D11	Active Handles Left 67	AACGGCTTCAGCGGTTTTGCTAAACAACTGTTTCCAGACGTTTTTTTAGGAAGAGAATGGTT
E11	Active Handles Left 65	ATAGAGAACAACGAGGGTAGCTTTTCATAAAAAAGATCAGCTTTTTTAGGAAGAGAATGGTT
F11	Active Handles Left 63	AAGGCCGCTTTTGCGAGGCTTGCAGGGACATTATTACCCTCATTTTTAGGAAGAGAATGGTT

TABLE B.13: 24HB staple sequence - passive handle - left

Well	Name	Sequence-passive handle
A1	Passive Left Handle 1	CTTAGAATGAATAACCTTGCTTCTGTAAATCGT
B1	Passive Left Handle 2	TAATTTCCGCAAGACAAAGAACGCGAGAAAACT
C1	Passive Left Handle 3	TTATCACCTTGCTGGGTCAGTTGGAAGATGATGAATAACAAT
D1	Passive Left Handle 4	ATAAAACATCGCCATTAAAAATACCGCTTCTTTAA
E1	Passive Left Handle 5	AAAGCCAGGAACCACCAGAAGGATGATGAAATCAAATATCTT
F1	Passive Left Handle 6	ATTTAATGGATTATTTACATTGGCAGATATCTTCT
G1	Passive Left Handle 7	GAGCGGACAAATGAACAGTGCCACGCTGCAACAGAGGTGAGG
H1	Passive Left Handle 8	GAAGGTTATCTAAACAGTTGAAATATCTAACCTCA
A2	Passive Left Handle 9	TCTGGCCTAAGAATACGTGTATCGGCCTGCTAAAAGGGACAT
B2	Passive Left Handle 13	AAGGTCGAGGTGCCGTAAAGCCCGAGTAAGTGTTT
C2	Passive Left Handle 11	ATAGATTAGAGCGCTGGCAAGCCGCCGCGCTTAAG
D2	Passive Left Handle 12	CACGACCAGTAACACTGAAATGGTTTGA
E2	Passive Left Handle 10	AGTAAGAACGCACAGACAATAACTGATAGCCCTAC
F2	Passive Left Handle 14	TCCATCACCCAAATGCCGATTAAAGGAGAATTCCTCGTTAGA
A3	Passive Left Handle 20	AGCGGGGAGAGGCGGTTTGCGTATTGTTGCTGCAT
B3	Passive Left Handle 18	TAAATAACGGCGGGCCATACCTACATTTGATAAAT
C3	Passive Left Handle 16	CATAGCTGTTTCCTCAACATACGCATCACGCAAATATAACAT
D3	Passive Left Handle 19	TTAAATCAAAAGAATTGGAACCCGGAAGTGAGCTA
E3	Passive Left Handle 17	CAAGTTTTTTGGGATCAGGGCGTACTATCGTAACC
F3	Passive Left Handle 15	AAAATCCCTTATAGAGCTTGAAGGAAAACAATATT
A4	Passive Left Handle 21	GATGGTGGTTCCGAAATCGGCTTTCACGCTGTTCT
B4	Passive Left Handle 25	GGGTGCCGCGCTCACTGCCAGCATCAGCGCCGGGCGCGGTTG
C4	Passive Left Handle 23	CAGGCGAAGCGGTCGCCTGGCCCTGAGATAACCAGTGAGACG
D4	Passive Left Handle 24	TTGAGGATCCCCGGCGCGTGCGTCATACCAGAATGGAATAAA
E4	Passive Left Handle 22	ACATTAATTGCGTTTAATGAGCATAAAGTTCCACAGTGTGAA
F4	Passive Left Handle 26	CCCGCTTTCCAGTCTCGGCCAACGCGCA
A5	Passive Left Handle 32	GCAAGCGCCATTCGATCGGTGCGGCAGCAACCGCAATCCCAC
B5	Passive Left Handle 30	TTCAGCCAGCGGTGCTGCATCTGCACTCTTACTAG
C5	Passive Left Handle 28	AGCCGCAGCAAATCGTTAAACTCTGCTCGTCATAA
D5	Passive Left Handle 31	CCTGCGGTATGAGCCGGGTCACTGTTGCTTCGCAC
E5	Passive Left Handle 29	GTACATCGACATAACAGCAGTACTTAAACGTGGTGACGTGCC
F5	Passive Left Handle 27	TGAAGGGTAAAGTTTTGCCCCCCGGTCT
A6	Passive Left Handle 33	ATAACCTCACCGGACCAGCGCGCCAGCT
B6	Passive Left Handle 37	CCAGCCAGCTTTCCTAGGACGACGACAG
C6	Passive Left Handle 35	AAAAAGAGACGCAGCCTCTTCCTGCAAG
D6	Passive Left Handle 36	ATGCGTTATACAAATGTTAAATCAGCTCATTTTTGGTATCAT
E6	Passive Left Handle 34	ACCGTAATGGGATAGTGTAGATGGGCGCATCGTTGCGGATTG
F6	Passive Left Handle 38	TTAAGTTGGGTAACGGATGTGGCTATTAAAGGGCGCCATTCA
A7	Passive Left Handle 44	AGTCAAATCACCCACAAGGTAAAGATTC
B7	Passive Left Handle 42	AACGCCATCAAATGAAATTTTTTCTTAC
C7	Passive Left Handle 40	ATCGATGCTGAGAGTCTGGAGCACGTTGGGTCAAA
D7	Passive Left Handle 43	GGTGGCATCAATTCGAGAGATAATGCCG
E7	Passive Left Handle 41	GAAAGGGGCCAGGGTTTTCAAACATTATATTTCAACGCAAGC
F7	Passive Left Handle 39	CTGGCCTGAGCGAGTAACAGTACCCCGGATAATAATTCGCGT
A8	Passive Left Handle 45	TAGCTCAACATGATACAGGCAAAATATTCCAAAAA
B8	Passive Left Handle 49	TCTTTTAAATATGCATATAACTCGTCATAACAGTT
C8	Passive Left Handle 47	GGGGCGCGAGCTTTGCAAATGCCTCATACGGGAGA
D8	Passive Left Handle 48	GCTTAATACTAATGCAGTTAATATTTTGCGCTCAA
E8	Passive Left Handle 46	ATGCCAGAGGGGGTATACTGCGGTCAGGTCATTGCAACGGTA
F8	Passive Left Handle 50	GCTTAAGAGGAAGCCCGAAAGACTTCTTAAGCAAA

Well	Name	Sequence-passive handle
A9	Passive Left Handle 56	TATCAGGTCTTTACGCATCAAAAAGAGC
B9	Passive Left Handle 54	CGATAAAAACCAAATAAGAGCCGCCAAAACATTCATGAGAAT
C9	Passive Left Handle 52	AAACGAGAATGACCTGCTTTAAAATATTGCGTCCAAATAGTA
D9	Passive Left Handle 55	CCTCAAAATAAATCAAAAATTCATTACCAATAAGGCTTGCCC
E9	Passive Left Handle 53	TGCGGATGCTCCTTTCAGGATTAGAGAGAATCAAAGCGAACC
F9	Passive Left Handle 51	TCATAACCCTCGCCTAAATTGTAAACGATACATAAAACACTA
A10	Passive Left Handle 57	TATACCAAGCGCCTACAAACGTAATAGA
B10	Passive Left Handle 61	CTTTGACCCCCATAAAAACGAACGAGTACTGCTCA
C10	Passive Left Handle 59	TTTCCATTAAACGGACTGACCAGACGGT
D10	Passive Left Handle 60	TTAAAAATCTACGTAACTAACCAGTTGAACGCCAA
E10	Passive Left Handle 58	GTTAAAACACTCATGAACTGGCTCATAGTAACTTTAATCATT
F10	Passive Left Handle 62	AAAAGGAACAACTAAAAATCTCCGGACAGATGAACCTTCATC
A11	Passive Left Handle 68	TTCGAGGTGAATTTTCGGTTTGCTCCAACACGTTGAAGGAAT
B11	Passive Left Handle 66	TTTTCGAGCCAGTAGTACTCAGGAGGTTTAGTAAGAGAGGCA
C11	Passive Left Handle 64	TCGTCGATACCACAGACAGCCCTCATAGTTAGCAAGTACAAA
D11	Passive Left Handle 67	AACGGCTTCAGCGGTTTTGCTAAACAACTGTTTCCAGACGTT
E11	Passive Left Handle 65	ATAGAGAACAACGAGGGTAGCTTTTCATAAAAAAGATCAGCT
F11	Passive Left Handle 63	AAGGCCGCTTTTGCGAGGCTTGCAGGGACATTATTACCCTCA

TABLE B.14: 24HB staple sequence - fluorophore/thiol

Name	Sequence-fluorophore/thiol-modification
Fluorophore Right	Alexa488-TTTTTTACCTACACTCCAAT
Fluorophore Left	Alexa647-TTTTTAACCATTCTCTTCCT
Thiol Left	ThioMC6-D/TTTTTAACCATTCTCTTCCT

Appendix C

Protocols and MATLAB code for Single molecule tracking

C.1 Fiji/ImageJ: Particle Tracker 2D/3D

Open and adjust Images/videos:

1. Drag the .nd2 file into Fiji;

2. Click OK for the first pop-up window (Bio-Formats Import Options) (For most of the usual cases, don't have to change the selections);

3. Close the second pop-up window (Original Metadata – File name), or keep it for information check, eg. exposure time, timestamp information...;

4. Wait for the image lookup window to show up;

5. If image shows totally black, adjust the brightness:

Image > adjust > Brightness/Contrast... Usually click 'Auto', then 'Apply' should be fine; if not, adjust manually.

Set the right pixel/micron ratio:

6. Analyze > Set Scale: usually 9.375 pixels/micron for our microscope setup (60X objective and a 2.5X extra magnification in the CCD camera); Check 'Global',

click 'OK'.

Particle tracking: (The most time-consuming part)

7. Plugins > Mosaic > Particle Tracking 2D/3D;

8. Find the optimal parameters for particle detection and linking and tracking, use 'Preview Detected' to preview the detection: Usually, Radius: 3-5; Per/Abs: 0.01-0.05; Link Range: 4; Displacement: 4-7; Dynamics: Brownian; (Refer to the attached paper for more information about the tracking parameters)

9. Click 'OK', wait for All Trajectories Visual window and Results window to show up.

Collect and save trajectory information:

10. In the All Trajectories Visual window, go through the entire video, check if most of the trajectories of moving particles are well recognized; if not, go back to Step 9, adjust the parameters and start over again;

11. If good, go to the Results window,

12. Click Save Full Report to save all parameter settings and motion information for this video detection;

13. Click All Trajectories to Table, double click > Save as > XXX_#.csv file (for MATLAB MSD Analysis later);

14. Click All MSS/MSD to Table; (At the first time, there might be a pop-up window warning about dimension unit > click OK > change Unit of length from "micron" to "um" > check Global > click OK);

15. If Reset Results Table window pop up, click OK; > double click > Save as > MSD_XXX_#.csv file.

For detailed tutorial, please refer to:

https://mosaic.mpi-cbg.de/MosaicToolboxSuite/ParticleTracker.html

C.2 MATLAB: Trajectory filtration and MSD analysis

There are two sets of code for Trajectory filtration and MSD analysis:

- PlotLogScaleMSDForUnknownDiffGeneral.m

- PlotLogScaleMSDForBrownianDiffGeneral.m

Code provided here (modified based on @msdanalyzer [45]):

https://github.com/Mengqiqqe/SingleParticleTracking.git

The only difference between these two codes is the filtration condition for filter out/recognize good trajectories. In UnknownDiff, $\langle(\Delta r_i)^2\rangle = 4D_{\text{general}}t^{\alpha}$, $\log(\langle(\Delta r_i)^2\rangle)$ and $\log(t)$ are fitted to a linear line, defining $R^2 > 0.9$ as good enough trajectory. For BrownianDiff, $\langle(\Delta r_i)^2\rangle = 4D_{\text{linear}}t$, $\langle(\Delta r_i)^2\rangle$ and t are fitted to a linear line, also with $R^2 > 0.9$ as good enough trajectory. In both methods, you can get Dgeneral, Dlinear and anomalous exponent α for each good trajectory that is filtered out.

1. Open "PlotLogScaleMSDForUnknown/BrownianDiffGeneral.m" in MATLAB;

2. Collect all raw data files (XXX_30ms_#.csv) in one folder and duplicate (always keep one as backup for other analysis maybe in the future);

3. Open the folder in MATLAB as Current Folder shown on the left hand side;

4. Change the initial settings:

- concentration (change this according to the file name)

- frame_interval (get this by subtracting two continuous timestamp)

- video (give video # range)

- remove (to remove # that are missing)

- clip_factor (usually set as 0.25, only fit the first one quarter of the MSD plot)

- Mini_Trajlength (define the mini trajectory length to rule out those short trajectories)

5. Click Run (green button on top);

6. Wait to get: (Files will be automatically generated and saved under the Current Folder selected.)

- MSD data for each individual good trajectory:

concentration_video#_MSDdata_Traj#.xlsx;

- All information (D_{general}, D_{linear}, α, R^2 etc.) for all good trajectories under this concentration:

AllDcollections_(un)brownian_Traj>miniTrajlenght_concentration.xlsx;

- A log scale MSD plot for all good trajectories:

concentration_logScale_MSD ALL.png).

C.3 Other codes used for MTT and Spot-On analysis

Some other codes used for MTT algorithm and Spot-On analysis (modified based on ref [63], [62]):

https://github.com/Mengqiqqe/SingleParticleTracking.git

Appendix D

Protocols for enzyme and DNA origami experiments

D.1 Enzyme experiments

D.1.1 Enzyme fluorescent dye labeling

Materials

Enzymes: Urease from Jack Bean (TCI), Aldolase from Rabbit Muscle (sigma); Alexa Fluor™ 647 Protein Labeling Kit

Protocols

1. Weigh 2-5 mg enzyme (powder).
2. Dissolve in 1 mL 1$\times$ PBS buffer completely.
3. Add 100 μL of 1 M bicarbonate to the enzyme solution and mix well. (Note: Bicarbonate, pH 8.3, is added to raise the pH of the reaction mixture, since TFP and succinimidyl esters react efficiently at alkaline pH.)
4. Measure the pH (should be around 8 $\sim$ 8.5).

5. Allow a vial of reactive dye to warm to room temperature. Transfer the protein solution from step 3 to the vial of reactive dye. This vial contains a magnetic stir bar. Cap the vial and invert a few times to fully dissolve the dye.

6. Stir the reaction mixture for 2 hour at room temperature or keep at 4 °C overnight.

7. Protein purification

    - Prepare a 0.5 mL, 40K MWCO, Zeba Spin Desalting Column (Thermo Scientific) by breaking off the bottom plug and placing the column into a 2 mL collection tube.
    - Centrifuge the column at 1000 × g for 2 minutes, discard the storage buffer and return column to the same collection tube.
    - Place a mark on the side of the column where the compacted resin is slanted upward. Place column in centrifuge with the mark facing outward in all subsequent centrifugation steps.
    - Equilibrate the column by adding 500 μL of PBS to the top of the resin bed and centrifuging at 1000 × g for 2 minutes. Discard the flow-through and repeat this step a total of 2-3 times.
    - Place column into a new 2 mL collection tube and apply the protein sample directly onto the center of the resin bed. Allow sample to absorb into the resin.
    - Centrifuge the column at 1000 × g for 2 minutes. The collected flow-through solution is the purified protein sample.

8. Determine the Degree of Labeling (Optional)

- Dilute a small amount of the purified conjugate into PBS, usually 1:10 dilution.
- Measure the absorbance in a cuvette with a 1-cm path length at 280 nm (A280) and 650 nm (A650, maximum (λ_{max}) for the AlexaFluor 647, and calculate the degree of labeling.

9. Store the protein solution in 4 °C fridge, protected from light.

(This protocol was modified based on USER GUIDE provided by *ThermoFisher*)

D.1.2 Enzyme fluorescent labeling and biotin modification

Materials

Enzymes: Urease from Jack Bean (TCI), Aldolase from Rabbit Muscle (sigma); EZ-LinkTM Sulfo-NHS-LC-Biotinylation Kit

Protocols

1. Weigh 2-5 mg enzyme (powder).
2. Dissolve in 1 mL 1× PBS buffer completely.
3. Add 100 μL of 1 M bicarbonate to the enzyme solution and mix well. (Note: Bicarbonate, pH 8.3, is added to raise the pH of the reaction mixture, since TFP and succinimidyl esters react efficiently at alkaline pH.)
4. Measure the pH (should be around 8 $\sim$ 8.5).
5. Allow a vial of reactive dye to warm to room temperature. Transfer the protein solution from step 3 to the vial of reactive dye. This vial contains a magnetic stir bar. Cap the vial and invert a few times to fully dissolve the dye.

6. Immediately before use, prepare 10mM Sulfo-NHS-LC-Biotin by dissolving 2.2mg in 400 μl ultrapure water.

7. Add 5 $\sim$ 6 μl 10 mM Sulfo-NHS-LC-Biotin solution (20-fold molar excess) to the protein/dye mixture.

8. Stir the reaction mixture for 2 hour at room temperature or keep at 4 °C overnight.

9. Protein purification

    - Prepare a 0.5 mL, 40K MWCO, Zeba Spin Desalting Column (Thermo Scientific) by breaking off the bottom plug and placing the column into a 2 mL collection tube.
    - Centrifuge the column at 1000 $\times$ g for 2 minutes, discard the storage buffer and return column to the same collection tube.
    - Place a mark on the side of the column where the compacted resin is slanted upward. Place column in centrifuge with the mark facing outward in all subsequent centrifugation steps.
    - Equilibrate the column by adding 500 μL of PBS to the top of the resin bed and centrifuging at 1000 $\times$ g for 2 minutes. Discard the flow-through and repeat this step a total of 2-3 times.
    - Place column into a new 2 mL collection tube and apply the protein sample directly onto the center of the resin bed. Allow sample to absorb into the resin.
    - Centrifuge the column at 1000 $\times$ g for 2 minutes. The collected flow-through solution is the purified protein sample.

10. Determine the Degree of Labeling (Optional)

    - Dilute a small amount of the purified conjugate into PBS, usually 1:10 dilution.
    - Measure the absorbance in a cuvette with a 1-cm path length at 280 nm (A280) and 650 nm (A650, maximum (λ_{max}) for the AlexaFluor 647, and calculate the degree of labeling ($\epsilon_{urease} = 75592\,M^{-1}cm^{-1}$, $\epsilon_{aldolase} = 150080\,M^{-1}cm^{-1}$).

11. Store the protein solution in 4 °C fridge, protected from light.

(This protocol was modified based on USER GUIDE provided by *ThermoFisher*)

D.2 DNA origami experiments

D.2.1 PEG purification

Materials

Precipitation buffer (15% PEG 8000 (w/v), 1x TE, 505 mM NaCl), DNA folded solution 50 uL

Protocols

1. Mix every 50 uL of the folded solution with 50 uL precipitation buffer. (Adjust [$MgCl_2$] so the final concentration of magnesium is over 10 mM)
2. Centrifuge at RT, 4500 rcf for 30 min. (Mark the expected pellet position)
3. Carefully remove the supernatant.
4. Elute using 50 uL of 1× FoB5.

5. Leave for over 24h (over 3h at RT or 30 min in 30-40°C rotating incubator).

6. To remove PEG and concentrate, filter with Amicon 100K filter.

7. Use Nanodrop to estimate the concentration

D.2.2 Gel purification

Materials

agarose, 10x TBE, 1.375 M $MgCl_2$, SYBR safe, folded solution 50 uL

Protocols

1. Make agarose solutions and gel buffers

    - Agarose solution: 1.5 g agarose, 95 mL DI water, 5 mL 10x TBE (1.5w%);
    - Running buffers: 475 mL DI water, 25 mL 10x TBE, 2 mL 1.375M $MgCl_2$ (for final concentration of 5.5mM)

2. Microwave agarose solutions at high for 2 minutes

3. Slightly shake and cool using water poured in another container

    - Add 400 uL of $MgCl_2$ 1.375M
    - Add 10 uL of SYBR Safe 10,000x
    - After a couple of minutes, take out and shake until you have a homogenous solution

4. Place the cassette and the comb (pink, or white) and slowly pour in the agarose solution

5. Remove the bubbles using pipette tips

6. Wait for 30 min
7. Holding the two sides, carefully take the comb out, wash the comb thoroughly
8. Rotate the gel 90 degrees (watch out for the side!)
9. Immerse the gel in buffer. First, pour the buffer on top of the gel, so that the wells are covered with the buffer. Don't overfill
10. Mix 50 uL of the sample and 10uL of the 6x loading dye (or 100ul for white well) Pipette sample into the well
11. Move to the cold room and run it in 90V for 2 hours
12. Put plastic wrap on the UV illumination plate with light source underneath. Place the gel on it. The DNA bands should look bright.
13. Wash the razor blade with 70% ethanol and cut out the band with folded DNA.
14. Slice the gel band into small pieces or use pestle to crush them in an eppendorf tube. Place the gel pieces inside Freeze and Squeeze tube.
15. Freeze at -20°C for 5 min.
16. Centrifuge at 10,000 g for 5 min, throw out anything above the filter. The solution should be around 20 uL.
17. Check the concentration of the solution using Nanodrop. (Should be around 1-5 nM, 10 ng/uL = 2 nM)

(Protocols in this section were provided by Daichi Hayakawa)

D.3 Fluorescent labeling of DNA six-helix bundle

Materials

DNA 6HB folded solution 100 ul, Alexa488/Alexa647 modified DNA strands

Protocols

1. Adjust the magnesium concentration of the DNA folded solution to 15mM with 1M $MgCl_2$
2. Add two-fold molar excess of Alexa488 (left)/Alexa647 (right) modified DNA anti-handle strands (complimentary to the DNA handle strands on each side, two anti-handle strands per handle on 6HB)
3. Incubate at 30°C for 30 min
4. PEG purification to remove free unattached fluorophore modified DNA oligos
5. Check the concentration of fluorescent labeled 6HB using Nanodrop.
6. Store at 4°C and protect from light, should be good for 2 weeks

D.4 Conjugation of urease on DNA six-helix bundle

D.4.1 DNA oligos modification of fluorescent labeled enzymes

Materials

Alexa647 labeled urease 100 ul, Thiol-modified DNA anti-handle strands, Amicon Ultra-0.5 filter device (100K NMWL), PBS-Mg15 buffer (normal PBS buffer with 15 mM $MgCl_2$)

Protocols

1. Add 3-fold molar excess of thiol-modified DNA strands to 100 ul Alexa647 labeled urease solution (usually $\sim$ 3 mg/ml).

2. Incubate at 4°C for at least 72hr

3. Remove the free unconjugated thiol-modified DNA strands by three times ultrafiltration with PBS buffer and restore the DNA-modified Alexa647-urease filtrate in 50 ul PBS-Mg15 buffer (The 15 mM magnesium was added to facilitate the conjugation between enzyme and DNA 6HB later).

4. Check DNA-modified Alexa647-urease concentration with Nanodrop (usually 2 $\sim$ 3 mg/ml)

5. Store at 4°C and protect from light, should be good for $\sim$ 3 days

D.4.2 Conjugation of DNA-modified Alexa647-urease to Alexa488 labeled DNA six-helix bundle

Materials

DNA-modified Alexa647-urease 50 ul in PBS-Mg15 buffer, Alexa488 labeled 6HB 10 ul, 8% precipitation buffer (8% PEG 8000 (w/v), 1x TE, 505 mM NaCl)

Protocols

1. Add ten-fold molar excess of DNA-modified Alexa647-urease to 10 ul Alexa488 labeled 6HB (usually $\sim$ 25 nM) (Ten DNA-modified Alexa647-ureases per handle on 6HB)

2. Incubate at RT for 2hr or 30°C for 30min

3. Remove the free unconjugated ureases by PEG purification with 8% precipitation buffer

- Build up the total volume of enzyme and DNA 6HB mixture to 100 ul with 1× FoB20
- Add 100 ul 8% precipitation buffer and mix well
- Centrifuge at 4500 rcf at RT for 30 min
- Remove the supernatant carefully
- Redissolve the enzyme conjugated DNA 6HB pellet in 10 ul PBS-Mg15 buffer by incubate at RT for 2 hr

4. Keep the enzyme conjugated DNA 6HB on ice and use immediately after making for further experiments

Bibliography

1. Tyska, M. J. & Warshaw, D. M. The myosin power stroke. *Cell Motility* **51,** 1–15 (2002).

2. Tsao, D. S. & Diehl, M. R. Molecular motors: Myosins move ahead of the pack. *Nat. Nanotech.* **9,** 9–10 (2014).

3. Hancock, W. O. Bidirectional cargo transport: moving beyond tug of war. *Nat. Rev. Mol. Cell Biol.* **15,** 615–628 (2014).

4. Ma, X. *et al.* Enzyme-Powered Hollow Mesoporous Janus Nanomotors. *Nano Letters* **15,** 7043–7050. ISSN: 15306992 (2015).

5. Ma, X., Hortelao, A. C., Miguel-López, A. & Sánchez, S. Bubble-Free Propulsion of Ultrasmall Tubular Nanojets Powered by Biocatalytic Reactions. *Journal of the American Chemical Society* **138.** PMID: 27718566, 13782–13785. eprint: https://doi.org/10.1021/jacs.6b06857. https://doi.org/10.1021/jacs.6b06857 (2016).

6. Muddana, H. S., Sengupta, S., Mallouk, T. E., Sen, A. & Butler, P. J. Substrate Catalysis Enhances Single-Enzyme Diffusion. *JACS Comm.* **132,** 2110–2111 (2010).

7. Sengupta, S. *et al.* Enzyme Molecules as Nanomotors. *J. Am. Chem. Soc.* **135,** 1406–1414 (2013).

8. Sengupta, S. *et al.* DNA polymerase as a molecular motor and pump. *ACS Nano* **8,** 2410–2418. ISSN: 1936086X (2014).

9. Zhao, X. *et al.* Substrate-driven chemotactic assembly in an enzyme cascade. *Nat. Chem.* **10,** 311–317 (2018).

10. Börsch, M. *et al.* Conformational changes of the H+-ATPase from Escherichia coli upon nucleotide binding detected by single molecule fluorescence. *FEBS Lett.* **437,** 251–254 (1998).

11. Riedel, C. *et al.* The heat released during catalytic turnover enhances the diffusion of an enzyme. *Nature (London)* **517,** 227–230 (2015).

12. Jee, A.-Y., Dutta, S., Cho, Y.-K., Tlusty, T. & Granick, S. Enzyme leaps fuel antichemotaxis. *Proc. Natl. Acad. Sci. U.S.A.* **115,** 14–18. ISSN: 0027-8424 (2018).

13. Xu, M., Ross, J. L., Valdez, L. & Sen, A. Direct Single Molecule Imaging of Enhanced Enzyme Diffusion. *Phys. Rev. Lett.* **123,** 128101 (12 Sept. 2019).

14. Illien, P., Adeleke-Larodo, T. & Golestanian, R. Diffusion of an enzyme: The role of fluctuation-induced hydrodynamic coupling. *Epl* **119.** ISSN: 12864854 (2017).

15. Jee, A.-Y., Tlusty, T. & Granick, S. Master curve of boosted diffusion for 10 catalytic enzymes. *Proc. Natl. Acad. Sci. U.S.A.* **117,** 29435–29441. ISSN: 0027-8424 (2020).

16. Günther, J. P., Börsch, M. & Fischer, P. Diffusion Measurements of Swimming Enzymes with Fluorescence Correlation Spectroscopy. *Accounts of Chemical Research* **51,** 1911–1920. ISSN: 15204898 (2018).

17. Cécile, F. *Fluorescence Correlation Spectoscopy* https://physics.mcmaster.ca/~biophys/molbiophys/FCS.html.

18. Zhang, Y., Armstrong, M. J., Bassir Kazeruni, N. M. & Hess, H. Aldolase Does Not Show Enhanced Diffusion in Dynamic Light Scattering Experiments. *Nano Lett.* **18,** 8025–8029 (2018).

19. Günther, J.-P., Majer, G. & Fischer, P. Absolute diffusion measurements of active enzyme solutions by NMR. *J. Chem. Phys.* **150,** 124201 (2019).

20. Jee, A.-Y., Chen, K., Tlusty, T., Zhao, J. & Granick, S. Enhanced Diffusion and Oligomeric Enzyme Dissociation. *J. Am. Chem. Soc.* **141,** 20062–20068 (2019).

21. Chen, Z. *et al.* Single-molecule diffusometry reveals no catalysis-induced diffusion enhancement of alkaline phosphatase as proposed by FCS experiments. *Proc. Natl. Acad. Sci. U.S.A.* **117,** 21328–21335. ISSN: 0027-8424 (2020).

22. Rothemund, P. W. K. Folding DNA to create nanoscale shapes and patterns. *Nature* **440,** 297–302. https://doi.org/10.1038/nature04586 (2006).

23. Douglas, S. M. *et al.* Self-assembly of DNA into nanoscale three-dimensional shapes. *Nature* **459,** 414–418. ISSN: 1476-4687. https://doi.org/10.1038/nature08016 (7245 2009).

24. Han, D. *et al.* DNA Origami with Complex Curvatures in Three-Dimensional Space. *Science* **332,** 342–346. eprint: https://www.science.org/doi/pdf/10.1126/science.1202998. https://www.science.org/doi/abs/10.1126/science.1202998 (2011).

25. Benson, E. *et al.* DNA rendering of polyhedral meshes at the nanoscale. *Nature* **523,** 441–444. ISSN: 1476-4687. https://doi.org/10.1038/nature14586 (7561 2015).

26. Gigadalton-scale shape-programmable DNA assemblies. *Nature* **552,** 78–83. ISSN: 1476-4687. https://doi.org/10.1038/nature24651 (7683 2017).

27. Han, D. *et al.* Single-stranded DNA and RNA origami. *Science* **358,** eaao2648 (2017).

28. Andersen, E. S. *et al.* Self-assembly of a nanoscale DNA box with a controllable lid. *Nature* **459,** 73–76 (2009).

29. Gerling, T., Wagenbauer, K. F., Neuner, A. M. & Dietz, H. Dynamic DNA devices and assemblies formed by shape-complementary, non–base pairing 3D components. *Science* **347,** 1446–1452. eprint: https://www.science.org/doi/pdf/10.1126/science.aaa5372. https://www.science.org/doi/abs/10.1126/science.aaa5372 (2015).

30. Dey, S. *et al.* DNA origami. *Nature Reviews Methods Primers* **1.** https://doi.org/10.1038/s43586-020-00009-8 (2021).

31. Castro, C. E. *et al.* A primer to scaffolded DNA origami. *Nature Methods* **8,** 221–229. ISSN: 1548-7105. https://doi.org/10.1038/nmeth.1570 (3 2011).

32. Wagenbauer, K. F. *et al.* How We Make DNA Origami. *ChemBioChem* **18,** 1873–1885. eprint: https://chemistry-europe.onlinelibrary.wiley.com/doi/pdf/10.1002/cbic.201700377. https://chemistry-europe.onlinelibrary.wiley.com/doi/abs/10.1002/cbic.201700377 (2017).

33. Guo, M. *et al.* Probing the stochastic, motor-driven properties of the cytoplasm using force spectrum microscopy. *Cell* **158,** 822–832. ISSN: 10974172. http://dx.doi.org/10.1016/j.cell.2014.06.051 (2014).

34. Parry, B. R. *et al.* The bacterial cytoplasm has glass-like properties and is fluidized by metabolic activity. *Cell* **156,** 183–194. ISSN: 00928674. http://dx.doi.org/10.1016/j.cell.2013.11.028 (2014).

35. Patiño, T. *et al.* Influence of Enzyme Quantity and Distribution on the Self-Propulsion of Non-Janus Urease-Powered Micromotors. *Journal of the American Chemical Society* **140,** 7896–7903. ISSN: 15205126 (2018).

36. Dey, K. K. *et al.* Micromotors Powered by Enzyme Catalysis. *Nano Letters* **15,** 8311–8315. ISSN: 15306992 (2015).

37. Yu, H., Jo, K., Kounovsky, K. L., Pablo, J. J. D. & Schwartz, D. C. Molecular propulsion: Chemical sensing and chemotaxis of DNA driven by RNA polymerase. *Journal of the American Chemical Society* **131,** 5722–5723. ISSN: 00027863 (2009).

38. Riedel, C. *et al.* The heat released during catalytic turnover enhances the diffusion of an enzyme. *Nature* **517,** 227 (2015).

39. Illien, P. *et al.* Exothermicity Is Not a Necessary Condition for Enhanced Diffusion of Enzymes. *Nano Letters* **17,** 4415–4420. ISSN: 15306992 (2017).

40. Bacia, K., Haustein, E. & Schwille, P. Fluorescence correlation spectroscopy: Principles and applications. *Cold Spring Harbor Protocols* **2014,** 709–725 (2014).

41. Kubecka, J., Uhlik, F. & Kosovan, P. View Issue Mean squared displacement from fluorescence correlation spectroscopy. *Soft Matter* **12,** 3760–3769 (2016).

42. Onal Okyay, T. High throughput colorimetric assay for rapid urease activity quantification. *J. Microbiol. Method.* **95,** 324–326 (2013).

43. McAllister, J. W., Schmidt, P. W., Dorfman, K. D., Lodge, T. P. & Bates, F. S. Thermodynamics of Aqueous Methylcellulose Solutions. *Macromolecules* **48,** 7205–7215 (2015).

44. Sbalzarini, I. F. & Koumoutsakos, P. Feature point tracking and trajectory analysis for video imaging in cell biology. *Journal of Structural Biology* **151,** 182–195 (2005).

45. Tarantino, N. *et al.* Tnf and il-1 exhibit distinct ubiquitin requirements for inducing NEMO-IKK supramolecular structures. *J. Cell Bio.* **204,** 231–245. ISSN: 00219525 (2014).

46. Howse, J. R. *et al.* Self-Motile Colloidal Particles: From Directed Propulsion to Random Walk. *Phys. Rev. Lett.* **99,** 048102. https://link.aps.org/doi/10.1103/PhysRevLett.99.048102 (4 July 2007).

47. Tanis, B. R. J. & Naylor, A. W. Physical and Chemical Studies of a Low-Molecular-Weight Form of Urease. *Biochem. J* **108,** 771–777 (1968).

48. Krajewska, B. Ureases I. Functional, catalytic and kinetic properties: A review. *Journal of Molecular Catalysis B: Enzymatic* **59,** 9–21. ISSN: 13811177 (2009).

49. Al-Shemmeri, T. *Engineering Fluid Mechanics* (Bookboon, 2012).

50. Golestanian, R. Enhanced Diffusion of Enzymes that Catalyze Exothermic Reactions. *Phys. Rev. Lett.* **115,** 108102. https://link.aps.org/doi/10.1103/PhysRevLett.115.108102 (10 Sept. 2015).

51. Mikhailov, A. S. & Kapral, R. Hydrodynamic collective effects of active protein machines in solution and lipid bilayers. *Proceedings of the National Academy of Sciences* **112,** E3639–E3644. ISSN: 0027-8424. http://www.pnas.org/content/112/28/E3639 (2015).

52. Balasubramanian, A. & Ponnuraj, K. Crystal Structure of the First Plant Urease from Jack Bean : 83 Years of Journey from Its First Crystal to Molecular Structure †. *Journal of Molecular Biology* **400,** 274–283. ISSN: 0022-2836. http://dx.doi.org/10.1016/j.jmb.2010.05.009 (2010).

53. Ross, J. L., Wallace, K., Shuman, H., Goldman, Y. E. & Holzbaur, E. L. Processive bidirectional motion of dynein-dynactin complexes in vitro. *Nature Cell Biology* **8,** 562–570. ISSN: 14657392 (2006).

54. Conway, L., Wood, D., Tuzel, E. & Ross, J. L. Motor transport of self-assembled cargos in crowded environments. *Proceedings of the National Academy of Sciences* **109,** 20814–20819. ISSN: 0027-8424. http://www.pnas.org/cgi/doi/10.1073/pnas.1209304109 (2012).

55. Han, Y *et al.* Brownian Motion of an Ellipsoid. *Science* **314,** 626–631 (2006).

56. Ribrault, C., Triller, A. & Sekimoto, K. Diffusion trajectory of an asymmetric object: Information overlooked by the mean square displacement. *Phys. Rev. E* **75,** 021112. https://link.aps.org/doi/10.1103/PhysRevE.75.021112 (2 Feb. 2007).

57. Kudalkar, E. M., Deng, Y., Davis, T. N. & Asbury, C. L. Coverslip Cleaning and Functionalization for Total Internal Reflection Fluorescence Microscopy. *Cold Spring Harbor Protoc.,* pdb.prot085548 (2016).

58. Saxton, M. J. Single-particle tracking: the distribution of diffusion coefficients. eng. *Biophys. J* **72,** 1744–1753. ISSN: 0006-3495 (Apr. 1997).

59. Rossier, O. *et al.* Integrins [beta]1 and [beta]3 exhibit distinct dynamic nanoscale organizations inside focal adhesions. *Nat. Cell Biol.* **14,** 1057–1067. ISSN: 14657392 (Oct. 2012).

60. Shuang, B. *et al.* Improved Analysis for Determining Diffusion Coefficients from Short, Single-Molecule Trajectories with Photoblinking. *Langmuir* **29,** 228–234 (2013).

61. Knight, S. C. *et al.* Dynamics of CRISPR-Cas9 genome interrogation in living cells. *Science* **350,** 823–826. ISSN: 0036-8075 (2015).

62. Hansen, A. S. *et al.* Robust model-based analysis of single-particle tracking experiments with Spot-On. *eLife* **7,** e33125 (2018).

63. Sergé, A., Bertaux, N., Rigneault, H. & Marguet, D. Dynamic multiple-target tracing to probe spatiotemporal cartography of cell membranes. *Nat. Method.* **5,** 687–694 (2008).

64. La Verde, V., Dominici, P. & Astegno, A. Determination of Hydrodynamic Radius of Proteins by Size Exclusion Chromatography. *BioProtoc.* **7,** e2230 (8 2017).

65. Hink, M. A. *et al.* Structural Dynamics of Green Fluorescent Protein Alone and Fused with a Single Chain Fv Protein. *J. Biol. Chem.* **275,** 17556–17560 (2000).

66. Cherstvy, A. G., Nagel, O., Beta, C. & Metzler, R. Non-Gaussianity population heterogeneity and transient superdiffusion in the spreading dynamics of amoeboid cells. *Phys. Chem. Chem. Phys.* **20,** 23034–23054 (35 2018).

67. Blattler, D. P., Contaxis, C. C. & Reithel, F. J. Dissociation of Urease by Glycol and Glycerol. *Nature (London)* **216,** 274–275. ISSN: 1476-4687 (1967).

68. Singh, J. K. D., Luu, M. T., Abbas, A. & Wickham, S. F. Switchable DNA-origami nanostructures that respond to their environment and their applications. *Biophysical reviews* **10,** 1283–1293 (2018).

69. Martin, T. G. & Dietz, H. Magnesium-free self-assembly of multi-layer DNA objects. *Nature communications* **3,** 1–6 (2012).

70. Sun, L. *et al.* Real-Time Imaging of Single-Molecule Enzyme Cascade Using a DNA Origami Raft. *Journal of the American Chemical Society* **139.** PMID: 29131610, 17525–17532. eprint: https://doi.org/10.1021/jacs.7b09323. https://doi.org/10.1021/jacs.7b09323 (2017).

71. Douglas, S. M. *et al.* Rapid prototyping of 3D DNA-origami shapes with caDNAno. *Nucleic acids research* **37,** 5001–6. ISSN: 1362-4962 (15 2009).

72. Maffeo, C., Yoo, J. & Aksimentiev, A. De novo reconstruction of DNA origami structures through atomistic molecular dynamics simulation. *Nucleic acids research* **44.** PMID: 26980283, 3013–9 (7 2016).

73. Kick, B., Praetorius, F., Dietz, H. & Weuster-Botz, D. Efficient Production of Single-Stranded Phage DNA as Scaffolds for DNA Origami. *Nano Letters* **15.** PMID: 26028443, 4672–4676. eprint: https://doi.org/10.1021/acs.nanolett.5b01461. https://doi.org/10.1021/acs.nanolett.5b01461 (2015).

74. Kauert, D. J., Kurth, T., Liedl, T. & Seidel, R. Direct Mechanical Measurements Reveal the Material Properties of Three-Dimensional DNA Origami. *Nano Letters* **11.** PMID: 22047401, 5558–5563. eprint: https://doi.org/10.1021/nl203503s. https://doi.org/10.1021/nl203503s (2011).

Mengqi Xu

✉ Syracuse University, 900 South Crouse Ave. Syracuse, NY13244, US
☎ +1-413-313-9267
@ mxu101@syr.edu

Educational Background

2021	**Ph.D. Candidate**, Syracuse University (*transferring with PI*) Biophysics, PhD program of Physics
2019	**Ph.D. Candidate**, University of Massachusetts Amherst Biophysics, PhD program of Physics-*Overall GPA: 3.94/4.00*
2016	**B.S.**, South University of Science and Technology of China (SUSTC) Major I: Biology (09.2013-09.2014) -*Overall GPA: 3.77/4.0, Ranking: Top 3;* Major II: Physics (09.2014-06.2016) -*Overall GPA: 3.8/4.0, Ranking: Top 4;*

Awards & Honors

03/2019	UMASS Soft Materials for Life Sciences National Traineeship Travel Grant Award
07/2016	Outstanding Undergraduate Thesis Award - SUSTC
09/2015	Start-up Scholarship of SUSTC-2015
11/2014	Gold Award of International Genetically Engineered Machine Competition (iGEM)
09/2014	Start-up Scholarship of SUSTC-2014
09/2013	Start-up Scholarship of SUSTC-2013
09/2012	Start-up Scholarship of SUSTC-2012

Publications

M. Xu, L. Valdez, A. Sen, J.L. Ross, "Direct Single Molecule Imaging of Enhanced Enzyme Diffusion", Phys. Rev. Lett. 123, 128101 (2019). *DOI: https://doi.org/10.1103/PhysRevLett.123.128101*

M. Xu, W.B. Rogers, W.W. Ahmed, J.L. Ross, "Comparison of different approaches to single-molecule imaging of enhanced enzyme diffusion", under review at Phys. Rev. E (2021). *https://arxiv.org/abs/2012.15424*

Research Conference Presentations

Mar 2021 *Talk*	**2021 APS March Meeting** "Comparison of different approaches to single particle tracking of enzymes displaying enhanced diffusion".
Oct 2019 *Invited PhD student*	**Symposia on the Physics of Biological Function** ITS @ The Graduate Center of the City University of New York.
Aug 2019 *Poster*	**Gordon Research Conference/Seminars (GRC/GRS)** "Direct single molecule imaging of enhanced enzyme diffusion".
Mar 2019 *Talk*	**2019 APS March Meeting** "Single molecule imaging of nanoscale self-propelled active matter".
Mar 2018 *Talk*	**2018 APS March Meeting** "Enhanced diffusion of molecular catalase".

Professional Skills

Experimental skills:	Protein labeling/purification, DNA origami, Lipid membrane (**Bench-top**) TIRF Microscope, Confocal Microscope, TEM, ARPES, STM (**Imaging**) Particle tracking, Diffusion, Photobleaching (**Data analysis**)
Computer skills:	MATLAB, C, Java, Igor Pro, Material Studio, Origin, LaTeX, LabVIEW (**Physics**) ImageJ, Primer Premier & Oligo (**Biology**)

Research Experiences

01/2019-Present
Research Assistant

Understand the physics of synthetic active materials powered by enzymes using highly programmable DNA origami

Create a new suite of highly programmable enzyme-powered active particles using DNA origami

Advisor: Jennifer Ross, W. Benjamin Rogers (*Brandeis*), Wylie W. Ahmed (*Cal State Fullerton*)

Overview: Enzymes appear to be a promising propulsion source for creating new active materials. Here, we try to make new nano- to micrometer-scale active particles or probes of active matter using highly programmable DNA origami and active enzymes. We realize nanometer-scale particles with complex anisotropic shape and near-atomic-level positioning of molecules using DNA origami. We then couple a precise number of active enzymes to DNA origami at specific locations to serve as the propulsive units and study the mechanisms of propulsion from the bottom up using single-particle imaging techniques.

07/2017-Present
Research Assistant

How autonomous materials harvest energy from a noisy environment, and couple together to engineer emergent biological phenomena

Direct single molecule imaging of active enzymes displaying enhanced diffusion in the presence of the substrates

Advisor: Jennifer Ross, Ayusman Sen (*Penn State*)

Overview: This project aims at investigating the mechanism of how random, non-specific motor (eg. active enzymes) coupling to harvest work from noisy, random systems. Specifically, enzymes have been shown to diffuse faster in the presence of their substrates. We revealed new insights into this emergent enzyme activity using single-particle tracking (SPT) with total internal reflection fluorescence (TIRF) microscopy and study the diffusion characteristics of each individual enzymes. We compared different experimental designs (free/tethered enzymes on polymer brush/supported lipid bilayer (SLB)), as well as different data analysis approaches (mean-square displacement (MSD) analysis and jump-length analysis), for studying single enzyme diffusion.

Publication:

1. **M. Xu**, L. Valdez, A. Sen, J.L. Ross, "Direct Single Molecule Imaging of Enhanced Enzyme Diffusion", Phys. Rev. Lett. 123, 128101 (2019).
2. **M. Xu**, W.B. Rogers, W.W. Ahmed, J.L. Ross, "Comparison of different approaches to single-molecule imaging of enhanced enzyme diffusion", under review at Phys. Rev. E (2020).

09/2019-09/2020
Lab Manager

Set up the new lab space @ Syracuse University

Served as a lab manager to help purchase, install and organize the lab equipment and supplies

Advisor: Jennifer Ross

Overview: We built a new lab space during the year.

- Purchased and setup new equipment (Refrigerator, Centrifuge, Balance, pH meter, Stirrer, Vortexer, Pipettor, Sonicator, Incubator, Electrophoresis, Gel imaging system, NanoDrop, UV/Vis spectrophotometer, PCR machine etc.);
- Ordered biochemical reagents needed for basic biochemical experiments;
- Organized all the lab stuff;
- Built up a custom total internal reflection fluorescence microscope (TIRF) with four-

color laser (405nm, 488nm, 561nm, 638nm);

- ❖ Installed a spinning-disk confocal microscope for fast 3D super resolution imaging.

04/2015-05/2016 **Band Gap Topology and Spin Texture of Transition Metal Dichalcogenides**

Research Assistant *Investigation of the electronic band structure of TMD (such as WSe_2) with Angle Resolved Photoemission Spectroscopy (ARPES)*

Advisor: Chang Liu

Overview: We studied the electronic band structure of diselenides WSe_2, $MoSe_2$ and $MoTe_2$, in particular the transformation from monolayer direct band gap to multilayer indirect band gap, as well as the spin-splitting of monolayer films using ARPES (*Maxlab IV Synchrotron Radiation Facility, Lund University, Sweden*).

BSc Thesis: Electronic structure of ultrathin transition metal dichalcogenides (TMDs) by angle resolved photoemission spectroscopy (ARPES)

03/2014-11/2014 **A New Treatment Plan for AIDS with CRISPR/Cas9 and reconstructed A-B toxin**

Team Leader *International Genetically Engineered Machine Competition (iGEM) 2014*

Research website: *http://2014.igem.org/Team:SUSTC-Shenzhen*

Advisor: Wei Huang

Overview: This project aimed at establishing a more effective HIV-curing system to protect the helper T cells from virus infection by using CRISPR/Cas9 (a special system that bacteria used to protect themselves from infection of virus) as weapon, gRNA as GPS guide, and reconstructed A-B toxin (a target-cell-specific exotoxin of bacteria) as gRNA delivery shuttle. I worked as the team leader of A-B toxin group and my contribution included:

- ❖ Proposed to use modified A-B toxin to realize the multi-times directional DNA introduction *in vivo*;
- ❖ Wrote a review about the reconstruction of bacterial A-B toxin for the entire group;
- ❖ Reached a cooperation with Prof. Winfried Wels (*Institute for Experimental Cancer Research, Tumor Biology Center, Germany*) on reconstruction of A-B toxin;
- ❖ Constructed the key genetic circuits needed for the construction of CRISPR/Cas9 system and gRNA-expression plasmids;

Teaching and Mentoring Experiences

09/2020-Present **Mentor to Ashley Scott** (Post-bachelor at Syracuse)

Making DNA origami, supported lipid bilayer, fluorescent labeling, and diffusion track.

01/2018-05/2018 **Mentor to Mackenzie Naseery** (Undergraduate at UMASS Amherst)

Single molecule imaging of enzymes using TIRF, and particle tracking analysis.

09/2016-05/2018 **Teaching assistant at physics department, UMASS Amherst**

P424 Quantum Mechanism, P131 Physics, P151/P152 Physics lab, P562 Advanced E&M Theory

Internship Experiences

01/2015-02/2015 **Jinan Weishi Road Primary School**

Assistant Science Teacher

- ❖ Mainly responsible for preparing for teaching plans and experimental materials for science classes;
- ❖ Gave experimental lectures, such as The Secret of Simple Pendulum.

07/2013-08/2013 **China Construction Bank (Shenzhen), Nanshan Sub-branch**

Customer Manager Assistant

- Assisted the Customer Manager with housing loan business;
- Learned process of bank business.

Additional

Personal Interests: Painting, hiking, cucurbit flute